NUMERICAL SOLUTION OF MULTIPLE FRONT PHASE CHANGE PROBLEMS FOR MODELING ICE THERMAL STORAGE SYSTEMS

By

Xianhui Yu

Dissertation submitted to the Faculty of the
Virginia Polytechnic Institute and State University
in partial fulfillment of the requirements for the degree of

DOCTOR OF PHILOSOPHY
IN
MECHANICAL ENGINEERING

APPROVED BY

Brian Vick, Co-chairman

Douglas J. Nelson, Co-chairman

Thomas E. Diller

William C. Thomas

Lee Johnson

May, 1995
Blacksburg, Virginia

NUMERICAL SOLUTION OF MULTIPLE FRONT PHASE CHANGE PROBLEMS FOR MODELING ICE THERMAL STORAGE SYSTEMS

By

Xianhui Yu

Brian Vick, Douglas J. Nelson, Co-chairmen

Department of Mechanical Engineering

(ABSTRACT)

Phase change problems with multiple fronts in cylindrical systems, which arise in ice-on-pipe brine thermal energy storage systems, are investigated in this study. Two numerical methods, the boundary element method (BEM) and the thermal network method (TNM), are developed to solve the multiple front phase change problems. In the thermal network method, the distributed effects of sensible energy are approximated as lumped capacity at the boundaries and quasi-steady assumption is used. In the boundary element method, the full effects of sensible energy are precisely considered.

The boundary element method is developed for multiple front phase change problems in one-dimensional radial systems. This method is applied as a module to a 2-dimensional axisymmetric problem and the model is used to predict the dynamic performance of the ice-on-pipe thermal storage systems with a parallel tube arrangement.

The thermal network method is developed to solve the 2-dimensional axisymmetric problems with a moving external boundary and the model is used for the ice-on-pipe thermal systems with both counter flow and parallel flow arrangements.

Performance predictions generated with the TNM are compared to experimental data from Oak Ridge National Laboratory (ORNL) for Calmac and Baltimore Air Coil (BAC) ice thermal storage systems which have counter flow arrangements. The predicted and measured results for the brine exit temperatures and load profiles are in good agreement throughout most of the charge and discharge cycles. Due to the lack of the experimental data for the counter flow arrangements, the results from BEM for the parallel arrangement problems are tested against the TNM and the negligible sensible heat approximation method (NSH) by comparing the outlet temperature, the latent state-of-charge (L-SOC) of the tube. It is found that BEM and TNM both give consistent and accurate results.

ACKNOWLEDGEMENTS

I am greatly indebted to my advisors Dr. Brian Vick and Dr. Douglas J. Nelson for their patience, invaluable help, encouragement and guidance through the course of my graduate studies. I am also very grateful to the other members of my doctoral committee, including Dr. Thomas E. Diller, Dr. William C. Thomas and Dr. Lee Johnson for their help and advice.

I appreciate the support of ASHRAE for the grant APP-699 which supported this research. My appreciation is extended to ORNL for their providing the valuable experimental data in validating my research.

Also I thank my wife Jean for her continued support, patience and love, as well as her willingness to remain in poverty for so long. It's been a long four years for her.

Without all these helps, this work would not have been possible.

TABLE OF CONTENTS

LIST OF FIGURES

LIST OF TABLES

NOMENCLATURE

A	ratio of the thermal diffusivities, α / α_l
Bi	Biot number, $h_b r_{out} / k_l$
c_p	specific heat
F	initial condition contribution
G	Green's function
GI	time integral of Green's function
h	heat transfer coefficient
h_{if}	latent heat of fusion
HI	time integral of $\partial G / \partial r_0$
k	thermal conductivity
K	thermal conductivity ratio, k / k_l
L	length of tube
Lz	dimensionless length of tube, L / r_{out}
Pe	Peclet number of fluid, $\overline{U} r_{pi} / \alpha_b$
r	radial position
R	dimensionless radial position, r / r_{out}
r_{out}	radial position of outside wall surface
s	phase front position

S dimensionless phase front position, s / r_{out}

Ste Stefan number, $(\rho c_p)_l (T_h - T_{fr}) / (\rho_l h_{lf})$

t time

T temperature

T_{fr} phase change temperature of PCM

$\overline{U}$ mean velocity of fluid

V velocity of moving front

z axial position

Z dimensionless axial position, z / r_{out}

Greek letters

α thermal diffusivity

δ_c spatial Dirac function for one-dimensional cylindrical geometry

δ_t time Dirac function

ρ density

θ dimensionless temperature, $(T - T_{fr}) / (T_h - T_{fr})$

τ dimensionless time, $\alpha_l t / r_{out}^2$

τ_c, τ_h dimensionless cooling and heating time

Subscripts

b fluid, average or bulk variable

c cold

f	fluid, local variable
h	hot
i	typical axial segment
in	inlet conditions, $z = 0$
$init$	initial condition
j	general region currently exists
j_{in}	region adjacent to $r = r_{po}$
j_{out}	region adjacent to $r = r_{out}$
l	liquid
out	outside wall surface, $r = r_{out}$
p	tube
pi	tube inside surface, $r = r_{pi}$
po	tube outside surface, $r = r_{po}$
s	solid

Superscripts

n	general time level
nn	current time level

CHAPTER 1 INTRODUCTION

1.1 LITERATURE REVIEW

Phase change problems in cylindrical systems with one or more moving fronts arise in thermal storage applications. There is little research on multiple phase front problems available, especially for problems in cylindrical systems. Numerous authors have addressed problems involving a single phase front (Banerjee and Shaw, 1982, Kim and Kaviany, 1990, Pasquetti and Caruso, 1990 and Vick and Nelson, 1993) but only a few have addressed multiple front phase change problems (Choi and Hsieh, 1992, Nelson and Vick, 1994, Vick and Nelson, 1994 and Yu, Nelson and Vick, 1994), especially in cylindrical systems. Wrobel and Brebbia (1981) addressed the basic formulation using the BEM for axisymmetric transient heat conduction problems, but phase change was not investigated. Sadegh, Jiji and Weinbaum (1987) addressed the buried tube problems in a semi-infinite domain where quasi-steady heat conduction was assumed. Among the proposed numerical techniques, the finite difference and finite element methods have been widely used. In recent years, the boundary element method (BEM) has been applied to phase change and moving boundary problems. The BEM requires discretization only over the boundaries and thus has a major advantage over the finite difference and finite element methods which require a discretization over the complete domain, especially for the phase change problems where nonlinearity is concentrated on the moving boundaries.

Thermal Energy Storage (TES) systems based on latent heat of fusion of ice can be used effectively to decrease peak electric demand or reduce the chiller size required to meet a building cooling load. To properly design a system using TES requires accurate component models to simulate the dynamic response of the system to time-varying loads. In addition, the balance between the storage device, chiller, and load is required for annual energy simulation as well as sizing.

Currently used ice thermal storage systems include ice harvesters, containerized ice systems, direct refrigeration ice-on-pipe systems, and ice-on-pipe brine systems. Previously, the American Society of Heating, Refrigeration and Air Conditioning Engineers sponsored research to develop performance algorithms for the direct refrigeration ice-on-pipe systems under project number RP-459 (Silver et al., 1989a, Silver et al., 1989b). In direct systems, the charging process occurs from inside the pipes while the discharge process occurs on the outside of the pipes by circulating the remaining liquid. This type of system can thus have only one ice layer directly adjacent to the pipe. The ice-on-pipe brine systems, however, are both charged and discharged from the inside of the pipes using a brine (usually a mixture of glycol and water) with a depressed freezing point. As a result, a single ice or liquid layer can exist adjacent to the tubes during a full charge or discharge cycle. In addition, multiple layers of ice and liquid can exist due to a sequence of partial charge and discharge cycles. The creation and evolution of the multiple layers distinguish and complicate the dynamic analysis of ice-on-pipe brine systems from the other ice thermal storage systems. These issues had not previously been investigated.

1.2 MOTIVATION

The research was motivated by the need for an accurate design tool to predict the performance of ice-on-pipe brine systems, which could then be coupled to various algorithms for chiller and load combinations. The absence of a reliable design tool could cause improper design of the system. An undersized thermal storage unit would result in an exit brine temperature too high during a discharge cycle to meet the required cooling load while an oversized unit would result in unnecessary cost. This project is sponsored by the American Society of Heating, Refrigeration and Air-Conditioning Engineers (ASHRAE) under project number RP-699.

1.3 INTRODUCTION

A typical thermal storage tank consists of an array of pipes surrounded by phase change materials (PCM) with brine flowing through the pipes in a counter or parallel flow arrangement. Water is used as the PCM due to a combination of high latent heat, cost and safety. The thermal storage unit, along with a chiller and load are represented in Fig. 1.1. The system can be represented as N flow channels each of length L. In the parallel arrangement, as shown in Fig. 1.2a, the thermal behavior of each tube is essentially the same and is assumed to be an axisymmetric problem. Thus, each tube can be singled out from the symmetry lines shown in Fig. 1.2a. Since there are no heat fluxes across the

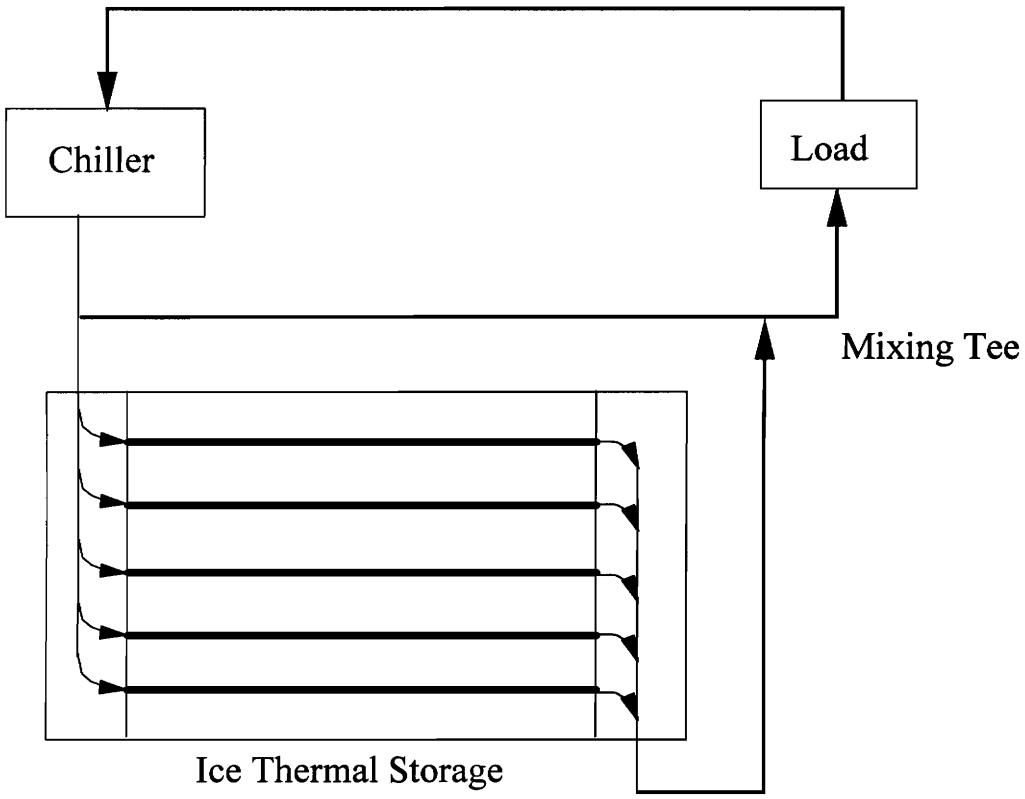

Fig. 1.1: Schematic of Thermal Storage System

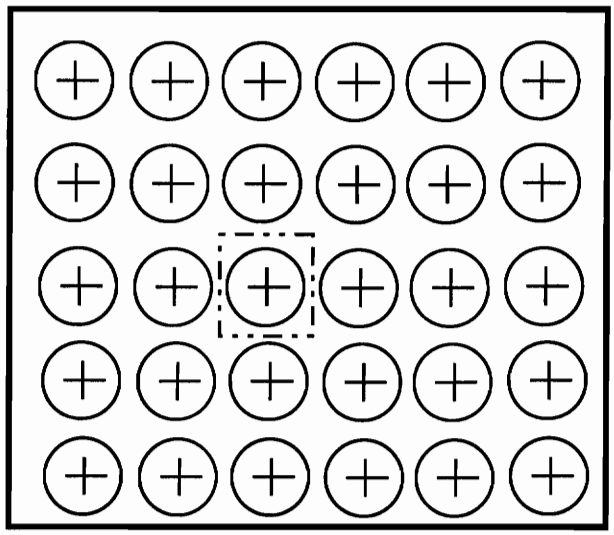

(a)

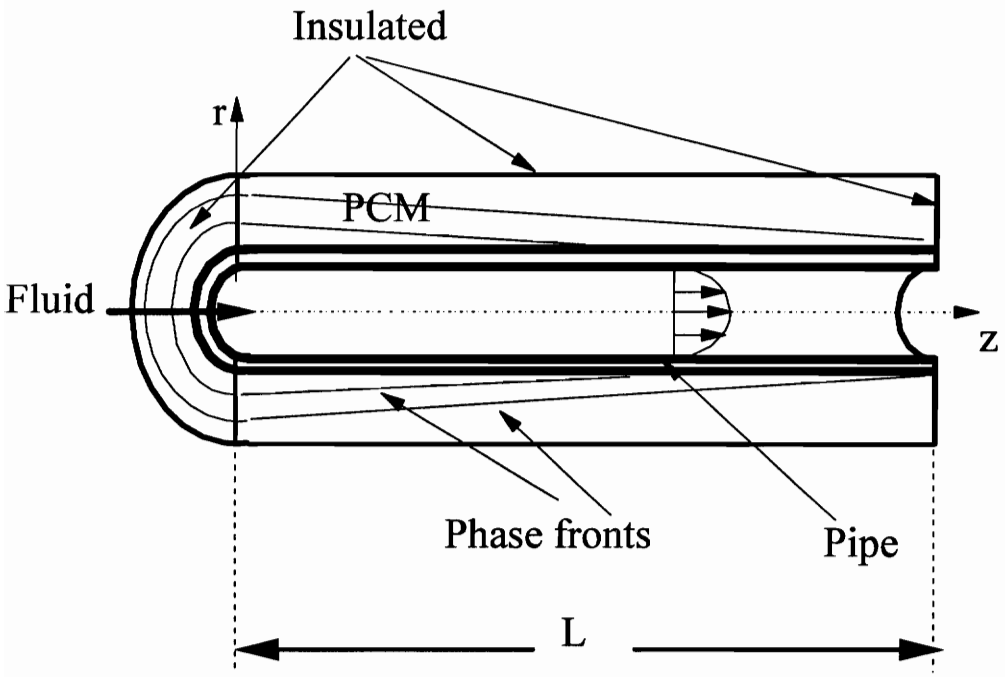

(b)

Fig. 1.2 A typical two-dimensional axisymmetric problem

symmetry lines, the problem of each tube is then modeled as an axisymmetric problem with a round insulated external boundary. The radius of the external boundary is determined by the mass of the PCM evenly distributed to each tube to keep track of the total latent capacity of the ice tank. Thus, the problem can then be reduced to a problem shown in Fig. 1.2b where the tube is buried in the PCM with a fluid flowing inside the it. The tubes are considered as straight and the spiral effects are justified through the correlations in calculation of the convective heat transfer coefficients. The inlet temperature of the fluid cycles across the freeze temperature of the PCM, T_{fr}, and causes the temperature of the tube outer surface to change across T_{fr} which causes alternating layers of liquid or solid to form and propagate from the tube wall.

Since the axial locations near the inlet of a tube tend to have higher charge or discharge rates, the thickness of the adjacent two tubes with different flow directions would be different in the counter flow arrangement, referring to Fig. 1.3. As a result, two adjacent tubes need to be considered together. Each pair of tubes can be singled out from the symmetry lines and all the pairs have essentially the same behavior. The problem can then be reduced to a pair of tubes as shown in Fig. 1.3b. The particular tube pair and the amount of phase change material shared by the tube pairs depends on the geometric arrangement and the resulting plane of symmetry.

For a thin, long geometry and low Rayleigh number in the PCM region encountered in the thermal storage system, as shown in Fig. 1.2, the axial conduction and

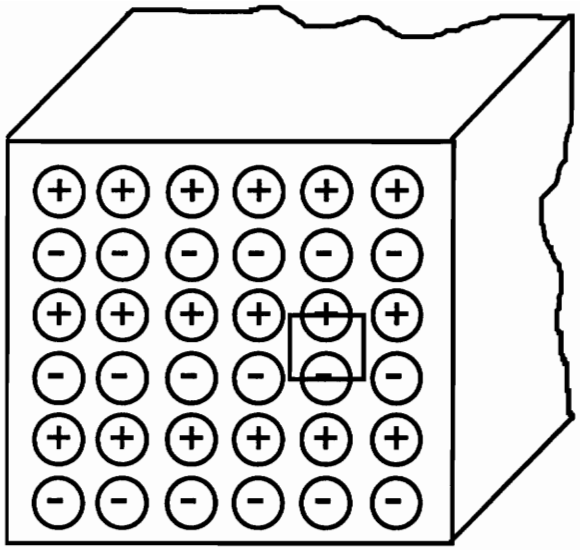

(a)

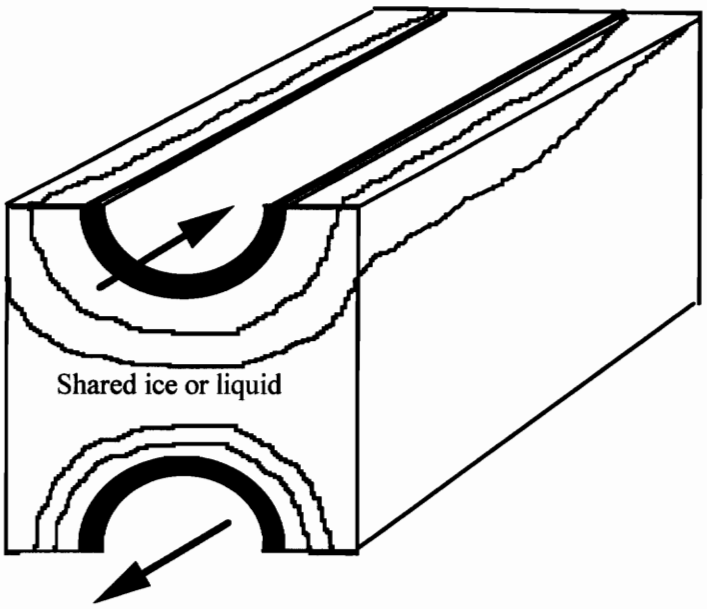

(b)

Fig. 1.3: Ice Thermal Storage Component

convection in the PCM region are all negligible. Thus, the typical tube shown in Fig. 1.2 can then be divided into a sequence of axial segments, shown in Fig. 1.4. In each of the axial segments, an radially one-dimensional conduction problem is assumed. The problem has a convective boundary with the fluid and an axial segment communicates with the downstream axial segments only through the fluid. A boundary element method is developed in chapter 2 for the multiple front phase change problems in one-dimensional cylindrical systems as shown in Fig. 1.5 and a pure PCM is considered. Multiple moving phase fronts arise when the phase change material is subjected to alternate driving temperatures that cause the surface temperature of the PCM to change back and forth across the phase change temperature. This kind of problem is highly nonlinear at the phase fronts that separate alternate liquid and solid layers with different properties. Fully implicit time discretization is applied to ensure numerically stable results. Numerical results are presented for a cylindrical problem with the inner surface subjected to a convective environment where the temperature changes between values above and below the freeze temperature of the PCM. The numerical behavior of the creation and collapse of the moving fronts are investigated by changing the Stefan number, Biot number, initial temperature, the cycling time length and the time step size. In Chapter 3, the BEM developed in Chapter 2 is then applied to the problem shown in Fig. 1.2 as a module for each axial segment as shown in Fig. 1.4. Tube wall and the convective boundary between the fluid and the tube are added to the module. The problem is solved by marching in the axial direction and time.

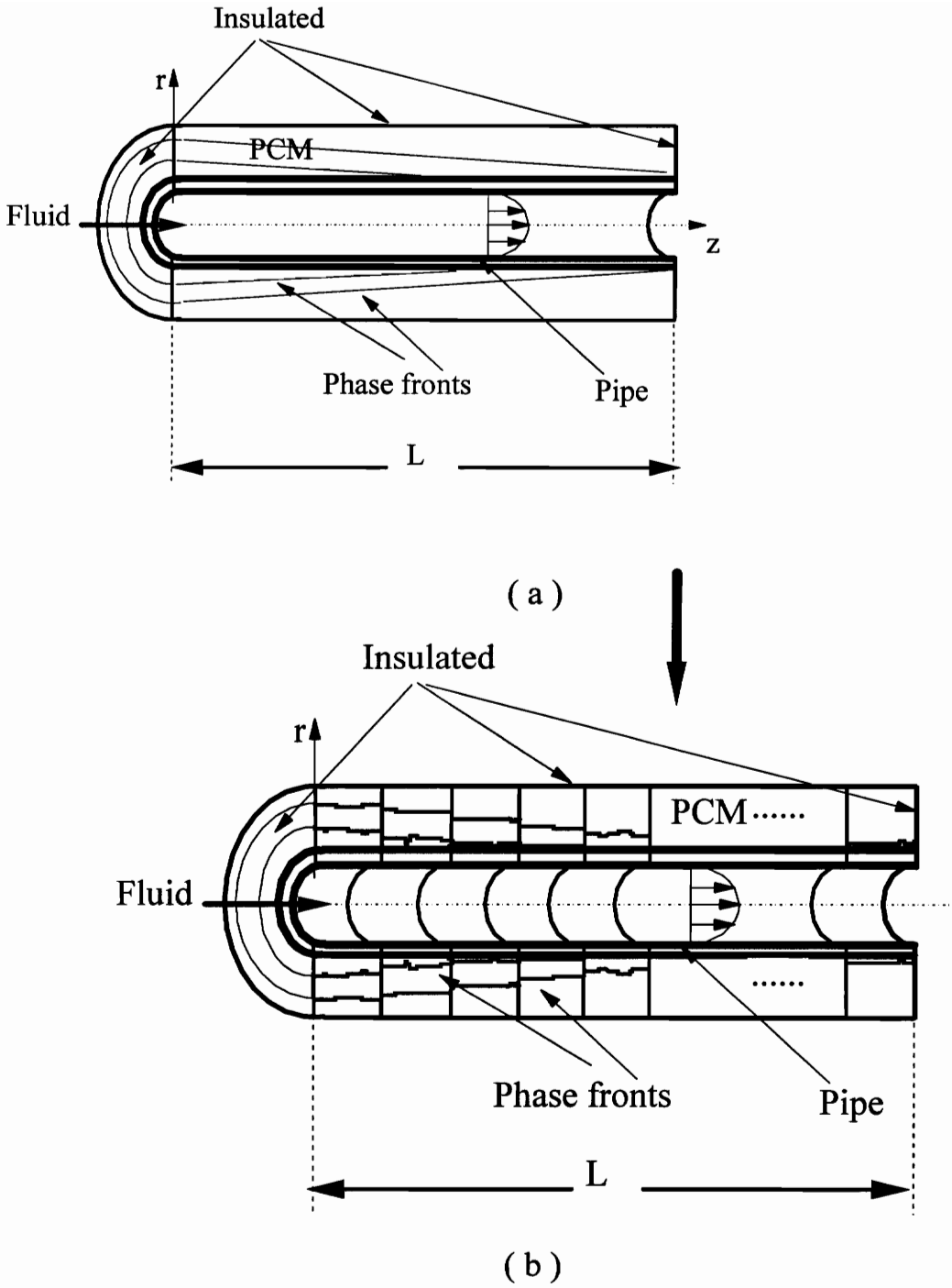

Fig. 1.4 A typical tube surrounded by PCM is simplified as a sequence of axial segments

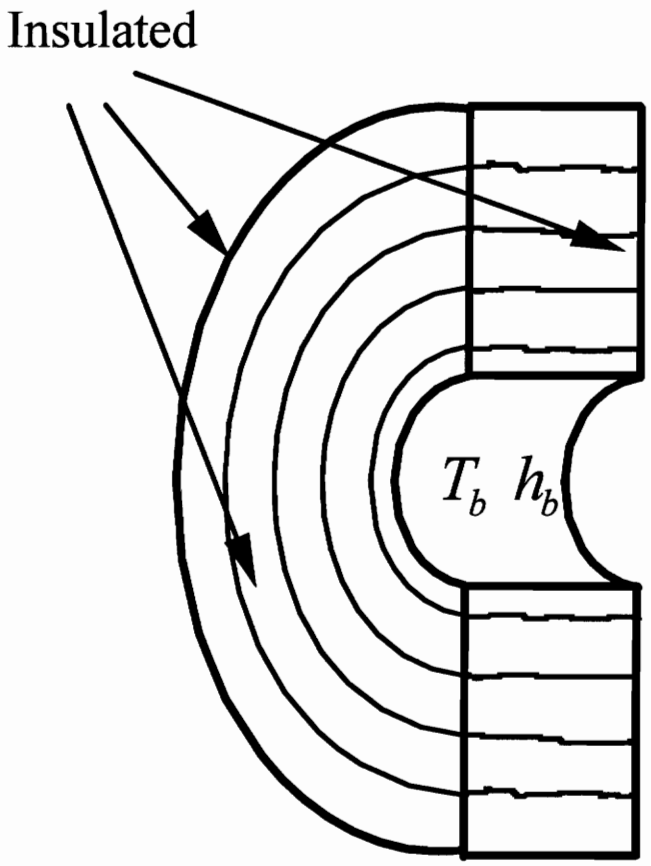

Fig. 1.5 A typical one-dimensional radial problem

Even though the boundary element method developed in Chapter 2 and Chapter 3 is an important contribution to the literature of multiple front phase change problems and to the performance prediction of the ice storage systems with a parallel arrangement, it has the limitation in predicting the performance of the ice storage system with a counter flow arrangement. Chapter 4 describes a model and solution algorithm called the thermal network method (TNM) developed to predict the dynamic performance of an ice-on-pipe brine thermal storage component, especially for the counter flow arrangement. The analysis is developed by considering the thermal storage unit as a collection of tube pairs in a counter flow arrangement. For a long, thin geometry and low Rayleigh number like in the parallel flow arrangement, referring to Fig 1.6, a typical tube pair is numerically divided into a number of sections in the axial direction. one-dimensional, radial heat transfer is considered in each of these axial segments except that the two adjacent axial segments share the PCM between the two tubes. The distributed effects of sensible energy are approximated as lumped capacity at the boundaries and quasi-steady assumption is used.

Chapter 5 presents the results generated from both the TNM and BEM. Using the TNM, a set of parametric studies is presented to show the predicted trends during both charge and discharge cycles with different flow rates and different inlet temperatures. The qualitative behavior for the brine outlet temperature, charge or discharge rate, and state of charge is displayed for a typical thermal storage system. In order to validate the TNM, performance predictions generated with the TNM are compared to experimental data from Oak Ridge National Laboratory (ORNL) for Calmac and Baltimore Air Coil (BAC) ice

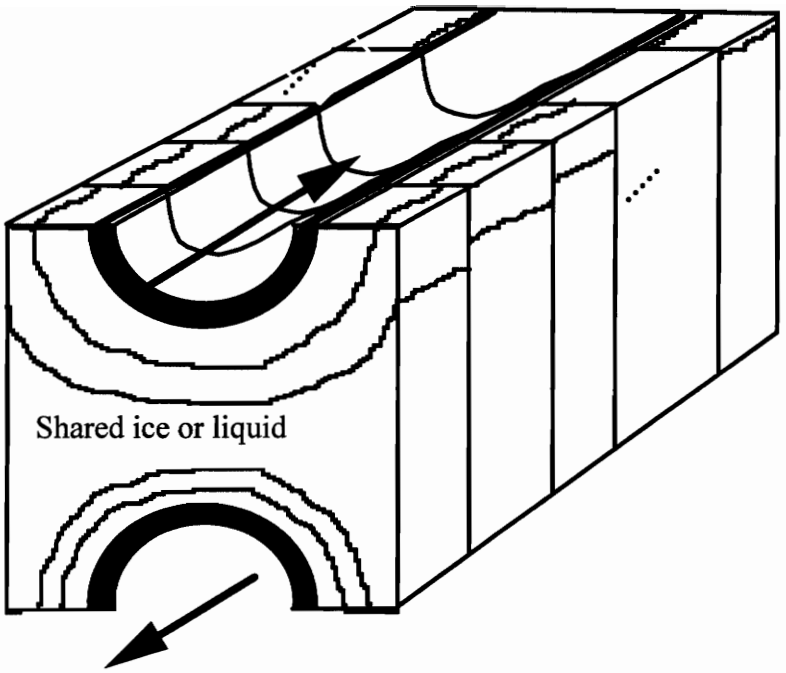

Fig. 1.6 A typical tube pair sharing the PCM is simplified as a sequence of axial segments

thermal storage systems which have counter flow arrangements. Additional results are presented to show a complete system simulation for a typical day in which the thermal energy storage component is coupled with a chiller and load. Because of the lack of experimental data for the parallel flow arrangements, the results generated from the BEM for parallel arrangements are tested against the results generated using the TNM by comparing the outlet fluid temperature and the latent state of charge (L-SOC).

OBJECTIVES

The objectives of this study are:

1. To develop a BEM algorithm for the phase change problems involving multiple phase fronts.
2. To solve the 2-dimensional axisymmetric problems using the BEM algorithm predicting the dynamic performance of an ice thermal storage system.
3. To develop the TNM model and algorithm predicting the dynamic performance of an ice thermal storage system.
4. To validate the TNM and BEM algorithms by comparing the TNM results with experimental data of ORNL and comparing the BEM results with the TNM results.

CHAPTER 2 BEM FOR 1-DIMENSIONAL RADIAL PROBLEMS

2.1 PROBLEM DESCRIPTION

The problem of interest in this chapter is one-dimensional radial transient heat transfer in a finite medium. A pure substance is considered with a melting and freezing temperature of T_{fr}. The substance is contained between two concentric thin circular walls. The inside surface is exposed to convective conditions causing heat to be added in the heating cycle and removed in the cooling cycle. The inner surface temperature of the phase change material could vary back and forth across the freezing temperature and alternating layers of solid and liquid could form and propagate from the inner surface.

This situation is shown in Fig. 2.1, in which the outer surface at $r = r_{out}$ is insulated while the inside surface at $r = r_{in}$ is subjected to a time varying convective boundary condition of T_b and h_b. When T_b cycles across the freezing temperature, alternating layers of liquid and solid will form from the inner surface. The PCM starts at a uniform temperature T_{init} and therefore a single phase of liquid or solid initially exists. The layers are numbered from the outside surface to the inside and any new formed layer is numbered sequentially from the inside surface. A general layer is represented as layer j. Note that a configuration change can occur due to the complete freezing of a liquid layer or complete melting of a solid layer. Whenever a configuration change occurs, all the layers are numbered again sequentially from outside to inside. Thus, the outer most

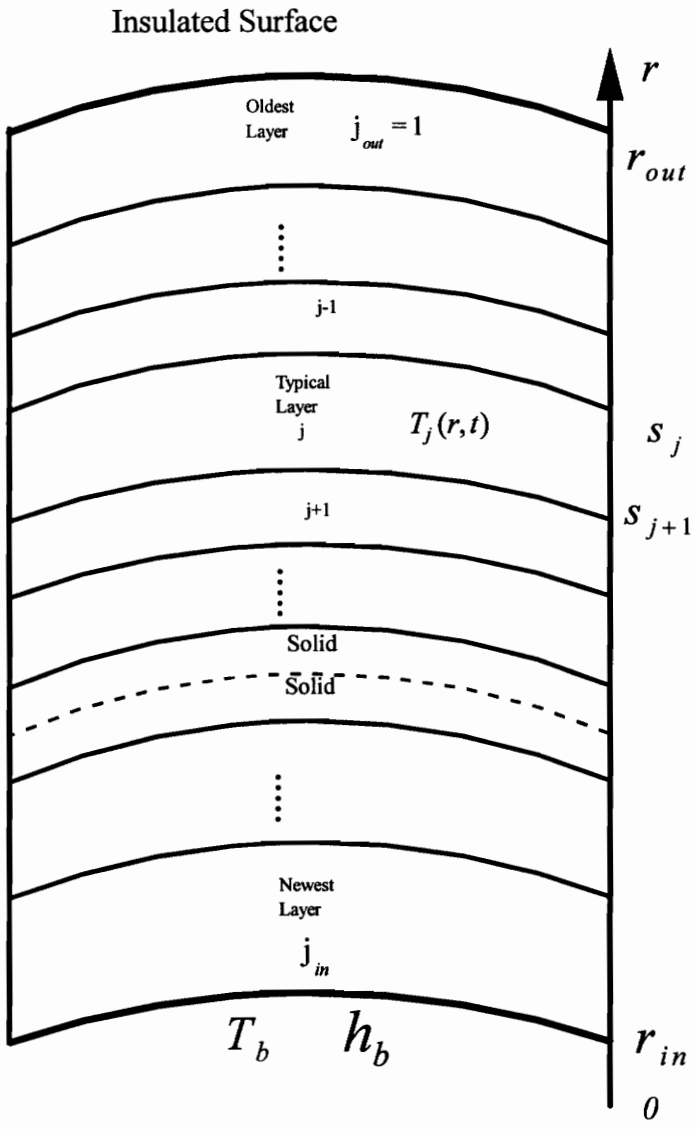

Fig. 2.1: Schematic of physical model

layer is always layer 1 but is not necessarily the one which initially existed since the moving front could reach the outer surface. Also, adjacent layers are not necessarily sequentially formed since a layer could be consumed when one front overtakes the other. In this figure, the thin solid lines represent moving fronts that separate the liquid and solid layers while a dashed line represents a boundary that separate two layers of same phase which were formed at different times.

2.2 GOVERNING EQUATIONS

The thermal properties are assumed to be constant in each solid or liquid layer j. The governing equations for the each PCM layer can be expressed as:

$$\frac{1}{r}\frac{\partial}{\partial r}\left(r\frac{\partial T_j}{\partial r}\right)=\frac{1}{\alpha_j}\frac{\partial T_j}{\partial t}, \quad \text{in layer j} \tag{2.1}$$

where the thermal diffusivity α_j takes different values for different layers:

$$\alpha_j=\begin{cases}\alpha_l, \text{ if layer j is liquid}\\ \alpha_s, \text{ if layer j is solid}\end{cases} \tag{2.2}$$

Since the PCM starts as a single layer at a uniform temperature T_{init}, only one layer initially exists, thus,

$$T_j = T_{init}, \qquad t = 0,\ j = 1 \tag{2.3}$$

During the creation and evolution of the moving fronts, three kinds of boundary conditions could exist.

1. At the *fixed exterior boundaries*, $j = j_{in}$ or $j = 1$,

$$-k_j \frac{\partial T_j}{\partial r} = h(t)[T_b - T_j], \quad \mathrm{r} = \mathrm{r_{in}}, \mathrm{j} = \mathrm{j_{in}} \tag{2.4}$$

$$\frac{\partial T_j}{\partial r} = 0, \qquad \mathrm{r} = \mathrm{r_{out}}, \ \mathrm{j} = 1 \tag{2.5}$$

where subscripts *in* and *out* represent the layer adjacent to the inside surface and the layer adjacent to the insulated outside surface. T_b and h_b are the temperature and heat transfer coefficient of the convective environment.

2. At a *moving boundary*, the difference between the conduction heat transfer on the two sides of the boundary should be the latent energy of the PCM,

$$-\left(k\frac{\partial T}{\partial r}\right)_j + \left(k\frac{\partial T}{\partial r}\right)_{j-1} = \pm\rho h_{if}\frac{ds_j}{dt}, \quad \mathrm{r} = \mathrm{s_j}(t) \tag{2.6}$$

$$T_j(r,t) = T_{j-1}(r,t) = T_{fr}, \qquad \mathrm{r} = \mathrm{s_j}(t) \tag{2.7}$$

where the plus sign in eqn (2.6) applies when the layer j is liquid and minus sign when the layer j is solid.

3. At a *stationary boundary* which separates two layers of the same phase, which arises from the merging of two phase fronts, conservation of energy and continuity of temperature require,

$$k_j \frac{\partial T_j}{\partial r} = k_{j-1}\frac{\partial T_{j-1}}{\partial r}, \quad \text{at } \mathrm{r} = \mathrm{s_j} \tag{2.8}$$

$$T_j(r,t) = T_{j-1}(r,t), \qquad \text{at r = } s_j \tag{2.9}$$

For a layer with an exterior boundary, the unknown at that boundary is the temperature only. At a moving front, the PCM is at the saturated temperature T_{fr} and the front position and the heat flux are the unknowns. At a stationary boundary, the front position is fixed, the temperature and the heat flux are unknown.

2.3 SOLUTION USING THE BEM

For this 1-dimensional radial transient problem, the Green's function with property α_j is governed by the following equation,

$$\frac{1}{r}\frac{\partial}{\partial r}\left(r\frac{\partial G_j}{\partial r}\right)+\frac{1}{\alpha_j}\delta_c(r-r_0)\delta_t(t-t_0)=\frac{1}{\alpha_j}\frac{\partial G_j}{\partial t} \quad \text{in region } 0<r<\infty, t_0<t<\infty \tag{2.10}$$

subject to the conditions,

$$\begin{aligned}&\frac{\partial G_j}{\partial r}=0, r=0\\ &G_j\to 0, r\to\infty\\ &G_j=0, t<t_0\end{aligned} \tag{2.11}$$

where, δ_c and δ_t are Dirac functions for space and time variables, and $G_j \equiv G_j(r,t|r_0,t_0)$ represents the Green's function. The Dirac functions δ_c and δ_t have the following properties for any function $f(r,t)$ continuous in region $[r_1,r_2]$, $[t_1,t_2]$ and $r_0 \in [r_1,r_2]$, $t_0 \in [t_1,t_2]$,

$$\int_{r_0=r_1}^{r_2} \delta_c (r-r_0)\, dA_0 = \int_{r_0=r_1}^{r_2} \delta_c (r-r_0)\, 2\pi r_0 dr_0 = 1 \tag{2.12}$$

$$\int_{t_0=t_1}^{t_2} \delta_t (t-t_0)\, dt_0 = 1 \tag{2.13}$$

$$\int_{t_1}^{t_2} \int_{r_1}^{r_2} f(r,t)\delta_c (r-r_0)\delta_t (t-t_0)\, 2\pi r_0 dr_0 dt_0 = \lambda f(r,t) \tag{2.14}$$

$$\text{where, } \lambda = \begin{cases} \frac{1}{2} & , \quad r_0 = r_1 \text{ or } r_0 = r_2 \\ 1 & , \quad r_1 < r_0 < r_2 \end{cases} \tag{2.15}$$

Solving eqn (2.10) gives the Green's function as (Beck and Cole, 1992),

$$G_j(r,t;r_0,t_0) = \frac{1}{4\pi\alpha_j (t-t_0)} \exp\left(-\frac{r^2 + r_0^{\,2}}{4\alpha(t-t_0)}\right) I_0\left(\frac{rr_0}{2\alpha(t-t_0)}\right) \tag{2.16}$$

From eqn (2.16), the derivative of the Green's Function with respect to r_0 is,

$$\frac{\partial G_j}{\partial r_0} = \frac{\exp\left(-\frac{r^2 + r_0^{\,2}}{4\alpha(t-t_0)}\right)}{8\pi\alpha_j^{\,2}(t-t_0)^2} \left\{ r\, I_1\left(\frac{rr_0}{2\alpha_j (t-t_0)}\right) - r_0\, I_0\left(\frac{rr_0}{2\alpha_j (t-t_0)}\right) \right\} \tag{2.17}$$

where, I_0 and I_1 are the modified Bessel functions.

The meaning of eqn (2.10) is that the Green's Function $G(r,t|r_0,t_0)$ represents the temperature at location r and time t due to the instantaneous concentrated ring heat

source of strength unity released at time t_0 and the location r_0 with the initial and boundary conditions defined in eqn (2.11).

2.3.1 Solution For Layer j In Terms of Green's Function

The most significant advantage of BEM is that it generally reduces the dimension of the problem by one. For this one-dimensional radial problem, the integrals over boundary surfaces reduce to evaluation at the boundary points. As they vary much slower than the Green's function G_j and its derivative $\partial G_j / \partial r_0$, the time variables are divided into discrete time steps and integrated by assuming constants for the unknown boundary data in each time interval. This piecewise constant, fully implicit manner is applied to ensure the numerical stability.

For each layer j that starts at time t_j as shown in Fig. 2.2, the thermal diffusivity α_j is a constant. The energy equation eqn (2.1) is multiplied by the Green's function and integrated over domain Ω_0 and time t_0 to get,

$$\int_{t_0=t_j}^{t} \int_{r_0=s_{j+1}}^{s_j} G_j \left[\frac{1}{r_0} \frac{\partial}{\partial r_0} \left(r_0 \frac{\partial T_j}{\partial r_0} \right) - \frac{1}{\alpha_j} \frac{\partial T_j}{\partial t_0} \right] d\Omega_0 dt_0 = 0 \tag{2.18}$$

where, $\Omega_0 : s_{j+1}(t) < r_j < s_j(t), d\Omega_0 = 2\pi r_0 dr_0$

The first portion of eqn (2.18) is integrated by parts twice and the second term once. As the boundaries could change with time, a Leibnitz rule must be applied for time varying boundaries $s_{j+1}(t)$ and $s_j(t)$. Then the eqn (2.18) becomes,

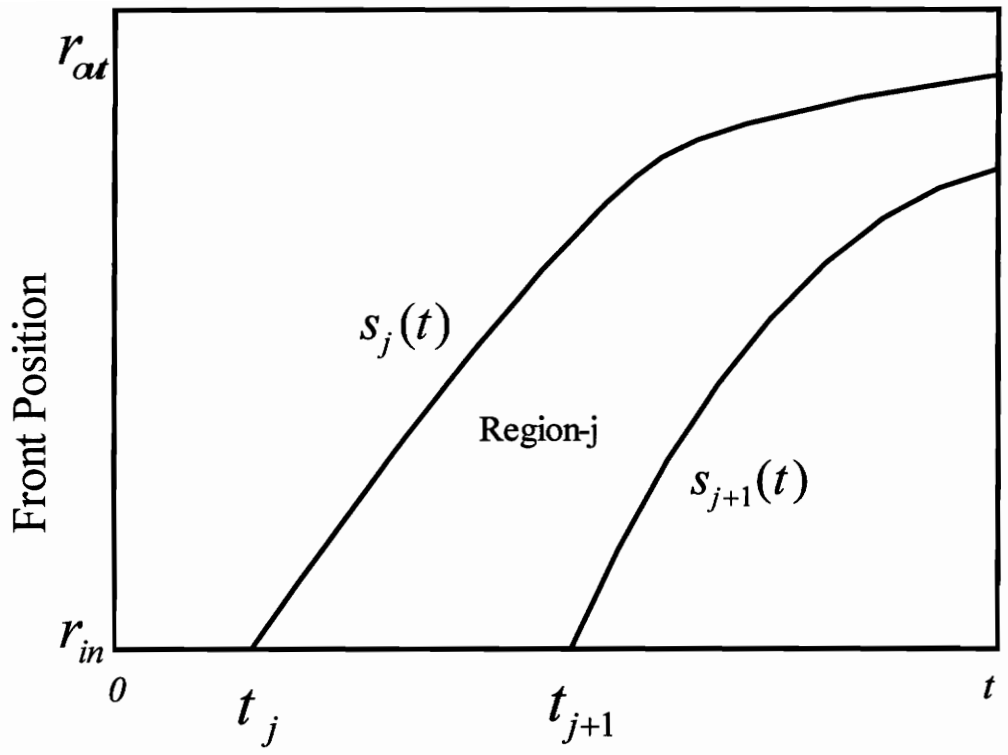

Figure 2.2: Domain of a typical layer

$$\int_{t_0=t_j}^{t}\int_{r_0=r_1(t_0)}^{r_2(t_0)} T_j\left[\frac{1}{r_0}\frac{\partial}{\partial r_0}\left(r_0\frac{\partial G_j}{\partial r_0}\right)+\frac{1}{\alpha}\frac{\partial G_j}{\partial t_0}\right]2\pi r_0 dr_0 dt_0$$

$$+2\pi\int_{t_0=t_j}^{t}\left\{\left[G_j r_0\frac{\partial T_j}{\partial r_0}-Tr_0\frac{\partial G_j}{\partial r_0}+T_{fr}G_j V_{r_0}\right]_{r_0=s_j(t_0)}\right\}dt_0 \qquad (2.19)$$

$$-2\pi\int_{t_0=t_j}^{t}\left\{\left[G_j r_0\frac{\partial T_j}{\partial r_0}-T_j r_0\frac{\partial G_j}{\partial r_0}+T_{fr}G_j V_{r_0}\right]_{r_0=s_{j+1}(t_0)}\right\}dt_0$$

$$+F_j(r,t)$$

where the term of $F_j(x,t)$ represent the initial condition influence,

$$F_j(r,t)=\begin{cases}2\pi\int_{r_1(t_0)}^{r_2(t_0)} r_0 G_j T_{init}\,dr_0 & \text{, if j = 1 and } t_0 = 0\\ 0 & \text{, elsewhere}\end{cases} \qquad (2.20)$$

V_{r_0} is the velocity of a phase front. For fixed boundaries at the inside and outside surfaces and the composite boundaries, this velocity term is zero.

From the definition of Green's function, switch r with r_0, $-t$ with $-t_0$ then, one can get the reciprocity condition of the Green's Function as,

$$G_j(r,t|r_0,t_0)=G_j(r_0,-t_0|r,-t) \qquad (2.21)$$

and,

$$\frac{1}{r_0}\frac{\partial}{\partial r_0}\left(r_0\frac{\partial G_j}{\partial r_0}\right)+\frac{1}{\alpha_j}\frac{\partial G_j}{\partial t_0}=-\frac{1}{\alpha_j}\delta_c(r_0-r)\delta_t(t_0-t) \qquad (2.22)$$

Substituting eqn (2.22) into eqn (2.19) and applying the property (2.14) of Dirac delta functions gives,

$$\frac{\lambda}{2\pi\alpha_j}T_j(r,t) = F_j(r,t)$$
$$+\int_{t_0=t_j}^{t}\left\{\left[G_j r_0\frac{\partial T_j}{\partial r_0} - T_j r_0\frac{\partial G_j}{\partial r_0} + T_{fr}G_j V_{r_0}\right]_{r_0=s_j(t_0)}\right. \tag{2.23}$$
$$\left.-\left[G_j r_0\frac{\partial T_j}{\partial r_0} - T_j r_0\frac{\partial G_j}{\partial r_0} + T_{fr}G_j V_{r_0}\right]_{r_0=s_{j+1}(t_0)}\right\}dt_0$$

$$\text{where, } \lambda = \begin{cases}\frac{1}{2} & , \quad r = s_j \text{ or } r = s_{j+1}\\ 1 & , \quad r \neq s_j \text{ and } r \neq s_{j+1}\end{cases} \tag{2.24}$$

Equation (2.23) is discretized in time as shown in Fig. 2.3 to get,

$$\frac{\lambda}{2\pi\alpha_j}T_j(r,t) = F_j(r,t)$$
$$+\sum_{n=n_j+1}^{nn}\int_{t_0=t^{n-1}}^{t_0=t^n}\left\{\left[G_j r_0\frac{\partial T_j}{\partial r_0} - T_j r_0\frac{\partial G_j}{\partial r_0} + T_{fr}G_j V_{r_0}\right]_{r_0=s_j(t_0)}\right\}dt_0 \tag{2.25}$$
$$-\sum_{n=n_j+1}^{nn}\int_{t_0=t^{n-1}}^{t_0=t^n}\left\{\left[G_j r_0\frac{\partial T_j}{\partial r_0} - T_j r_0\frac{\partial G_j}{\partial r_0} + T_{fr}G_j V_{r_0}\right]_{r_0=s_{j+1}(t_0)}\right\}dt_0$$

To perform the calculation in eqn (2.25), integrals of the following types are defined,

$$(GI)^n = \int_{t^{n-1}}^{t^n} G_j(r,t|r_0,t_0)dt_0$$
$$(HI)^n = \int_{t^{n-1}}^{t^n}\frac{\partial G_j(r,t|r_0,t_0)}{\partial r_0}dt_0 \tag{2.26}$$

where the subscript n represents the n_{th} time step.

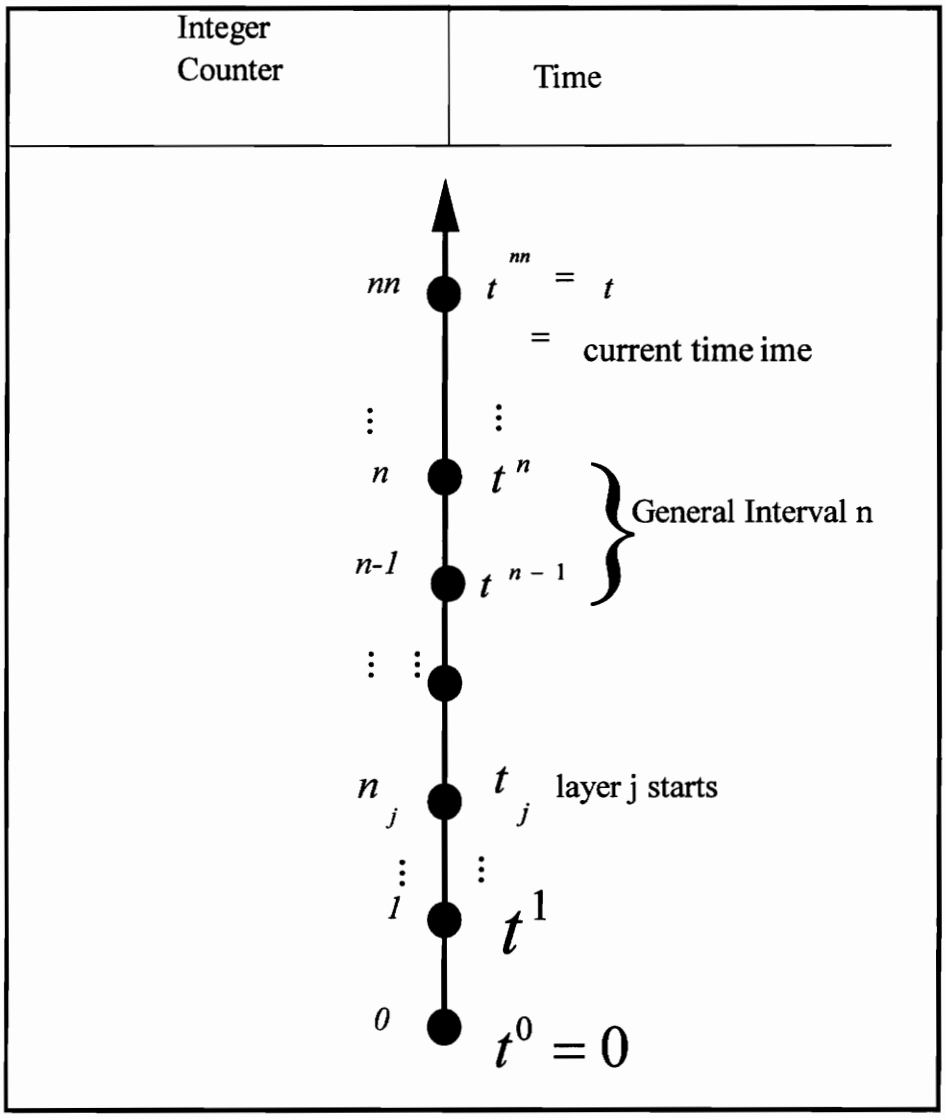

Figure 2.3: Time discretization

With the definitions above and using a *fully implicit* scheme, the discretized solution eqn (2.25) can be expressed as,

$$\frac{\lambda}{2\pi\alpha_j} T_j^{mn}(r) = F_j(r,t)$$
$$+ \sum_{n=n_j+1}^{mn} \left(r_0 \left(\frac{\partial T_j}{\partial r_0} \right)^n (GI)^n - T_j^n r_0 (HI)^n + T_{fr} V_{r_0} (GI)^n \right)_{r_0 = s_j(t_0)} \qquad (2.27)$$
$$- \sum_{n=n_j+1}^{mn} \left(r_0 \left(\frac{\partial T_j}{\partial r_0} \right)^n (GI)^n - T_j^n r_0 (HI)^n + T_{fr} V_{r_0} (GI)^n \right)_{r_0 = s_{j+1}(t_0)}$$

where $(\partial T_j / \partial r_0)^n$ and T_j^n are the heat flux and temperature values at the time t^n.

Thus, for layer j at the current time t^{mn}, two simultaneous equations can be obtained by evaluating the eqn (2.27) at both boundaries of this layer, $r = s_{j+1}(t_0)$ and $r = s_j(t)$. These equations can be written in matrix form as,

$$\mathbf{A_j U_j = B_j} \qquad (2.28)$$

where, $\mathbf{A_j}$ is a 2×2 matrix that depends on geometry, thermal properties of the medium and the time step. $\mathbf{U_j}$ and $\mathbf{B_j}$ are 2×1 matrices. where $\mathbf{U_j}$ represents the unknowns,

$$\mathbf{U_j} = \begin{bmatrix} U_{j2} \\ U_{j1} \end{bmatrix} \qquad (2.29)$$

and $\mathbf{B_j}$ accounts for the history of this layer that depends on geometrical data, properties of the medium, the time step, the values of unknowns at the previous time steps and the initial condition of this layer.

For a layer with no moving front, such as the inner and outer boundaries and the boundary separating two layers of the same phase, the unknowns U_{j1} and U_{j2} could be temperature or heat flux depending on the boundary conditions. For a layer with one or more moving fronts, the unknowns at a moving front should be the heat flux because the temperature is locked to the freezing temperature T_{fr} of the PCM and the front location should be determined through iteration.

Note that the integrals defined in eqn (2.26) cannot be performed analytically and polynomial approximations of the Bessel functions are applied before the integrations are performed [see Appendix C].

To simplify the calculation, the freezing temperature takes the value of zero. This simplification does not reduce the generality of this method.

Multiply eqn.(2.6) by $2\pi s_j$, integrate over time from t_{nn-1} to t_{nn}. The discretized form of the energy balance at a moving boundary, eqn (2.6), can be expressed as,

$$[(s_j^{nn})^2 - (s_j^{nn-1})^2]\,\rho h_{if} \pm 2 s_j^{nn} \Delta t \left[k_j \left(\frac{\partial T_j}{\partial r} \right)^{nn} - k_{j-1} \left(\frac{\partial T_{j-1}}{\partial r} \right)^{nn} \right] = 0 \text{ , at } \mathrm{r} = \mathrm{s}_\mathrm{j}^{\mathrm{nn}} \quad (2.30)$$

2.3.2 Computational Algorithm

The problem under investigation begins as a single layer of either liquid or solid with a uniform temperature of T_{init}. The inside surface is subjected to a convective environment with specified time variation of T_b and h_b over each time step with a time marching scheme.

At each time step, the unknowns for each PCM layer involve a combination of temperatures, heat fluxes and the phase front positions depending on the boundary conditions of the layer considered. As the boundary of a moving front is highly nonlinear, an iterative scheme is applied for the moving front positions. The calculation is first carried out at this time step by assuming no configuration change. Newton's method is employed in determination of a phase front for a moving boundary and of the temperature for a boundary separating two layers of same phase. After getting the converged results for all the layers, a check is performed to determine if configuration change(s) arises. If there is more than one configure change at the same time step, the code will deal with them one by one. The possible configuration changes are:

1. The inner surface temperature crosses the freezing temperature T_{fr} , a new layer forms.
2. A phase front consumes an adjacent layer and merges with another phase boundary, producing a stationary composite boundary which separates two layers of the same phase.
3. The phase front reaches the outer surface of the PCM and thus the layer adjacent to the outer surface is consumed.

2.3.3 Numerical Behavior

The present work is an extension of the multiple front problems for the planar problem by Nelson and Vick. In these works, the behavior of the problem with different

Stefan numbers, initial temperatures and time variations of the driving temperature is investigated. In the present work, the influences of Stefan number, initial temperature, Biot number, cycling time of driving temperature and time step size are investigated. The limiting cases of no sensible heat phase change and pure conduction were also tested and found to give consistent and accurate results. The sample results given in the following section are all created by changing a single parameter from a standard case to investigate the behavior of the problem with the specific parameter change. The standard case begins at an all liquid condition at the initial nondimensional temperature of 0, Stefan number of 0.1, Biot number of 1 and 100 time steps for each heating or cooling cycle with the time step of 0.1 .

The influence of time step size was investigated. A time step 10 times bigger than the regular one was applied and that gave consistent results with those from fine time steps. These results will be discussed later.

2.4 RESULTS

To investigate the dynamic evolution of the multiple phase fronts, the most important parameters are considered, i.e. the Stefan number, Biot number, initial temperature, time step size and time period of the cooling or heating cycles τ_c or τ_h. The results are presented with nondimensional variables defined in Tables 2.1a, 2.1b.

TABLE 2.1a: DEFINITION OF DIMENSIONAL AND DIMENSIONLESS PHYSICAL VARIABLES

Definition	Physical Variables	Dimensionless Variables	Definition of Dimensionless Variables
Time	t	$\tau = \alpha t / r_{out}^2$	Time
Radial Location	r	$R = r / r_{out}$	Radial Location Ratio
Temperature	$T(r,t)$	$\theta(R,\tau) = \dfrac{T(r,t) - T_{fr}}{T_h - T_{fr}}$	Temperature Ratio
Temperature at r_{in}	$T_{in}(t)$	$\theta_{in}(\tau) = \dfrac{T_{in}(t) - T_{fr}}{T_h - T_{fr}}$	Temperature at R_{in}
Temperature at r_{out}	$T_{out}(t)$	$\theta_{out}(\tau) = \dfrac{T_{out}(t) - T_{fr}}{T_h - T_{fr}}$	Temperature at R_{out}
Moving Front Location	$s_j(t)$	$S_j(\tau) = s_j(t) / r_{out}$	Moving Front Location
Heat Flux at a Boundary	$q_j'' = -k_j \dfrac{\partial T}{\partial r}$	$-K_j \dfrac{\partial \theta}{\partial R}$	Heat Flux at a Boundary
Convective Heat Flux at r_{pi}	$q_p'' = h \cdot (T_{pi} - T_b)$	$Bi \cdot (\theta_{pi} - \theta_b)$	Convective Heat Flux at R_{in}

TABLE 2.1b: DEFINITION OF DIMENSIONAL AND DIMENSIONLESS PHYSICAL PARAMETERS

Definition	Physical Parameters	Dimensionless Parameters	Definition of Dimensionless Parameter
High, Low Inlet Temperatures	T_h, T_{low}	+1,–1	High, Low Inlet Temperatures
Initial Temperature	T_{init}	θ_{init}	Initial Temperature
Fluid Temperature	T_b	θ_b	Fluid Temperature
Convection Coefficient	h_b	$Bi = \frac{h_b r_{out}}{k_l}$	Biot Number
Volume Latent Heat	ρh_{if}	$Ste = \frac{(\rho c_p)_l (T_h - T_{fr})}{\rho_l h_{if}}$	Stefan Number
Conductivity of Liquid	k_l	1	Reference Conductivity
Conductivity of Solid	k_s	$K_s = \frac{k_s}{k_l}$	Conductivity Ratio
Thermal Diffusivity of Liquid	α_l	1	Reference Thermal Diffusivity
Thermal Diffusivity of Solid	α_s	$A_s = \frac{\alpha_s}{\alpha_l}$	Thermal Diffusivity Ratio
Outer Radius	r_{out}	1	Reference Length
Inside Radius	r_{in}	$R_{in} = \frac{r_{in}}{r_{out}}$	Radius Ratio

To illustrate the method, water is used as the PCM. A standard case is taken as, $Bi = 1.0$, $Ste = 0.1$, $\theta_{init} = \theta_{fr}$, $\Delta\tau = 0.1$ and the driving temperature θ_b switches between cold (-1) and hot $(+1)$. The nondimensional inside and outside radiuses of cylinder are set to $R_{in} = 0.25$ and $R_{out} = 1.0$. For illustration, the two cycling periods are the same $(\tau_c = \tau_h)$ with 100 time steps in each cycling period.

In figures 2.4 to 2.9, the bottom portion shows the position of each front varying with time. When one front overtakes another, the layer between them disappear and the front separating these two adjacent layers is fictitious (represented with a dotted line) because these two layers are of same phase. When a moving front reaches the upper limit $(s(\tau) = 1.0)$, the layer adjacent to the outer wall surface is consumed. All the phase fronts are represented in solid lines except the fictitious boundaries. The liquid and solid layers are labeled in each region. All the properties and the parameters for Fig. 2.4 to Fig. 2.9 are listed in Table 2.2.

The top portion shows the time variation of environment temperature θ_b, inside wall temperature θ_{in} at $R = R_{in}$ and the outside wall temperature θ_{out} at $R = R_{out}$. A new layer forms when θ_{in} crosses the freeze temperature $(\theta_{fr} = 0)$.

Figure 2.4 and Fig. 2.5 have the same parameters except for the cycling periods. In Fig. 2.4, the hot and cold periods τ_h and τ_c are 20. The PCM begins as an all liquid at an initial condition of $\theta_{init} = \theta_{fr}$, while the convective heat transfer takes place with an environment at Biot number of 1.0 . Stefan number is set to 0.1 which is representative of

Table 2.2 PROPERTIES AND PARAMETERS OF THE SAMPLE CASES

	Ste	Bi	θ_{init}	$\Delta\tau$	K_s	A_s
Fig. 2.4	0.1	1.0	0.0+	0.4	3.88	8.51
Fig. 2.5	0.1	1.0	0.0+	0.2	3.88	8.51
Fig.2.6	0.1	1.0	0.0+	2.0	3.88	8.51
Fig.2.7	0.1	1.0	1.0	0.2	3.88	8.51
Fig. 2.8	0.1	0.1	0.0+	2.0	3.88	8.51
Fig. 2.9	1.0	1.0	0.0+	0.02	3.88	8.51

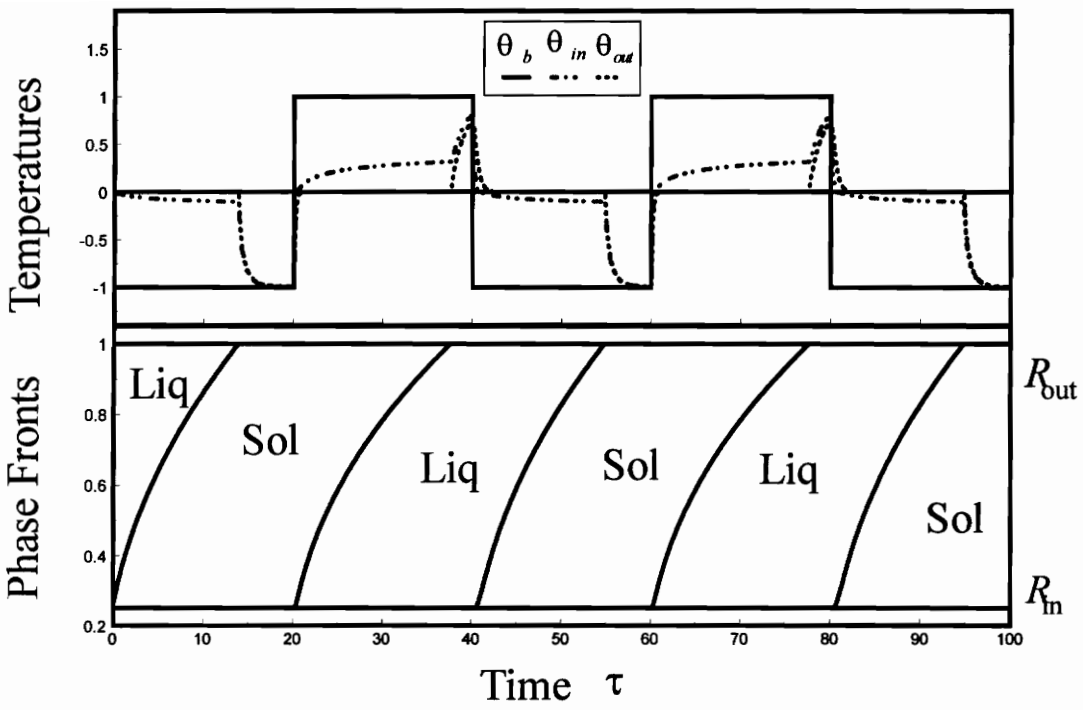

Figure 2.4: Time evolution of temperatures and phase front positions for *long* cooling and heating cycling period

phase change problems of water with moderate temperature differences. The cold and hot time periods are 20. At time $\tau = 0$, the driving temperature θ_b is set to -1. Since the initial temperature is at the saturated point, the first freeze phase front starts at the first time step and propagates as a solid layer. At time $\tau = 14$, the freeze front reaches the outer surface $R = 1$, eliminating the original liquid layer. Then, sensible energy is quickly removed as shown by the sudden drop in θ_{out} to the environment temperature of -1. At $\tau = 20$, θ_b switches to $+1$, initiating a melt front. In this heating cycle. The melt front reaches the outer wall surface at $\tau = 37.4$, 17.4 after the start of the melt front, which is longer than that in the first cycle because of the lower conductivity of liquid and the sensible heat stored in the previous cycle. The new cooling cycle starts at $\tau = 40$ and it takes a little longer that in the first cycle to reach to the outer surface at $\tau = 54.6$ because of the sensible heat stored in the previous heating cycle. In Fig. 2.4, only one front exists at each cooling or heating cycle.

Figure 2.5 shows the standard case defined earlier with the same parameters of Fig. 2.4 except that the cycling periods τ_h and τ_c are 10. At time $\tau = 0$, the driving temperature θ_b is set to -1, initiates the first freeze phase front at the first time step and propagates as a solid layer. At time $\tau = 10$, θ_b switches to $+1$, initiating a melt front and virtually locking the freeze front at $r = 0.86$. At time $\tau = 20$, a new cooling cycle starts while the melt front only reaches $r = 0.80$ because of the lower conductivity of liquid and the sensible heat stored in previous cycle. A new freeze front starts while the freeze and

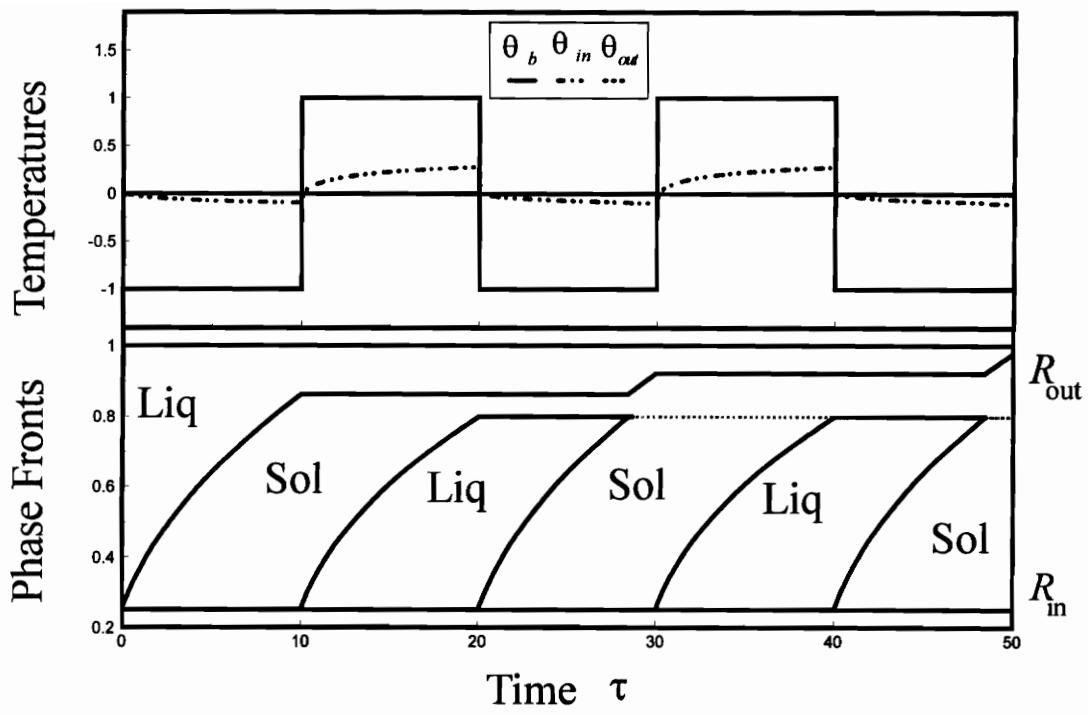

Figure 2.5: Time evolution of temperatures and phase front positions for *short* cooling and heating cycling period

melt fronts formed earlier are locked at $r = 0.86$ and $r = 0.80$. At $\tau = 28.5$, the new formed freeze front overtakes the former melt front at $r = 0.80$ and consumes the liquid layer between the two solid layers, causing the coalescence of these two layers. This coalescence is shown as a dashed line. The two fronts merge at $r = 0.80$ and are fixed there for numerical purposes. The melt front actually moved a little from 0.80 to 0.8002 before merging with the freeze front. This is the accumulated effect of sensible heat during the freeze cycle. The previously isolated freeze front at $r = 0.86$ is now connected to the environment through a continuous solid layer and begins to propagate towards the outer wall surface. At $\tau = 30$, θ_b switches to $+1$ again and the new melt front stops the propagation of the freeze front before it propagates to the outer wall surface. The new melt front propagates to nearly the same position as the first melt front before the next freeze cycle begins.

Figure 2.6 shows the influence of the time step size. A factor of 10 times of the time step size of that in Fig. 2.5 is applied with 10 time steps in each period. Like in Fig. 2.5, the freeze front propagates to $r = 0.86$ when the first melt front forms. The melt front propagates to $r = 0.80$ when the second freeze front starts. This freeze front overtakes the melt front at $\tau = 29.0$ and the first freeze front is driven towards to the outer surface and stop again at $r = 0.94$ when next melt front initiates at $\tau = 30$. Note that the first freeze front reaches the outer surface when $\tau \approx 50$ in Fig. 2.6 while it still does not go that far in Fig. 2.5. This is the accumulated error because of this large time step.

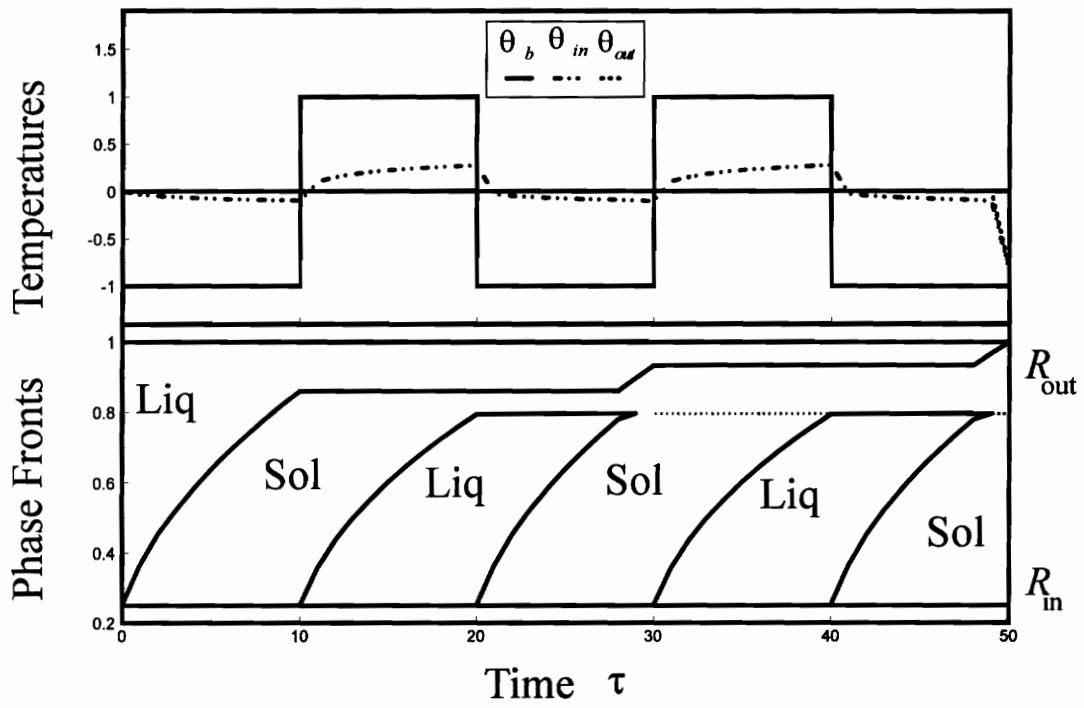

Figure 2.6: Time evolution of temperatures and phase front positions for *large* time steps

In Fig. 2.7, all the conditions are the same as in Fig. 2.5 except for the initial temperature. The PCM starts at a uniform nondimensional temperature of $\theta_{init} = 1$. At $\tau = 10$, the freeze front propagates to $r = 0.84$ when the melt fronts starts. Because of the sensible heat, the freeze front does not propagate as far as in Fig. 2.5. All the other results are similar to those in Fig. 2.5.

In Fig. 2.8, the influence of Biot number is investigated. All the conditions are the same as in Fig. 2.5 except that the Biot number is changed to $Bi = 0.1$ by reducing the convection with the environment by 10. With this condition, the heat transfer slows down by factor of 10, and the temperature difference in the whole region decrease dramatically and the effect of the conductivity difference is also minimized.

Figure 2.9 shows the influence of the Stefan number. The Stefan number is increased by a factor of 10 from 0.1 to 1.0. For water properties, this higher Stefan number represents freezing and melting with large temperature differences. It is analogous to Fig. 2.5 in that $\tau_c = \tau_h = 1$. At $\tau = 0$, θ_b is set to -1, a freeze front forms at the first time step since the whole region begins at the T_{fr}. At $\tau = 1$, θ_b switches from -1 to $+1$, a melt front initiates while the freeze front reaches $r = 0.86$ and continues propagating to $r = 0.862$ before it stays locked. At $\tau = 2$, θ_b switches to -1, the melt front reaches $r = 0.79$ before the new freeze front initiates and propagates to $r = 0.793$ before it becomes still. The new freeze front overtakes the melt front at $\tau = 2.84$ and results in a continuous solid layer. The first freeze front is now connected to the

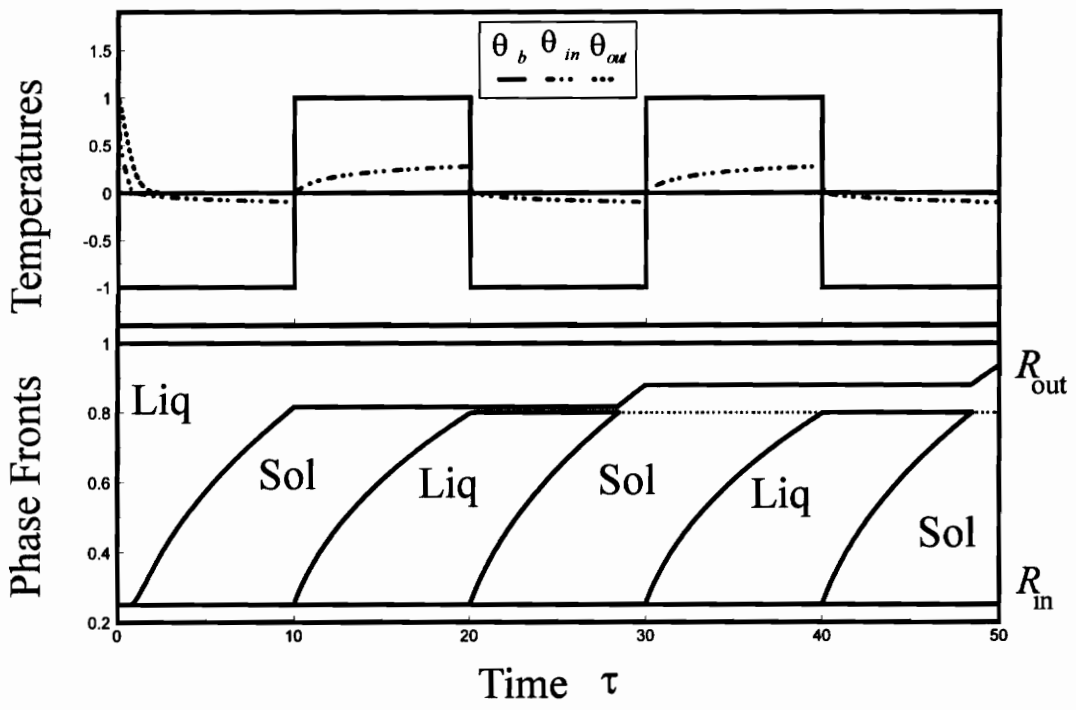

Figure 2.7: Time evolution of temperatures and phase front positions for *short* cooling and heating cycling period and *high* initial temperature

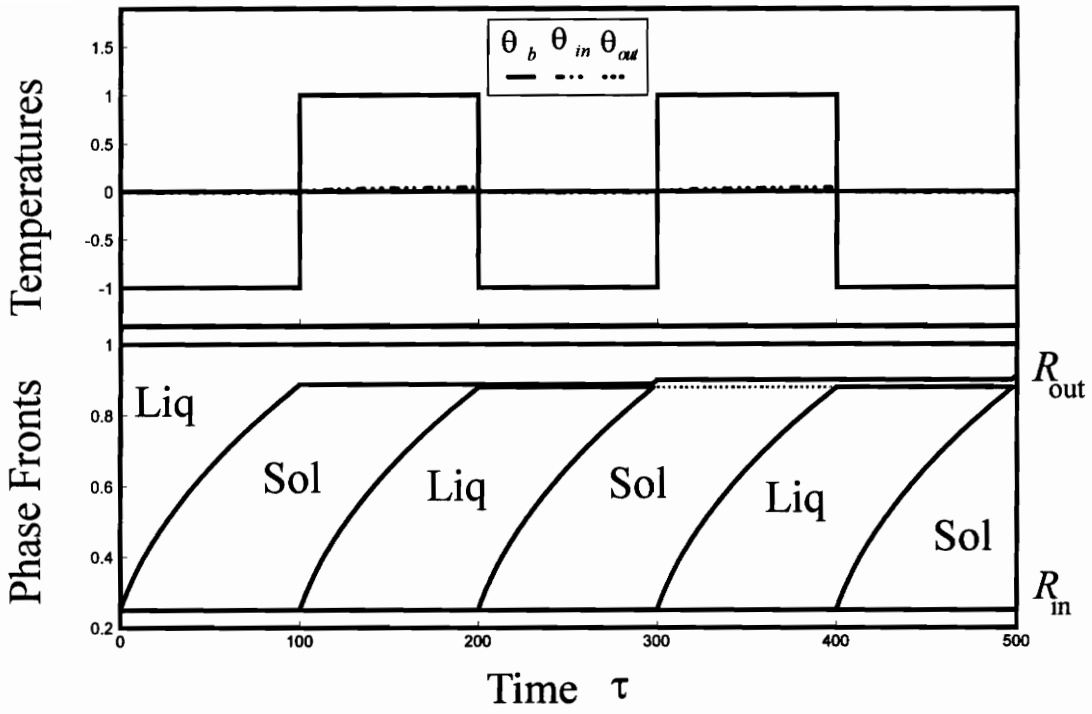

Figure 2.8: Time evolution of temperatures and phase front positions for *low* Biot number

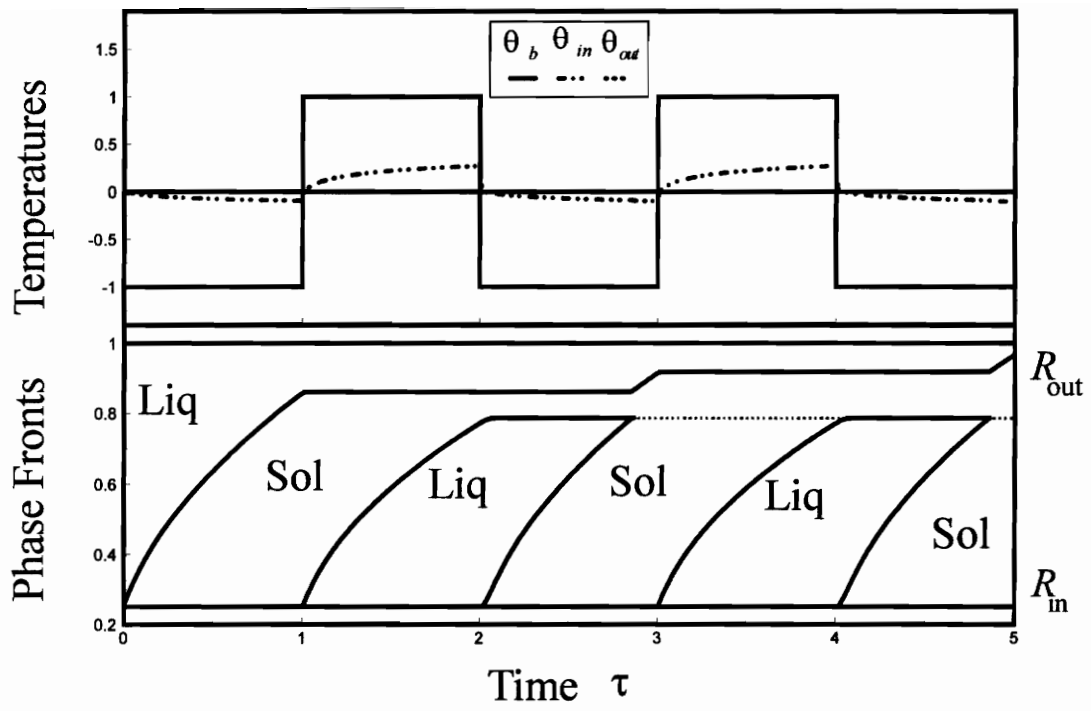

Figure 2.9: Time evolution of temperatures and phase front positions for *high* Stefan number

environment and propagates towards the outer surface. And all the other results are analogous to Fig. 2.5.

CHAPTER 3 AXISYMMETRIC PROBLEMS USING BEM

3.1 PROBLEM FORMULATION

As shown in Fig. 3.1, the problem under investigation involves two-dimensional axisymmetric heat transfer in a finite medium. A pure substance with freezing and melting temperature of T_{fr} is contained between two concentric cylindrical walls of length L. The outside wall is thin and insulated and has a radius of r_{out}. The tube wall has inside and outside radii of r_{pi} and r_{po}. There is a fluid of bulk temperature $T_b(z,t)$ and mass flow rate of $\dot{m}(t)$ flowing inside the tube. The fluid enters the tube at the temperature of $T_{b,in}$ and leaves the pipe at $T_{b,out}$. The inlet temperature $T_{b,in}$ cycles across T_{fr} of the PCM. As a result, the temperature $T_{po}(z,t)$ at r_{po} changes back and forth across the T_{fr}. This changing $T_{po}(z,t)$ causes alternating layers of solid and liquid to form and propagate from the tube outside surface.

3.1.1 General Energy Equations for Axisymmetric Problems

Assume that the PCM, tube and the fluid in the tube all start at a uniform temperature T_{init}. As shown in Fig. 3.2, j is used to designate a general layer of the PCM. Newly formed layers are numbered sequentially from the tube wall. For a general two-dimensional transient axisymmetric heat transfer problem, the energy equation based on

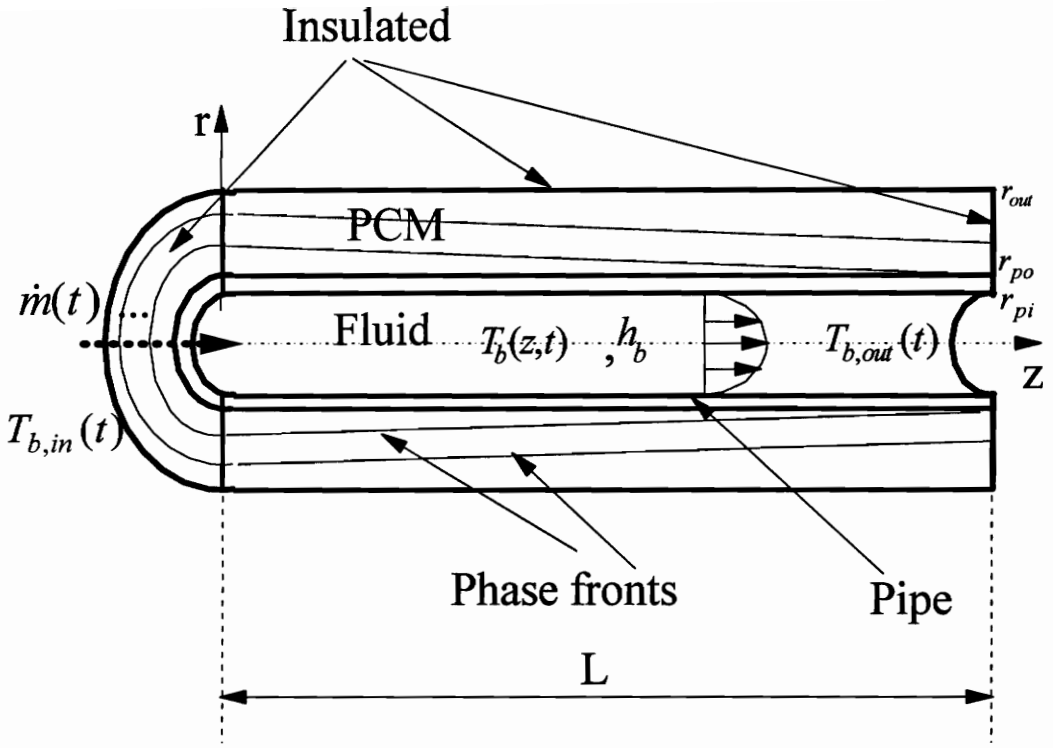

Fig. 3.1: A typical tube showing the details of boundary/inlet conditions

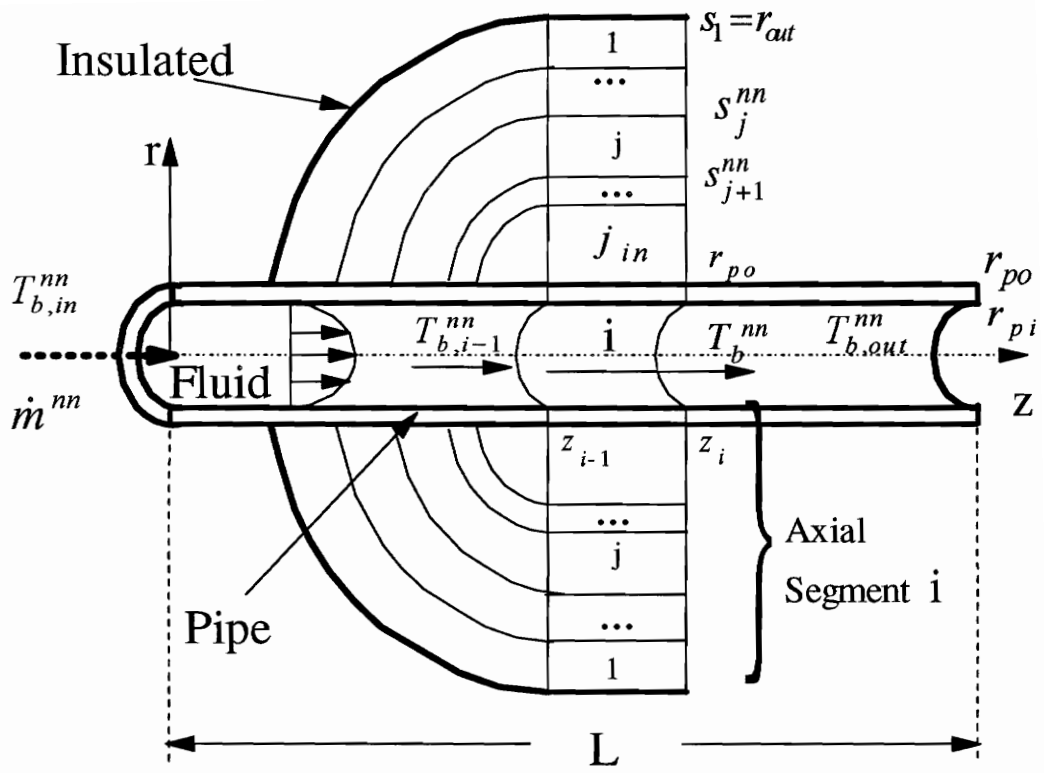

Fig. 3.2: A typical tube showing details of axial segment i

the energy balance of a control volume in the fluid, the pipe wall or the PCM region can be expressed as,

$$\frac{1}{r}\frac{\partial}{\partial r}\left(r\frac{\partial T_j}{\partial r}\right)+\frac{\partial^2 T_j}{\partial z^2}=\frac{1}{\alpha_j}\left(u_z\frac{\partial T_j}{\partial z}+u_r\frac{\partial T_j}{\partial r}+\frac{\partial T_j}{\partial t}\right) \qquad (3.1)$$

where subscript j represents different PCM layers, the pipe wall or the fluid; u_z and u_r represent the velocities in axial and radial directions.

3.1.2 Equations in the Fluid

It is assumed that axial conduction is negligible and fully developed conditions exist. Since there is no radial direction flow for fully developed flow, the energy equation of the fluid can be reduced from eqn.(3.1) as:

$$\frac{1}{r}\frac{\partial}{\partial r}\left(r\frac{\partial T_f}{\partial r}\right)=\frac{1}{\alpha_f}\left(u_z\frac{\partial T_f}{\partial z}+\frac{\partial T_f}{\partial t}\right) \qquad (3.2)$$

with the initial and inlet conditions as,

$$\begin{aligned} T_f &= T_{init.}, \quad t=0 \\ T_f &= T_{b,in}(t), \quad z=0 \end{aligned} \qquad (3.3)$$

Here, T_f represent the local temperature of fluid and is a function of r, z and t.

Integrating eqn.(3.2) over the cross section of the tube and using the axisymmetric condition at $r=0$ results in,

$$\pi r_{pi}^2(\rho c_p)_b\frac{\partial T_m}{\partial t}+(\dot{m}c_p)_b\frac{\partial T_b}{\partial z}=k_f\left(\frac{\partial T_f}{\partial r}\right)_{r=r_{pi}} \qquad (3.4)$$

where T_b is the bulk temperature and T_m is the mean temperature in terms of transient capacity or heat storage, defined as,

$$T_b = \frac{\int_0^{r_{pi}} (\rho c_p)_b u_z T_f(r,z,t) dA}{\int_0^{r_{pi}} (\rho c_p)_b u_z dA} = \frac{\int_0^{r_{pi}} (\rho c_p)_b u_z T_f(r,z,t) dA}{\dot{m}(t) c_p} \qquad (3.5)$$

$$T_m = \frac{\int_0^{r_{pi}} (\rho c_p)_b T_f(r,z,t) dA}{\int_0^{r_{pi}} (\rho c_p)_b dA} \qquad (3.6)$$

where A represents the cross sectional area of the tube.

As shown in eqn.(3.5) and eqn.(3.6), T_b is the mean temperature at a given cross section and is defined in terms of the thermal energy transported with the bulk motion of the fluid as it moves past the cross section. The temperature T_m is the average temperature defined in terms of the lumped capacity of the fluid. T_b and T_m are different since the velocity is involved in T_b and is not involved in T_m. For the problems under investigation, T_b is used to replace T_m approximately to reduce the number of unknowns in the equations.

While the energy equation is defined in eqn.(3.4), the convective boundary condition between the fluid and the pipe wall can be expressed as,

$$h_b\left(T_b - T_{pi}\right) = -k_p \frac{\partial T_p}{\partial r} = -k_f \frac{\partial T_f}{\partial r}, \quad r = r_{pi} \qquad (3.7)$$

where T_{pi} represents the tube inside surface temperature and the forced convection heat transfer coefficient h_b is calculated using empirical correlations for laminar or turbulent flow.

Substituting eqn.(3.7) and replacing T_m with T_b reduces eqn.(3.4) to,

$$\pi r_{pi}^2 (\rho c_p)_b \frac{\partial T_b}{\partial t} + (\dot{m} c_p)_b \frac{\partial T_b}{\partial z} = 2\pi r_{pi} h_b \left[T_{pi}(z,t) - T_b(z,t) \right] \qquad (3.8)$$

3.1.3 Equations in the PCM

It is assumed that convection (low Rayleigh number) and axial conduction (long thin geometry) are all neglected in the PCM region. Thus, the energy equation eqn.(3.1) can be reduced to,

$$\frac{1}{r}\frac{\partial}{\partial r}\left(r \frac{\partial T_j}{\partial r} \right) = \frac{1}{\alpha_j} \frac{\partial T_j}{\partial t}, \text{ in layer j} \qquad (3.9)$$

with the initial condition of,

$$T_j = T_{init}, \quad t = 0 \qquad (3.10)$$

The appropriate boundary conditions for this conduction problem are described as follows,

1. At the *outside wall surface*, the wall is insulated,

$$\frac{\partial T_j}{\partial r} = 0, \quad j = 1, \; r = r_{out} \qquad (3.11)$$

2. At a *moving front*, the difference between the conduction heat transfer terms is the latent energy,

$$\left.\begin{aligned} -k_l \frac{\partial T_l}{\partial r} &= -k_s \frac{\partial T_s}{\partial r} + \rho h_{if} \frac{\partial s_j}{\partial t} \\ T_j &= T_{j-1} = T_{fr} \end{aligned}\right\} \quad at\ r = s_j(z, t),\ j = 2..., j_{in} \qquad (3.12)$$

where $s_j(z,t)$ is the location of phase boundary j.

3. At a *stationary boundary* which separates two layers of the same phase, which arises from the merging of two phase fronts, conservation of energy and continuity of temperature require,

$$k_j \frac{\partial T_j}{\partial r} = k_{j-1} \frac{\partial T_{j-1}}{\partial r}, \quad \text{at } r = s_j \qquad (3.13)$$

$$T_j(r,t) = T_{j-1}(r,t), \qquad at\ r = s_j \qquad (3.14)$$

3. At the pipe outside surface:

$$\left.\begin{aligned} -k_p \frac{\partial T_p}{\partial r} &= -k_{j_{in}} \frac{\partial T_{j_{in}}}{\partial r} \\ T_{j_{in}} &= T_{po} \end{aligned}\right\} \quad \text{at } r = r_{po} \qquad (3.15)$$

where T_{po} represents the pipe temperature at $r = r_{po}$, j_{in} represents the layer adjacent the tube.

The convective boundary condition at the tube inside surface which connects the fluid and the tube is given by eqn.(3.7).

3.2 SOLUTION

By neglecting axial conduction, the tube of total length L may be divided into I_{out} axial segments of length Δz as shown in Fig. 3.2. All quantities are assumed uniform over each segment. Radially one-dimensional heat transfer is assumed for the alternating liquid/solid layers and the tube wall in each axial segment. The problem can then be solved as a sequence of radially one-dimensional problems in each axial segment. Each axial segment communicates with downstream segments through the fluid flowing inside the tube as shown in Fig. 3.2.

After discretization in the axial direction, all the governing equations (3.7)-(3.13) still keep the same form except all quantities in each axial segment should have a subscript i representing the i_{th} axial segment. For convenience, all the subscript i's are dropped in the following expressions and all the quantities are assumed to be of the i_{th} axial segment unless mentioned specifically.

3.2.1 Time and Axial Discretization of Fluid Energy Equation

Referring to Fig. 3.2 and Fig. 3.3, the fluid energy equation, eqn.(3.8), can be discretized in time and in the axial direction. The fully implicit scheme is employed in

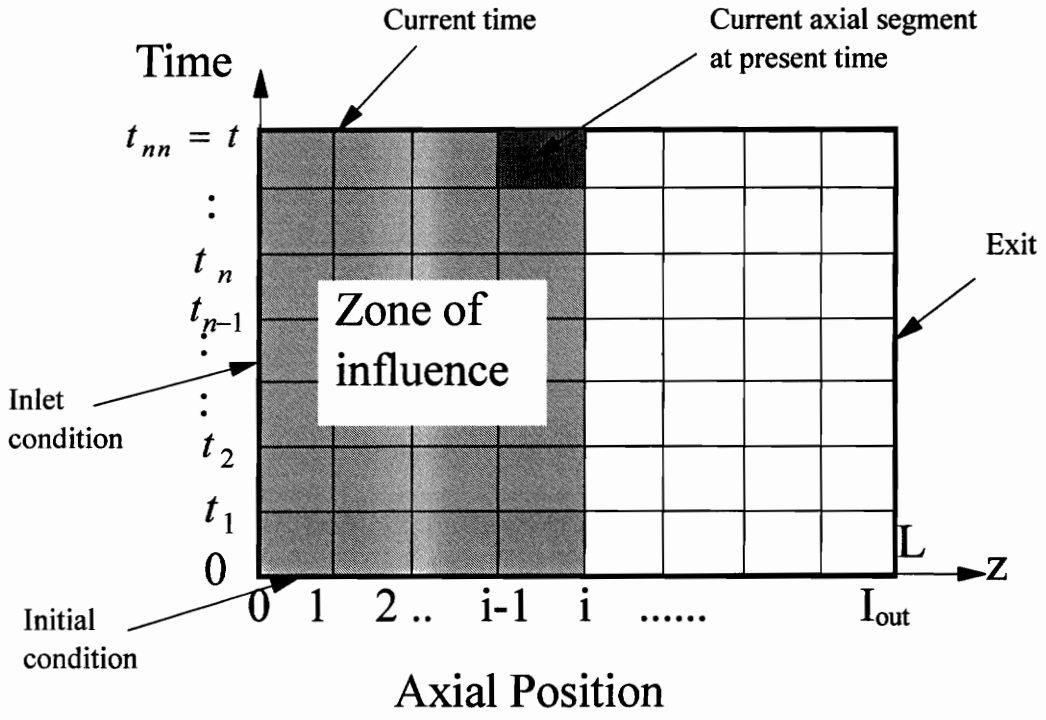

Fig. 3.3: Discretization in axial direction and time

both the time and the axial variables to ensure unconditionally stable results. The discretized form of the fluid energy equation, eqn.(3.8), can be expressed as:

$$\pi r_{pi}^2 (\rho c_p)_b \frac{(T_b^{nn} - T_b^{nn-1})}{\Delta t} + (\dot{m} c_p)_b \frac{(T_b^{nn} - T_{b,i-1}^{nn})}{\Delta z} = 2\pi r_{pi} h_b (T_{pi}^{nn} - T_b^{nn}) \qquad (3.16)$$

3.2.2 General BEM Solution of One-dimensional Problem in Cylindrical Systems

Referring to Chapter 2, the discretized form of general solution for this layer is:

$$\frac{\lambda}{2\pi\alpha_j} T_j^{nn}(r) = F_j(z,t)$$
$$+ \sum_{n=n_j+1}^{nn} \left(r_0 \left(\frac{\partial T_j}{\partial r_0} \right)^n (GI)^n - T_j^n r_0 (HI)^n + T_{fr} V_{r_0 j}^{\ n} (GI)^n \right)_{r_0 = s_j(t_0)} \qquad (2.27)$$
$$- \sum_{n=n_j+1}^{N} \left(r_0 \left(\frac{\partial T_j}{\partial r_0} \right)^n (GI)^n - T_j^n r_0 (HI)^n + T_{fr} V_{r_0 j}^{\ n} (GI)^n \right)_{r_0 = s_{j+1}(t_0)}$$

where

$$\lambda = \begin{cases} \frac{1}{2} & , \quad r = s_j^{nn} \text{ or } r = s_{j+1}^{nn} \\ 1 & , \quad r \neq s_j^{nn} \text{ and } r \neq s_{j+1}^{nn} \end{cases} \qquad (2.24)$$

and

$$F_j(r,t) = \begin{cases} 2\pi \int_{s_j(t_0)}^{s_{j+1}(t_0)} r_0 G_j T_{init} dr_0 & , \text{ for pipe wall at } t_0 = 0 \text{ or } j = 1 \text{ at } t_0 = 0 \\ 0 & , \text{ elsewhere} \end{cases}$$

(2.20)

Here V_{r_0} is the velocity of a moving front, λ represents the shape coefficient and F_j represents the influence of initial conditions. $(GI)^n$ and $(HI)^n$ act as the influence coefficients.

Thus, for each PCM layer j or the tube wall at current time step nn, two simultaneous equations can be obtained by evaluating the eqn.(2.27) at both boundaries of this layer $r = s_{j+1}^{nn}$ and $r = s_j^{nn}$. These equations can be written in matrix form as,

$$\mathbf{A_j U_j = B_j} \qquad (2.28)$$

and $\mathbf{B_j}$ accounts for the history of this layer that depends on geometrical data, properties of the medium, the time step, the values of unknowns at the previous time steps and the initial condition of this layer.

For a layer with no moving front, such as the tube surfaces, the outer wall surface, the unknowns U_{j1} and U_{j2} could be temperature or heat flux depending on the boundary conditions. For a layer with one or more moving fronts, the unknowns at a moving front should be the heat flux because the temperature is locked to the freezing temperature T_{fr} of the PCM and the front location should be determined through iteration. For a fixed boundary separating two layers of the same phase, the temperature is assumed first and is determined through iteration based on the continuity of heat flux through this boundary.

The discretized form of the energy balance at a moving boundary, eqn.(3.12) can be expressed as,

$$\left[(s_j^{nn})^2-(s_j^{nn-1})^2\right]\rho h_{if} \pm 2s_j^{nn}\left[k_j\left(\frac{\partial T_j}{\partial r}\right)^{nn}-k_{j-1}\left(\frac{\partial T_{j-1}}{\partial r}\right)^{nn}\right]=0\ ,\ \text{at r}=\text{s}_\text{j}^{\text{nn}} \qquad (2.30)$$

3.2.3 Computational Algorithm

The problem under investigation begins as a single layer of either liquid or solid with a uniform temperature of T_{init}. The tube inside wall is subjected to a convective environment with specified time variation of the fluid inlet conditions of $T_{bin}(t)$ and $\dot{m}(t)$.

To solve this problem, time and axial discretizations are employed. The calculation is carried out as follows:

1. Start at the initial conditions.
2. March one time step.
3. Solve the radially one-dimensional problem in the first axial segment and march to next axial segment until the exit is reached. An axial segment communicates with downstream segments through the fluid flowing inside the tube.
4. March to next time step and repeat step 3.

As indicated in Fig. 3.3, at axial segment i and time step nn, the inlet temperature is the outlet of section $i-1$ and all variables before time step nn are already known. The variables are determined only by the values before time step nn and the outlet temperature of previous axial segment $i-1$. This is shown as a shadowed *Zone of Influence* in Fig. 3.3.

At each time step, no configuration change is assumed at first for all the axial segments and the routine will detect all possible configuration changes and carry out the calculation based on the new configuration.

In a typical axial segment i, the unknowns for each PCM layer involve a combination of temperatures, heat fluxes and the phase front positions depending on the boundary conditions of the layer considered. As the boundary condition of a moving front is highly nonlinear, an iterative scheme is applied for the moving front positions. Newton's method is employed in determination of a phase front position for a moving boundary and of the temperature for a boundary separating two layers of same phase. After getting the converged results for all the layers, a check is performed to determine if configuration change(s) arises. If there is more than one configuration change at the same time step, the code will deal with them one by one. The possible configuration changes are:

1. The outer tube wall surface temperature crosses the freezing temperature T_{fr}, a new layer forms.
2. A phase front consumes an adjacent layer and merges with another phase boundary, producing a stationary composite boundary which separates two layers of the same phase.

After solving axial segment i at time step nn, the solution proceeds to the next axial segment with the outlet temperature of section i as the inlet of section $i+1$ to get

the solution for the whole tube. Then the solution marches in time to get the solution for the next time step.

To simplify the calculation, the freezing temperature takes the value of zero. This simplification does not reduce the generality of this method.

3.3 RESULTS

The results of this investigation are presented with dimensionless parameters defined in the nomenclature. The governing equations are shown in Fig. 3.4 in both dimensional and dimensionless expressions, referring to Tables 3.1 and 3.2. To illustrate the influence of the sensible energy, a Stefan number of $Ste = 1.0$ which is very high for a thermal energy storage system is chosen in this sample case.

3.3.1 Numerical Behavior

In current research, cases with different Stefan numbers, Biot numbers, initial temperatures, and Peclet numbers were tested against results of the thermal network method (TNM) and the negligible sensible heat approximation method (NSH) by comparing the fluid exit temperatures and the latent state-of-charges. The geometry, properties and the parameters of the sample case are listed in Table 3.3. The agreement between the results from the BEM model and the TNM model were excellent for low Stefan number cases and good for high Stefan numbers cases. The sample results given in the following section for cases with multiple fronts around the tube are generated

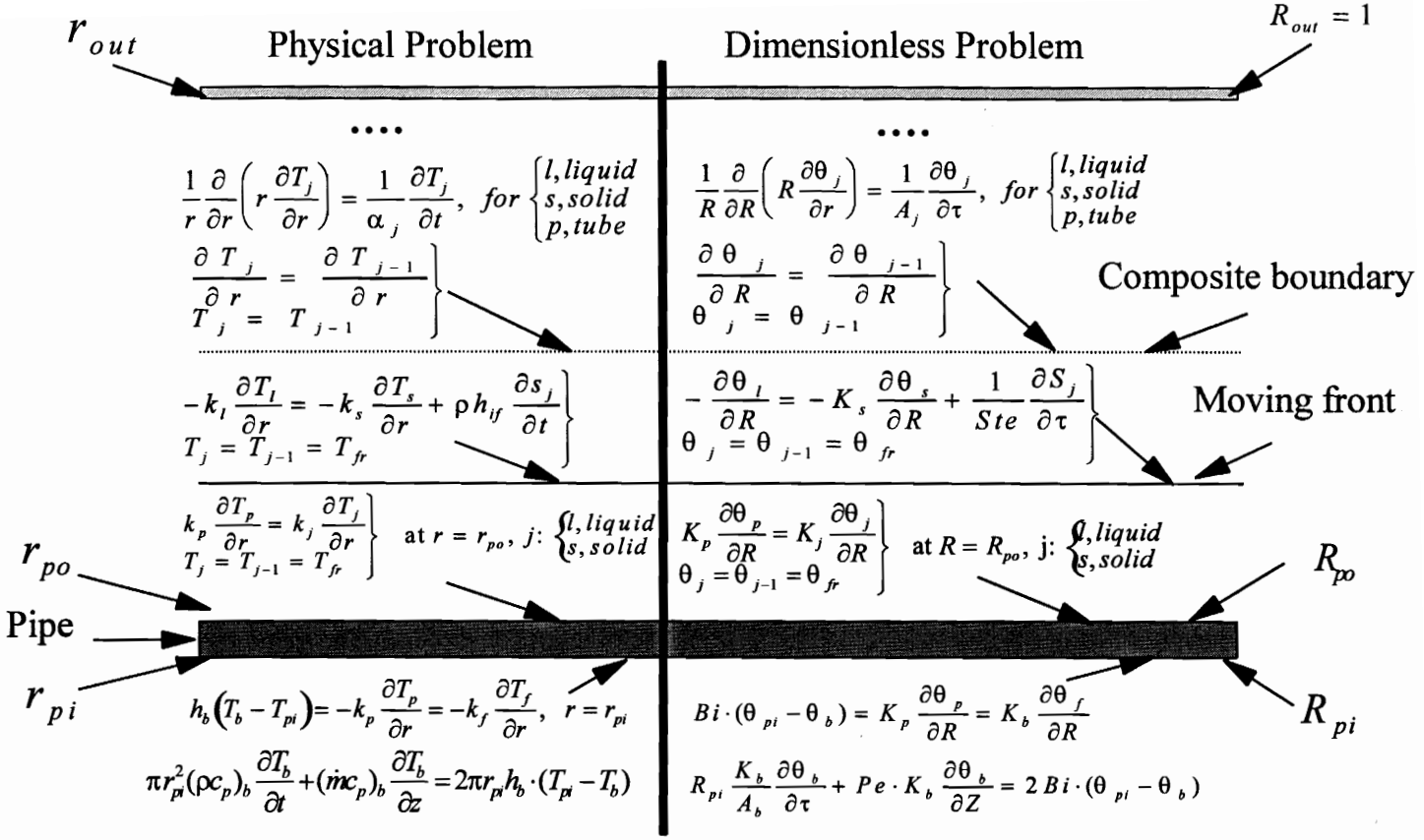

Fig. 3.4: Dimensional and dimensionless governing equations for axial segment i

TABLE 3.1: DEFINITION OF DIMENSIONAL AND DIMENSIONLESS PHYSICAL VARIABLES

Definition	Physical Variables	Dimensionless Variables	Definition of Dimensionless Variables
Time	t	$\tau = \alpha t / r_{out}^2$	Time
Radial Location	r	$R = r / r_{out}$	Radial Location Ratio
Axial Location	z	$Z = z / r_{out}$	Dimensionless Axial Location
Temperature	$T(r,z,t)$	$\theta(R,Z,\tau) = \frac{T(r,z,t) - T_{fr}}{T_h - T_{fr}}$	Temperature Ratio
Fluid Bulk Tempearture	$T_b(z,t)$	$\theta_b(Z,\tau) = \frac{T_b(z,t) - T_{fr}}{T_h - T_{fr}}$	Fluid Bulk Tempearture
Temperature at r_{pi}	$T_{pi}(z,t)$	$\theta_{pi}(Z,\tau) = \frac{T_{pi}(z,t) - T_{fr}}{T_h - T_{fr}}$	Temperature at R_{pi}
Temperature at r_{po}	$T_{po}(z,t)$	$\theta_{po}(Z,\tau) = \frac{T_{po}(z,t) - T_{fr}}{T_h - T_{fr}}$	Temperature at R_{po}
Temperature at r_{out}	$T_{out}(z,t)$	$\theta_{out}(Z,\tau) = \frac{T_{out}(z,t) - T_{fr}}{T_h - T_{fr}}$	Temperature at R_{out}
Moving Front Location	$s_j(z,t)$	$S_j(Z,\tau) = s_j(z,t) / r_{out}$	Moving Front Location
Heat Flux at a Boundary	$q_j'' = -k_j \frac{\partial T}{\partial r}$	$-K_j \frac{\partial \theta}{\partial R}$	Heat Flux at a Boundary
Convective Heat Flux at r_{pi}	$q_p'' = h \cdot (T_{pi} - T_b)$	$Bi \cdot (\theta_{pi} - \theta_b)$	Convective Heat Flux at R_{pi}

TABLE 3.2: DEFINITION OF DIMENSIONAL AND DIMENSIONLESS PARAMETERS

Definition	Physical Parameters	Dimensionless Parameters	Definition of Dimensionless Parameter
High, Low Inlet Temperatures	T_h, T_{low}	+1,−1	High, Low Inlet Temperatures
Initial and Inlet Temperature	T_{init}, $T_{b,in}$	θ_{init}, $\theta_{b,in}$	Initial Temperature
Convection Coefficient	h_b	$Bi = \frac{h_b r_{out}}{k_l}$	Biot Number
Volume Latent Heat	ρh_{if}	$Ste = \frac{(\rho c_p)_l (T_h - T_{fr})}{\rho_l h_{if}}$	Stefan Number
Fluid Average Velocity	$\overline{U}$	$Pe = \frac{\overline{U} r_{pi}}{\alpha_b}$	Peclet Number
Conductivity of Liquid	k_l	1	Reference Conductivity
Conductivity of Solid	k_s	$K_s = \frac{k_s}{k_l}$	Conductivity Ratio
Conductivity of Tube	k_p	$K_p = \frac{k_p}{k_l}$	Conductivity Ratio
Conductivity of Fluid	k_b	$K_b = \frac{k_b}{k_l}$	Conductivity Ratio

(to be continued)

TABLE 3.2: DEFINITION OF DIMENSIONAL AND DIMENSIONLESS PARAMETERS (continued)

Thermal Diffusivity of Liquid	α_l	1	Reference Thermal Diffusivity
Thermal Diffusivity of Solid	α_s	$A_s = \frac{\alpha_s}{\alpha_l}$	Thermal Diffusivity Ratio
Thermal Diffusivity of Tube	α_p	$A_p = \frac{\alpha_p}{\alpha_l}$	Thermal Diffusivity Ratio
Thermal Diffusivity of fluid	α_p	$A_b = \frac{\alpha_b}{\alpha_l}$	Thermal Diffusivity Ratio
Outer Wall Radius	r_{out}	1	Reference Length
Tube Wall Outer Radius	r_{po}	$R_{po} = \frac{r_{po}}{r_{out}}$	Radius Ratio
Tube Wall inside Radius	r_{pi}	$R_{po} = \frac{r_{pi}}{r_{out}}$	Radius Ratio

TABLE 3.3: GEOMETRY, PROPERTY RATIOS AND THE PARAMETERS FOR THE SAMPLE CASE:

Geometry	$R_{pi} = 0.2$; $R_{po} = 0.25$; $R_{out} = 1$; $Lz = 3000$
Thermal Diffusivity Ratios	$A_l = 1$; $A_s = 8.60$; $A_p = 1.70$; $A_b = 0.21$
Thermal Conductivity Ratios	$K_l = 1$; $K_s = 3.88$; $K_p = 0.88$; $K_b = 0.20$
Stefan Number	$Ste = 1.0$
Peclet Number	$Pe = 10^4$
Biot Number	$Bi = 1.0$
Initial Temperature	$\theta_{init} = 0.0+$

using 20 time steps for each heating or cooling period and 21 segments in the axial direction and represent results independent of the time step and the axial segment sizes. Figure 3.5 shows the outlet temperature and the latent state of charge (L-SOC) using different time steps and axial segment sizes. The first case has 20 time steps in each freezing/melting period and 21 axial segments while the second case has 10 time steps in each period and 11 axial segments. The results prove to be consistent and accurate.

3.3.2 Sample Results

To illustrate this method, water is used as the PCM. A sample case is chosen as (see Table 3.3), $Bi = 1$, $Ste = 1.0$, $Pe = 10^4$, $\theta_{init} = \theta_{fr} = 0.0+$, $\Delta\tau = 0.05$, and the driving temperature $\theta_{b,in}$ switches between cold (-1) and hot $(+1)$. The property ratios are chosen as, $A_s = 8.60$, $A_p = 1.70$, $A_b = 0.21$, $K_s = 3.88$, $K_p = 0.88$, $K_s = 0.20$. The dimensionless inside and outside radiuses of the tube are set to $R_{pi} = 0.20$, $R_{po} = 0.25$. The outer wall surface radius is $R_{out} = 1.0$. The dimensionless length of tube is set to $Lz = 3000$. The tube is divided into $I_{out} = 21$ axial segments with equal length of $\Delta Z = Lz / I_{out}$. For illustration, the two cycling periods are the same ($\tau_c = \tau_h$) with 20 time steps in each cycling period.

Figures 3.6 to 3.8 give the time evolution of temperatures and phase fronts at three different axial locations. In each figure, the bottom portion shows the radial position of each front varying with time. When one front overtakes another, a layer between them

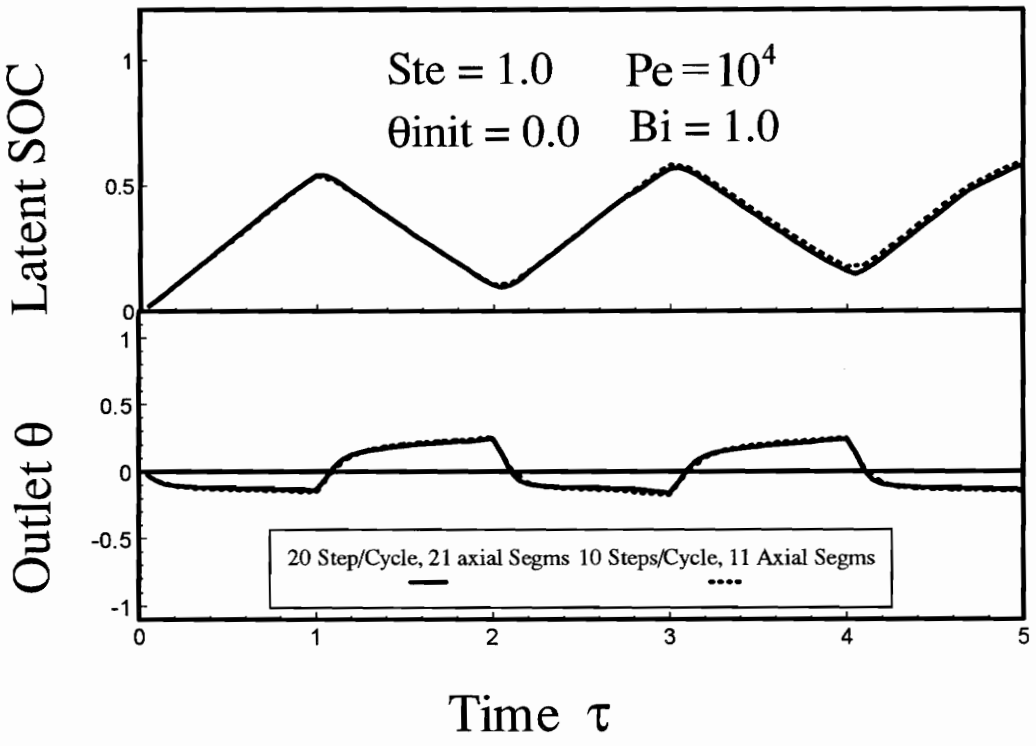

Fig. 3.5: Numerical behavior of the BEM algorithm with different time steps and axial segment sizes

is consumed and the front separating these two adjacent layers is fictitious (shown as a dotted line) because these two layers are of a same phase. When a moving front reaches the upper limit ($S_j^{nn} = 1.0$), the layer adjacent to the outer wall surface is consumed. All the phase fronts are represented with solid lines except for the fictitious boundaries. The liquid and solid layers are labeled in each region with Liq or Sol representing liquid or solid respectively. The top portion shows the variation of the tube inlet temperature, fluid bulk temperature at this segment and tube outer surface temperature. A new layer forms when θ_{po} crosses the freeze temperature of the PCM ($\theta_{fr} = 0.0$).

Figure 3.6 shows the variation of temperatures and the phase fronts at the exit of the first axial segment $i = 1$. The hot and cold periods are $\tau_c = \tau_h = 1$. The PCM starts as an all liquid layer at an initial condition of $\theta_{init} = 0.0$. At time $\tau = 0$, the inlet temperature is set to $\theta_{b,in} = -1$. The first freeze phase front starts at the first time step. Because of the higher conductivity of the ice and no stored sensible energy at the initial condition, this freeze front reaches the outer boundary and consumes the whole liquid layer before the inlet temperature $\theta_{b,in}$ switches. The PCM becomes one layer of solid and is subcooled quickly until the melting period begins. At time $\tau = 1$, the inlet temperature switches to $\theta_{b,in} = +1$. Because of the subcooling of the PCM and the high Stefan number, the energy stored in the subcooled solid slows down the formation and propagation of the liquid layer. This first melt front starts late at the second time step of this melting period, $\tau = 1.10$ and does not reach the outer wall at the end of this period

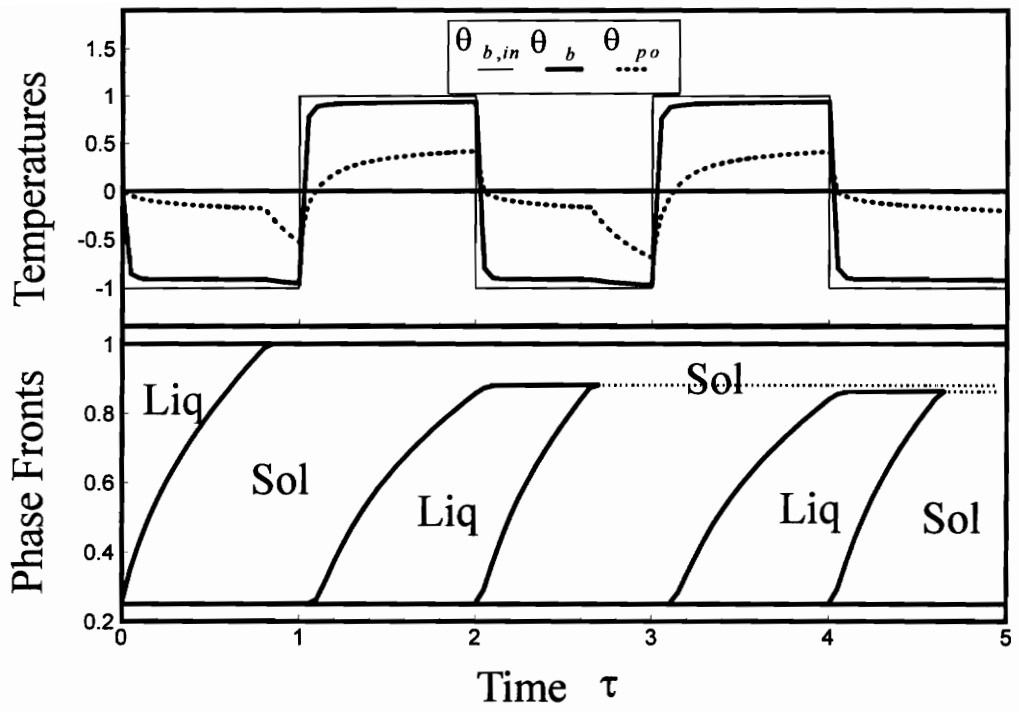

Fig. 3.6: Time evolution of temperatures and phase fronts at the exit of the first axial segment (i = 1, Z=142.86); parameters are listed in Table 3.3

because of the sensible energy stored in the first solid layer and the lower conductivity of liquid. Thus, there is less energy stored in this liquid layer. In the next freezing period, the freezing front overtakes the first melting front, consumes the liquid between the two solid layers. Thus, the PCM becomes two layers of solid separated by a fictitious boundary for numerical purposes. This boundary is shown as dotted line. The PCM is subcooled more than in the first freezing period until the fluid temperature switches back to $\theta_{b,in} = +1$ at time $\tau = 3$. The second melt front starts at the third time step of this melting period, $\tau = 3.15$, and thus propagates slower than the first melting front. Because of more stored sensible energy in the solid layers and lower conductivity and diffusivity of the liquid, this melt front propagates slightly less than previous melting front. The next cooling period starts at $\tau = 4$ and the third freeze front starts at the first time step of the freezing period and overtakes the previous melt front.

Figure 3.7 shows the variation of temperatures and the phase fronts at the exit of the middle axial segment, $i = 11$. The behavior of the freezing and melting fronts are similar to those in Fig. 3.6. Because of the energy transferred in the upstream axial segments, the driving potentials in both freezing and melting periods decrease quickly in this case. Thus, the first freezing front is far away from the outer wall. Because the fluid driving potential is smaller, and thus less sensible energy is stored, the PCM never gets to a fully charged or discharged condition (becomes all liquid or all solid). The influence of sensible energy is not apparent in this segment. Even though the driving potential in

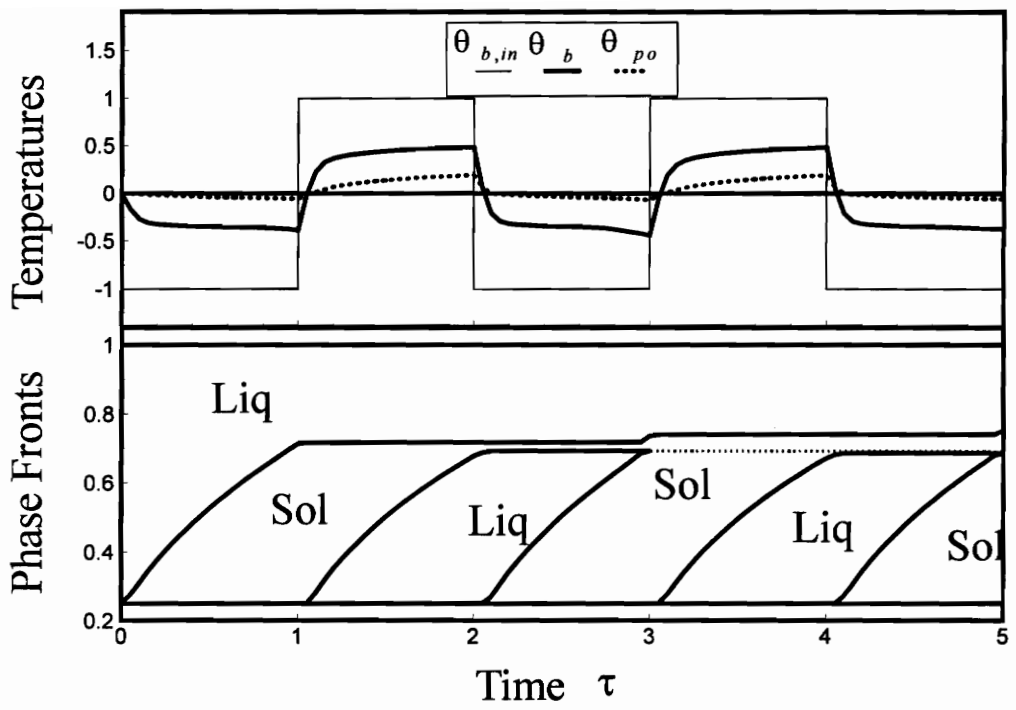

Fig. 3.7: Time evolution of temperatures and phase fronts at the exit of the middle axial segment (i = 11, Z=1571.42); parameters are listed in Table 3.3

the freezing period decreases faster than that in the melting period, the freezing fronts still propagate faster than the melting fronts. It is hard to notice that all the temperatures have a slight time delay in responding to the inlet temperature since the tube is long and it needs time to propagate the inlet condition downstream to this segment. This phenomenon could be exaggerated for cases with low Peclet numbers.

Figure 3.8 shows the temperature and phase front curves at the outlet of the tube, $i = 21$. In this axial segment, the fluid temperature has a longer time delay than that in segment $i = 11$. Since the absolute value of the fluid temperature is much closer to the freeze temperature of the PCM than that in previous segment $i = 11$, the phase front propagates much slower than in segment $i = 11$. Even though the fluid has lower conductivity and the first solid layer has some stored sensible energy, the melting fronts overtake the first freeze fronts in the melting cycles. This is because the fluid driving potential in the freezing period decreases faster than that in the melting period. Thus, the driving potential difference of the fluid in the melting and freezing periods is large enough to cause the melt front to overtake the freeze front in this segment. The PCM is then heated to store more sensible energy. Because of this, the second freeze front starts late at the fourth time step in this freezing period, $\tau = 2.2$. Because the driving potential is relatively small in this segment, the stored sensible energy in the liquid plays a important role in slowing down the formation of the freeze fronts.

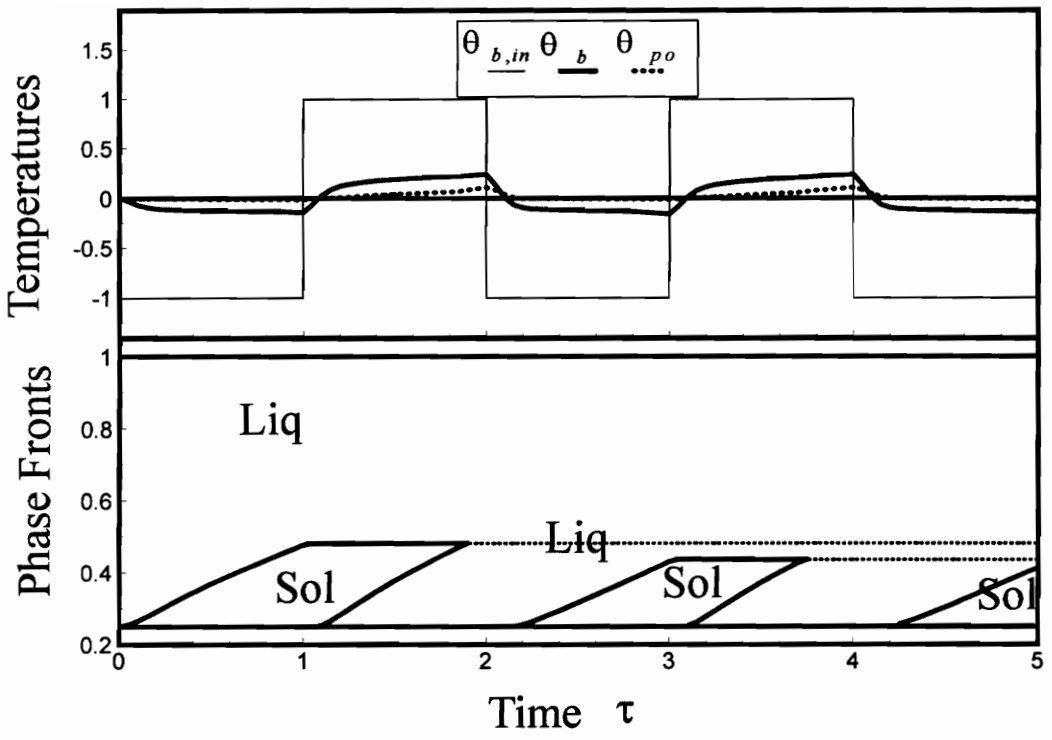

Fig. 3.8: Time evolution of temperatures and phase fronts at the exit of the tube (i = 1, Z=3000); parameters are listed in Table 3.3

Figures 3.9 to 3.13 are snapshots of the freeze and melt front distributions around the tube taken in the middle of each heating/cooling period. These figures are not to scale in geometry and the radial direction scale is strongly exaggerated for illustration. The physical ratio of axial scale to radial scale should be 3000:1.

Figure 3.9 shows the freeze front distribution along the tube at time $\tau = 0.5$, in the middle of the first freezing period. The stepwise pattern is a representation of the fully implicit axial discretization. There are a total of 21 axial segments.

Figure 3.10 shows the front distributions at $\tau = 1.5$, in the middle of the first melting period. Note that the melt front at the entrance of the tube is slowed down since the freeze front reached the outer wall surface. The solid layer at the entrance was subcooled and the stored sensible energy slows down the formation of the melt front.

Figure 3.11 shows the distributions at $\tau = 2.5$, in the middle of the second cooling period. Note that the melting front is overtaking the freezing front at this moment. Due to the energy transferred in upstream axial segments, the driving potential of the fluid in the melting period is larger than that in the freezing period at the latter portion of the tube. This causes the melt front to overtake the freeze front. The fictitious boundary separating two layers of the phase is shown as a dotted line.

Figure 3.12 shows the front distributions in the middle of the second melting period, $\tau = 3.5$. The second freeze front overtook the first melt front over approximately the first half of the tube and subcooled the solid in the first five segments, drove the first

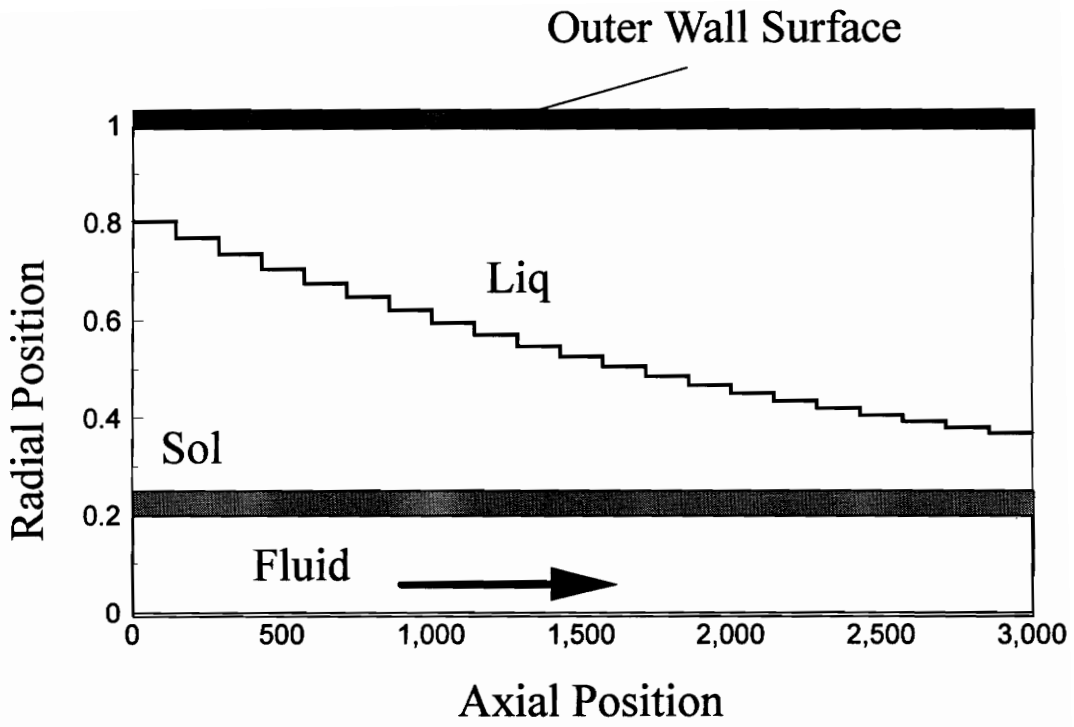

Fig. 3.9: Moving front distribution in the middle of the first freezing period ($\tau = 0.5$, nn = 10); parameters are listed in Table 3.3

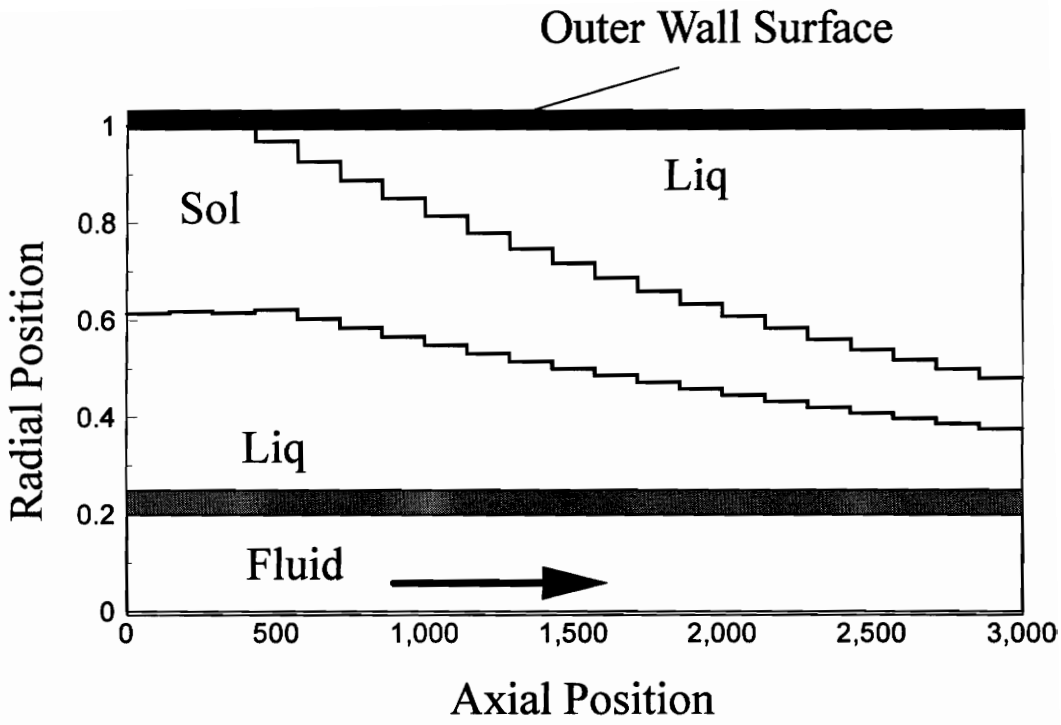

Fig. 3.10: Moving front distribution in the middle of the first melting period ($\tau = 1.5$, nn = 30); parameters are listed in Table 3.3

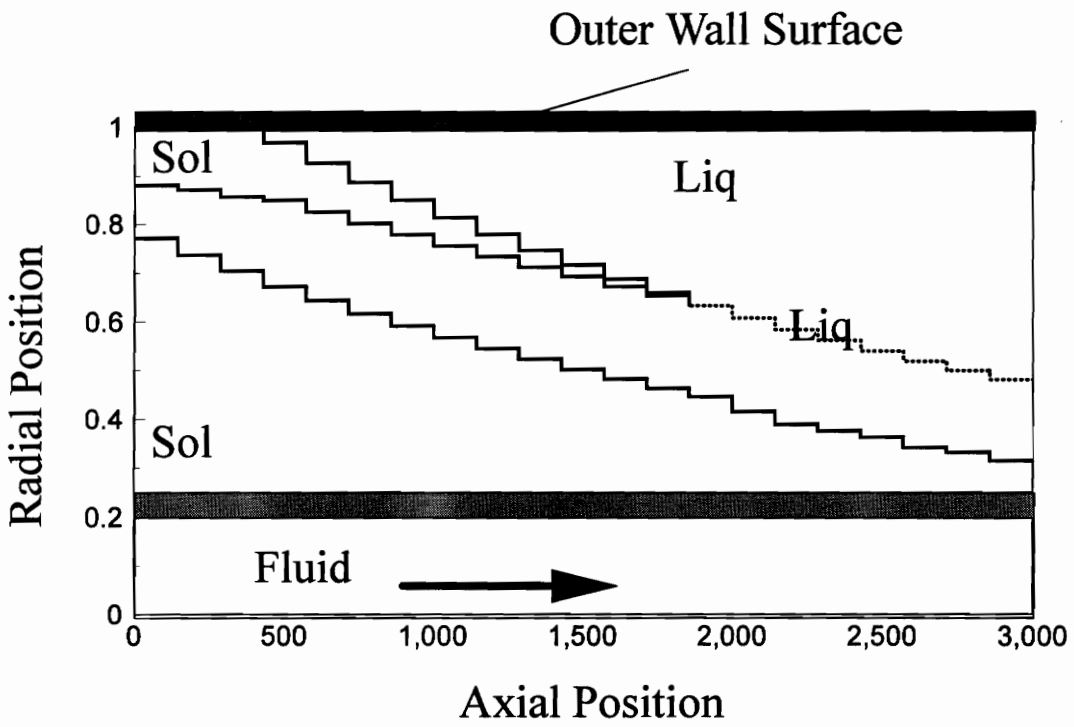

Fig. 3.11: Moving front distribution in the middle of the second freezing period ($\tau = 2.5$, nn = 50). Parameters are listed in Table 3.3

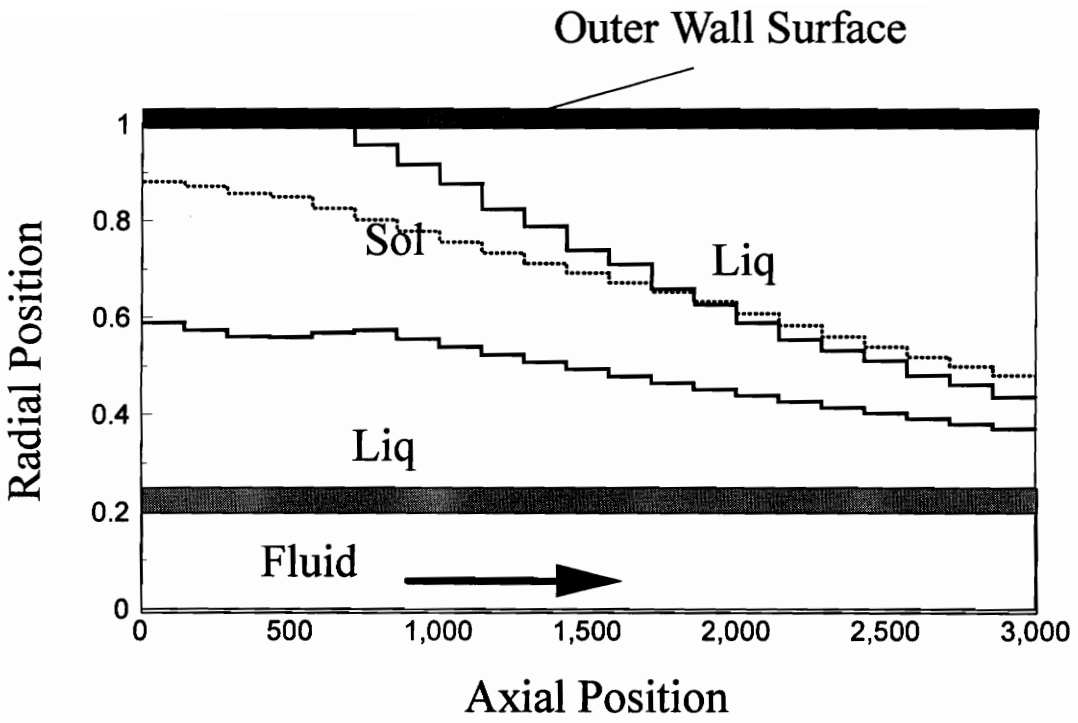

Fig. 3.12: Moving front distribution in the middle of the second melting period ($\tau = 3.5$, nn = 70); parameters are listed in Table 3.3

freeze front to move out for axial segments 6 to 13. This subcooling stores more sensible energy in the solid at the entrance segments and slowed down the second melt front more than in the first melting period. The second solid front near the exit propagated not as far as in previous cooling period because of the stored sensible energy from the previous heating period.

Figure 3.13 shows the results at $\tau = 4.5$, in the middle of the third freezing period. The second melt front overtook the second freeze front around the exit at axial segments 14 to 21. Because of more subcooling in last cooling period, the melt front at the entrance segment 1 to 13 of last period did not propagated as far as in previous heating period.

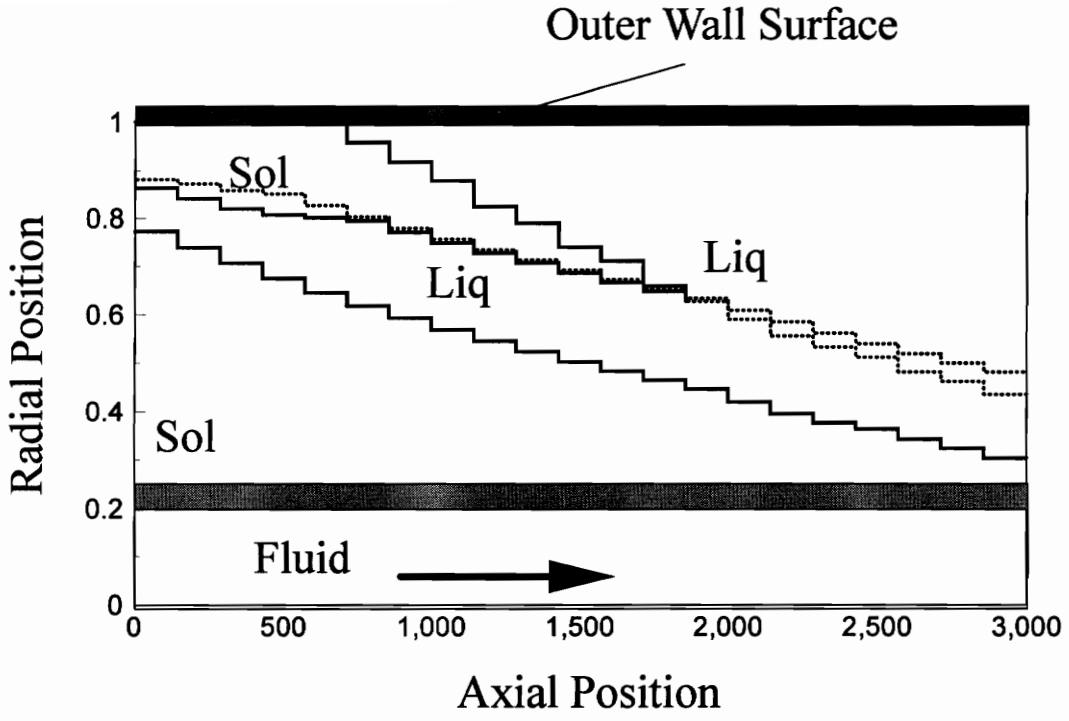

Fig. 3.13: Moving front distribution in the middle of the third freezing period ($\tau = 4.5$, nn = 90); parameters are listed in Table 3.3

CHAPTER 4 THERMAL NETWORK METHOD (TNM)

4.1 MODEL OF THERMAL STORAGE COMPONENT

A typical thermal storage tank consists of an array of pipes surrounded by phase change material (PCM) with brine flowing through the pipes in a counter or parallel flow arrangement. Water is used as the PCM due to a combination of high latent heat, cost and safety. The thermal storage unit, along with a chiller and load are represented in Fig. 1.1.

A counter flow arrangement with a typical tube pair is shown in Fig. 1.3. The particular tube pair and the amount of phase change material shared by the tube pair depend on the geometric arrangement of the tubes and the resulting planes of symmetry. Since charging and discharging is accomplished with the brine flowing on the inside of the tubes, alternating layers of liquid and solid could be present. Axial locations near the inlet would tend to charge and discharge at a higher rate than locations further downstream, thus the thicknesses of the ice and liquid layers around adjacent tubes would be different. As a result, the two tubes need to be considered together with alternating layers of liquid and ice forming around each tube and the remaining mass of PCM shared between them. The complete thermal model of the thermal storage unit is built up from an appropriate number of tube pairs.

An axial view of a typical tube pair showing the alternating layers of ice and liquid and the remaining shared mass of either ice or liquid between the tubes is shown in Fig. 4.1. The following assumptions are employed in the thermal model:

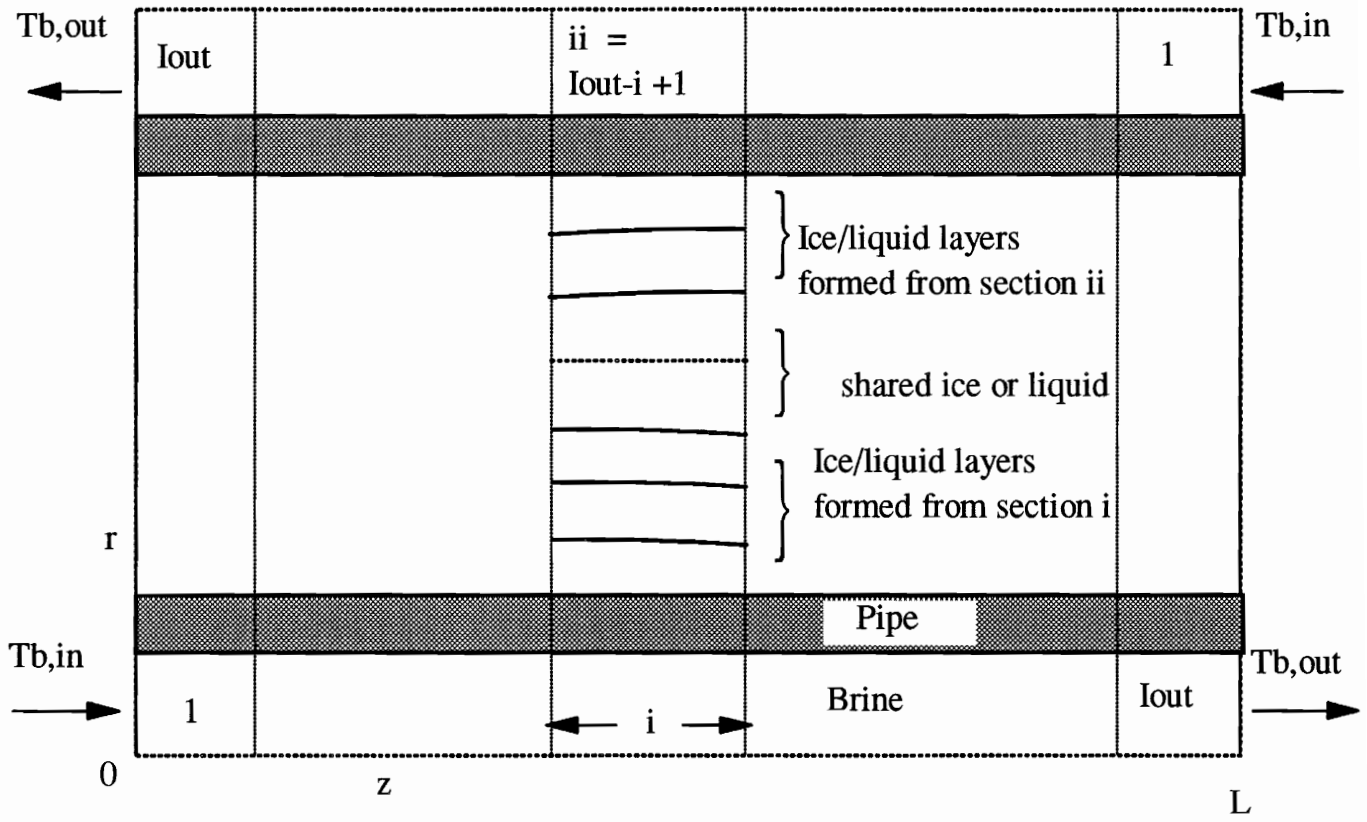

Fig. 4.1: Typical Tube Pair in a Counterflow Arrangement

1. Axial heat conduction is neglected. An axial section of total length L may then be divided into I_{out} axial segments of length Δz over which all quantities are uniform.
2. One-dimensional, radial heat transfer is assumed in the alternating liquid and ice layers forming in each axial segment.
3. Sensible heat effects in the pipe walls and in the ice/liquid layers are lumped on the outside boundary of each layer.
4. The sensible heat contained in the mass of shared ice or liquid between adjacent tubes is lumped as a thermal capacitance and placed at the center of the available mass, located at $r = r_{out}(t)$. This forms the thermal link between adjacent tubes and allows the tubes to share the available PCM while maintaining the one-dimensional radial approximation for the layers.
5. Changes in sensible energy are calculated using a quasi-steady state temperature profile between the two boundary temperatures of each layer. For the one-dimensional, radial case considered here the profiles are logarithmic, as explained in Appendix A.
6. A constant density equal to the average liquid and solid densities is used.
7. External heat gains are distributed into each axial section and are input on the outermost phase boundary or at the outside pipe wall if no phase change is occurring. The external heat gain is calculated using an overall heat transfer coefficient in the form,

$$q_{amb} = (UA)_{amb}(T_{amb} - T_{fr})/(N \cdot I_{out}) \qquad (4.1)$$

where N is the number of tubes and T_{amb} is the external ambient temperature.

In view of the preceding assumptions, the dynamic behavior of the ice building and melting processes can be analyzed as a sequence of radially one-dimensional problems in each of the axial segments shown in Fig. 4.1. An axial segment communicates with downstream segments through the brine flowing in the tubes and communicates with the adjacent tube in the counterflow arrangement through the shared PCM between the tube pair. Since the latent heat is a concentrated effect at ice/liquid interfaces and since the distributed effects of sensible heat are assumed to be lumped at the outer boundary of each layer, the thermal model for a typical axial section can be represented with a network of resistors and capacitors. The energy terms involved in a typical axial section i for the situations involving no phase change, a single phase boundary, and multiple phase boundaries are pictured in Figs. 4.2, 4.3 and 4.4, respectively. The resistors and sensible energy terms are summarized in Table 4.1. The number of ice/liquid phase interfaces is designated as J and the locations are designated by s_1, s_2,...,s_J. For convenience the subscript i has been omitted from all symbols, thus, $T_b = T_{b,i}$ represents the brine temperature over section i, $s_1 = s_{1,i}$ represents the location of the innermost phase boundary and so forth. Explicit reference to axial sections other than i (such as i-1 or ii) have been retained. The energy equations governing the thermal storage unit are now derived with reference to Table 4.1 and Figs. 4.2, 4.3, and 4.4.

Table 4.1: RESISTOR AND SENSIBLE ENERGY TERMS USED IN THE THERMAL MODEL

Region	R (°C/W or °F·h/Btu)	E_{sen} [1] (kJ or Btu)
Brine (b)	$\frac{1}{(2\pi r_{pi}\Delta x)\bar{h}}$	$(\pi r_{pi}^2 \bullet \Delta x)(\rho C_p)_b T_b$
Pipe (p)	$\frac{\ln\left(\frac{r_{po}}{r_{pi}}\right)}{2\pi k_p \Delta x}$	$C_{o,p} T_{po} + C_{i,p} T_{pi}$
Inner Layer (1)	$\frac{\ln\left(\frac{s_I(t)}{r_{po}}\right)}{2\pi k_1 \Delta x}$	$C_{o,1} T_{fr} + C_{i,1} T_{po}$
Outer Layer (out)	$\frac{\ln\left(\frac{r_{out}(t)}{s_I(t)}\right)}{2\pi k_{out} \Delta x}$	[2] $(C_{o,out} T_{out} + C_{i,out} T_I) + (C_{o,out} T_{out} + C_{i,out} T_I)_{ij}$

1 See Appendix A for derivations and definitions of C_o and C_i.

2 $$T_I = \begin{cases} T_{po} & , \text{ no phase change} \\ T_{fr} & , \text{ with phase change} \end{cases}$$

4.1.1 Energy Balance in the Brine in Axial Section-i

Conservation of energy in the brine requires,

$$\frac{dE_{sen,b}}{dt} = \dot{m}(h_{i-1} - h) - q'_b \qquad (4.2)$$

where q'_b is the average heat transfer from the brine to the pipe wall and his enthalpy in section i. Since T_b represents the bulk fluid temperature of the brine, the sensible energy term listed in Table 4.1 can be represented by the single temperature T_b. The enthalpy change of the flowing brine can be expressed as,

$$\dot{m}(h_{i-1} - h) = (\dot{m} C_p)_b [T_{b,i-1} - T_b] \qquad (4.3)$$

Note that an upwind scheme in the axial variable has been used; that is, the incoming flow term is evaluated using T_b in the upstream section i-1 while the outgoing flow term is evaluated using values from section i. The heat transfer between the inside pipe surface and the brine is evaluated as,

$$q_b = \frac{T_b - T_{pi}}{R_b} = (2\pi r_{pi} \Delta x)\ \bar{h}(T_b - T_{pi}) \qquad (4.4)$$

The average heat transfer coefficient, , in section i is evaluated from appropriate Nusselt number correlations in a round duct as summarized in Appendix B.

Substituting relations (4.3) and (4.4) and $E_{sen,b,j}$ from Table 4.1 into (4.2) gives the brine energy equation in terms of temperatures as,

$$(\pi r_{pi}^2\ \Delta x)(\rho C_p)_b\ \frac{dT_b}{dt} = (\dot{m} C_p)_b\ (T_{b,i-1} - T_b) - \frac{T_b - T_{pi}}{R_b} \qquad (4.5)$$

4.1.2 Energy Balance at Inside Pipe Wall in Axial Section i

At location $r = r_{pi}$, an energy balance gives,

$$q_b = q_p$$

which can be written in terms of temperature as,

$$\frac{T_b - T_{pi}}{R_b} = \frac{T_{pi} - T_{po}}{R_p} \qquad (4.6)$$

4.1.3 Energy Balance at Outside Pipe Wall in Axial Section i

At $r = r_{po}$, the energy balance with and without phase change takes different forms. As seen in Fig. 4.2 with no phase change, the outside pipe wall at T_{po} communicates directly with the shared capacitor at temperature T_{out} through the resistor R_{out}. However, Figs. 4.3 and 4.4 show that when phase change is occurring, the outside pipe wall communicates directly with the innermost phase boundary at temperature T_{fr} through the resistor R_1. The appropriate energy balances become,

$$\frac{dE_{sen,p}}{dt} = \begin{cases} q_p - q_{out} + q_{amb} \\ q_p - q_1 \end{cases} \qquad (4.7)$$

Equation (4.7) can be then expressed in terms of temperature as,

$$\frac{dE_{sen,p}}{dt} = \begin{cases} \dfrac{T_{pi} - T_{po}}{R_p} - \dfrac{T_{po} - T_{out}}{R_{out}} + q_{amb} \text{ , no phase change} \\ \dfrac{T_{pi} - T_{po}}{R_p} - \dfrac{T_{po} - T_{fr}}{R_1} \text{ , with phase change} \end{cases} \qquad (4.8)$$

where the sensible energy term and resistors are listed in Table 4.1

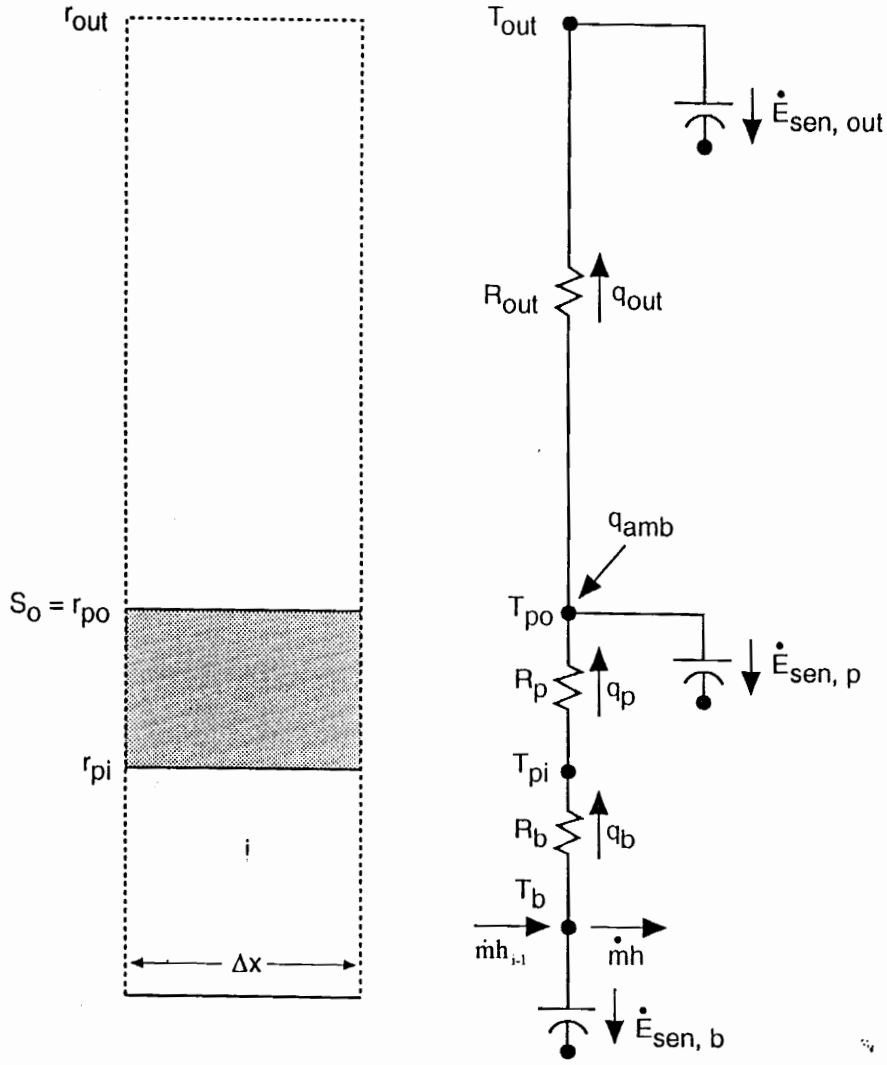

Fig. 4.2: Energy Terms in Axial Section-j with no phase change (I = 0)

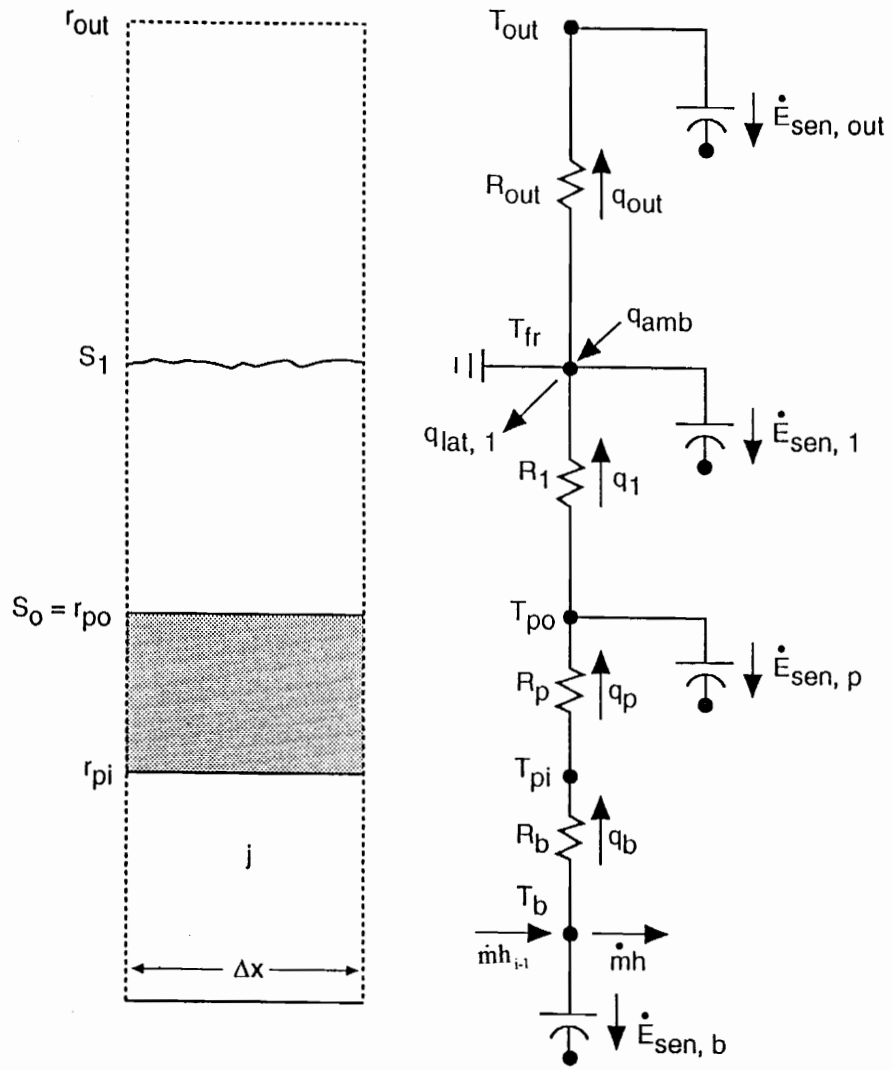

Fig. 4.3: Energy Terms in Axial Section-j with a single phase front (I = 1)

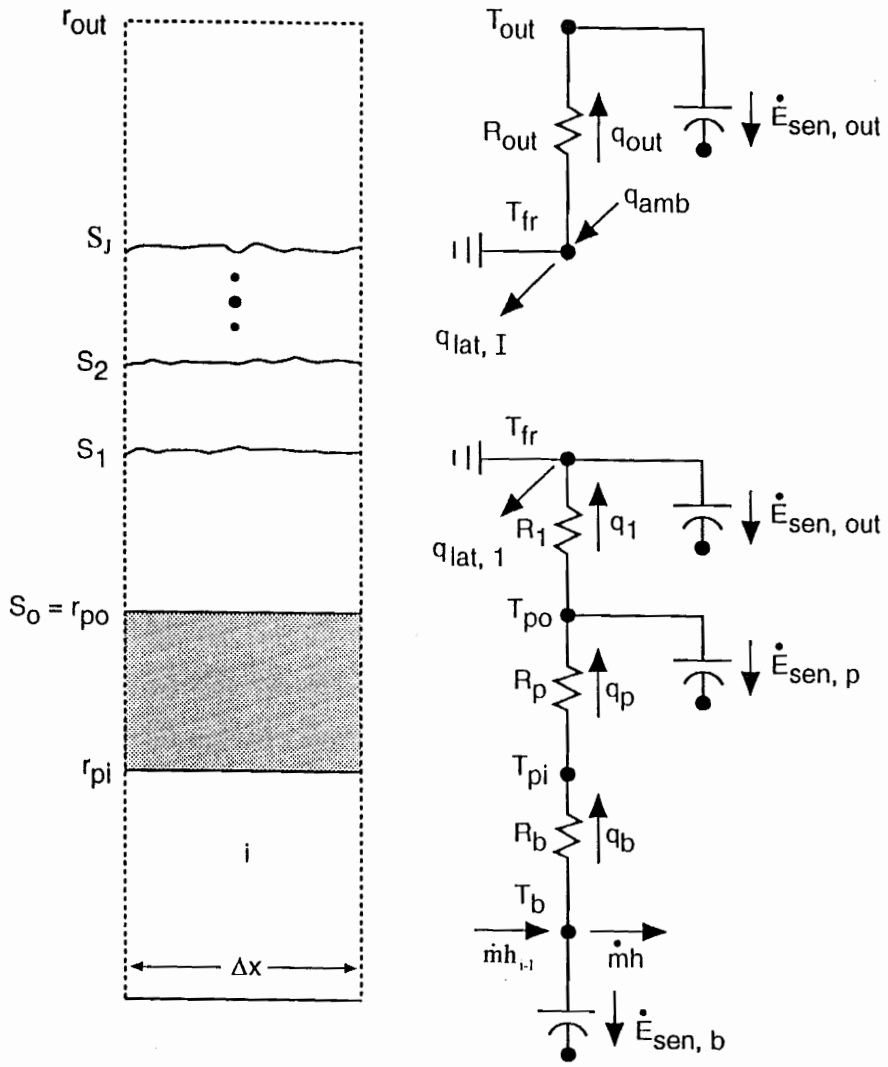

Fig. 4.4: Energy Terms in Axial Section-j with multiple phase fronts ($I \geq 2$)

When a phase change is occurring, s_1 and thus resistor R_1 change with time. The conductivities k_1 and k_{out} needed in R_1 and R_{out}, respectively become the conductivity of ice or liquid.

4.1.4 Energy Balance at Inner Phase Boundary in Axial Section i

The energy balance at $r = s_1(t)$ depends on whether single or multiple fronts exist. As seen in Fig. 4.3 for a single phase front (J= 1), the temperature T_{fr} is linked directly with T_{out} through resistor R_{out}. However, the presence of multiple phase boundaries ($J \geq 2$), together with the quasi-steady temperature profiles assumption, thermally insulates adjoining phase boundaries from each other as seen in Fig. 4.4. The appropriate energy equations are thus,

$$\frac{dE_{sen,1}}{dt} + q_{lat} = \begin{cases} q_1 - q_{out} + q_{amb}, & \text{single phase front} \\ q_1, & \text{multiple phase front} \end{cases} \qquad (4.9)$$

The latent energy contribution is

$$q_{lat} = \pm \rho h_{if} \frac{ds_1}{dt}(2\pi s_1 \Delta x) \qquad (4.10)$$

where h_{if} is the latent heat. During melting latent energy is absorbed by the ice while during freezing latent energy is released by the liquid thus, the plus sign is appropriate when the first layer adjacent to the pipe is liquid while the minus sign is appropriate when the first layer is solid. Substituting eqn.(4.10) into eqn.(4.9) and expressing heat rates in terms of temperatures and resistors produces,

$$\frac{dE_{sen,1}}{dt} \pm \rho h_{if} \frac{ds_1}{dt}(2\pi s_1 \Delta x) = \begin{cases} \dfrac{T_{po} - T_{fr}}{R_1} - \dfrac{T_{fr} - T_{out}}{R_{out}} + q_{amb} \text{ , single phase front} & (4.11a) \\ \dfrac{T_{po} - T_{fr}}{R_1} \quad \text{, multiple phase front} & (4.11b) \end{cases}$$

where the R values and $E_{sen,1}$ are listed in Table 4.1.

4.1.5 Energy Balance at Outer Phase Boundary in Axial Section i

When more than one phase front exists, the interior interfaces ($s_2,...,s_{J-1}$) are insulated and thus locked in place since no heat transfer is available for phase change. However, the outside phase interface can communicate with the shared PCM between the tube pair. As shown in Fig. 4.4, the energy balance at $r = s_j(t)$ is,

$$q_{lat,j} = -q_{out} + q_{amb}$$

which can be expressed as,

$$\pm \rho h_{if} \frac{ds_j}{dt} (2\pi s_j \Delta x) = - \frac{T_{fr} - T_{out}}{R_{out}} + q_{amb} \qquad (4.12)$$

where the plus sign applies when layer j is liquid, the minus sign applies when layer j is solid.

4.1.6 Energy Balance at $r = r_{out}(t)$ in Axial Section i

The location $r_{out}(t)$ at any instant of time is at the center of the shared PCM between the two tubes forming a tube pair in the counterflow arrangement. With no phase change from either tube, r_{out} is exactly halfway between the adjoining tubes. The energy balance at r_{out} is,

$$\frac{dE_{sen,out}}{dt} = q_{out} \qquad (4.13)$$

The sensible energy in the shared layer is due to both section i and the adjoining section $ii = I_{out} - i + 1$ and thus is calculated in two distinct pieces as indicated in Table 4.1. Equation (4.13) can be expressed as,

$$\frac{dE_{sen,out}}{dt} = \frac{T_J - T_{out}}{R_{out}} \qquad (4.14)$$

where T_J is the temperature at s_J,

$$T_J = \begin{cases} T_{po} \text{ , no phase change} \\ \\ T_{fr} \text{ , with phase change} \end{cases}$$

All terms without an axial subscript refer to section i.

4.2 NUMERICAL INTEGRATION

The energy equations derived in the previous section represent a coupled set of first order equations in time for the unknown temperatures and phase boundary locations. The solution is obtained by marching in the time variable from some known initial state and integrating the equations directly in an implicit fashion. As described by Patankar (1980), the implicit scheme produces unconditionally stable results for any size time step while explicit and centered difference schemes can produce unstable oscillations in the solutions if the time step is too large.

Energy equations (4.5), (4.6), (4.8), (4.11), (4.13), and (4.14) are integrated in time from t_{n-1} to $t_n = t_{n-1} + \Delta t$ to obtain the following set of relations:

Brine

$$(\pi r_{pi}^2 \Delta x)(\rho C_p)_b (T_b^n - T_b^{n-1}) = \Delta t(\dot{m} C_p)_b (T_{b,i-1}^n - T_b^n) - \frac{\Delta t}{R_b}(T_b^n - T_{pi}^n) \quad (4.15)$$

Inside Pipe Wall

$$\frac{\Delta t}{R_b}(T_b^n - T_{pi}^n) = \frac{\Delta t}{R_p}(T_{pi}^n - T_{po}^n) \quad (4.16)$$

Outside Pipe Wall

$$E_{sen,p}^n - E_{sen,p}^{n-1} = \begin{cases} \frac{\Delta t}{R_p}(T_{pi}^n - T_{po}^n) - \frac{\Delta t}{R_{out}}(T_{po}^n - T_{out}^n) + q_{amb}.\Delta t \text{, no phase change} & (4.17a) \\ \frac{\Delta t}{R_p}(T_{pi}^n - T_{po}^n) - \frac{\Delta t}{R_1}(T_{po}^n - T_{fr}^n) \text{, with phase change} & (4.17b) \end{cases}$$

Inner Phase Boundary

$$E_{sen,1}^n - E_{sen,1}^{n-1} \pm \rho h_{if}[(s_1^n)^2 - (s_1^{n-1})^2]\Delta z =$$

$$\begin{cases} \frac{\Delta t}{R_1^n}(T_{po}^n - T_{fr}) - \frac{\Delta t}{R_{out}^n}(T_{fr} - T_{out}^n) + q_{amb}.\Delta t \text{, single phase front} & (4.18a) \\ \frac{\Delta t}{R_1^n}(T_{po}^n - T_{fr}^n) \text{, multiple phase front} & (4.18b) \end{cases}$$

Outer Phase Boundary

$$\pm \rho h_{if} \pi \left[(s_j^n)^2 - (s_j^{n-1})^2\right]\Delta x = -\frac{\Delta t}{R_{out}^n}(T_{fr} - T_{out}^n) + q_{amb}\ \Delta t \quad (4.19)$$

Shared Capacitor at r_{out}

$$E^{n}_{sen,out} - E^{n\text{-}1}_{sen,out} = \frac{\Delta t}{R^{n}_{out}} (T^{n}_{j} - T^{n}_{out}) \qquad (4.20)$$

where

$$T^{n}_{j} = \begin{cases} T^{n}_{po} \text{ , no phase change} \\ T_{fr} \text{ , with phase change} \end{cases}$$

In the previous expressions, the superscript n indicates values at time t_n. Note that resistor values which depend on the moving phase locations are functions of time and are also designated with the superscript n. In addition, some of the heat capacity coefficients, C_o and C_i, used in the E_{sen} terms depend on the phase locations and are also functions of time.

4.3 COMPUTATIONAL ALGORITHM

Equations (4.15)-(4.20) provide a simultaneous set of nonlinear equations for the unknown temperatures and phase fronts at time t_n in terms of values at the previous time step t_{n-1}. Equation (4.15) also involves the brine temperature in the upstream axial segment i-1. The solution is implemented by marching forward in time and downstream in the axial variable. Thus values at time t_{n-1} and in axial segment i-1 have already been calculated or have been specified as inlet or initial conditions and only values at the current time t_n in section j are unknown.

The particular combination of unknowns, equations and required solution procedure depend on the configuration of ice and liquid layers that exist at the current time and axial location. The three possible configurations are as follows:

No Phase Change (J=0)

Unknowns: T_b^n , T_{pi}^n , T_{po}^n , T_{out}^n

Equations: (4.15), (4.16), (4.17a), (4.20)

Solution: The system of equations is linear and can be solved directly.

Single Phase Boundary (J=1)

Unknowns: T_b^n , T_{pi}^n , T_{po}^n , s_1^n , T_{out}^n

Equations: (4.15), (4.16), (4.17b), (4.18a), (4.20)

Solution: This system is linear in the temperature variables but highly nonlinear with respect to s_1^n. Thus the value of s_1^1 is guessed based on the velocity of s_1 at the previous time step and equations (4.15), (4.16), (4.17b) and (4.20) are solved for the temperatures. Equation 4.18a is then used to obtain an improved value of s_1^n and the iteration continues until satisfactory convergence is achieved.

Multiple Phase Boundaries (J ≥ 2)

Unknowns: T_b^n , T_{pi}^n , T_{po}^n , s_1^n , s_J^n , T_{out}^n

Equations: (4.15), (4.16), (4.17b), (4.18b), (4.19), (4.20)

Solution: Equations (4.15), (4.16), (4.17b) and (4.18b) are uncoupled from equations (4.19) and (4.20) and are solved in manner described for a single phase front. Equations (4.19) and (4.20) are solved by guessing s_J^n and solving equation (4.20) for T_{out}^n. This value of T_{out}^n

is used in equation (4.19) to obtain an improved value for s_1^n and the iteration proceeds until convergence is met. Note that the internal phase fronts, s_2, s_3,...,s_{J-1} are thermally insulated and thus locked in place.

At each new time and axial location, the unknown temperatures and phase fronts are calculated assuming that the previous configuration of phase fronts still exists. The results from the new calculation are then examined to see if a configuration change has occurred. If no configuration change occurs, the solution proceeds down the tube. If a configuration change has occurred, the necessary energy corrections are made and the solution is recalculated. Configuration changes are due to the following occurrences:

1. T_{po} crosses the freezing temperature T_{fr}.

   In this case, a new phase front begins propagating from the pipe wall. The sensible energy required to bring the pipe wall to T_{fr} is added to the inner phase front, J is set to J+1 and the solution is recalculated.

2. s_1 overtakes s_2 or s_j becomes less than s_{j-1}

   In this case, two layers and two phase fronts are destroyed. The sensible and latent energy corrections are made and the solution is recalculated with J = J - 2.

3. s_1 becomes less than $s_o = r_{po}$

   This can only occur for a single phase boundary (J=1) due to heat transfer from the shared capacitance and external environment. The sensible and latent energy corrections are made and the solution is recalculated with J = J-1 = 0.

4. s_1 overtakes r_{out}

This can only occur for a single phase boundary (J=1). The mass shared by the tube pair has been consumed and a new shared mass is assigned.

The various configuration changes which can occur require a significant amount of logic and testing in the computer code, however, accounting for these changes is essential for an accurate description of the dynamic behavior of the thermal storage unit. Whenever a configuration change occurs, energy corrections are made to conserve total energy, both sensible and latent. A flow chart of the basic algorithm is shown in Fig. 4.5.

4.4 SAMPLE CALCULATIONS

The algorithm for the ice thermal storage component is now applied to a special case involving partial discharge and partial charge cycles in order to show the dynamics of the ice melting and building processes. A counter flow arrangement is considered with a brine flow rate of 0.05kg/s (.79GPM) in each tube, a total length in the axial direction of 76.2m (250ft), an inside tube radius of 6.4mm (1/4in), an outside tube radius of 7.9mm (5/16in), and a mass of 218kg (58gal) of water shared by the tube pair. These parameters match a CALMAC model 1190 which has 56 tubes or 28 tube pairs for a total mass of 6131kg (1620 gal) of water and a total brine flow rate of 2.8kg/s (44GPM).

Initially the water is in a fully charged state as ice at 0°C. A discharge cycle is then initiated by introducing brine at 7°C (45°F) into the tubes. Calculations were performed using 20 axial sections (Δz=3.81m) along the flow direction and using a time step of 1/2 hour. The positions

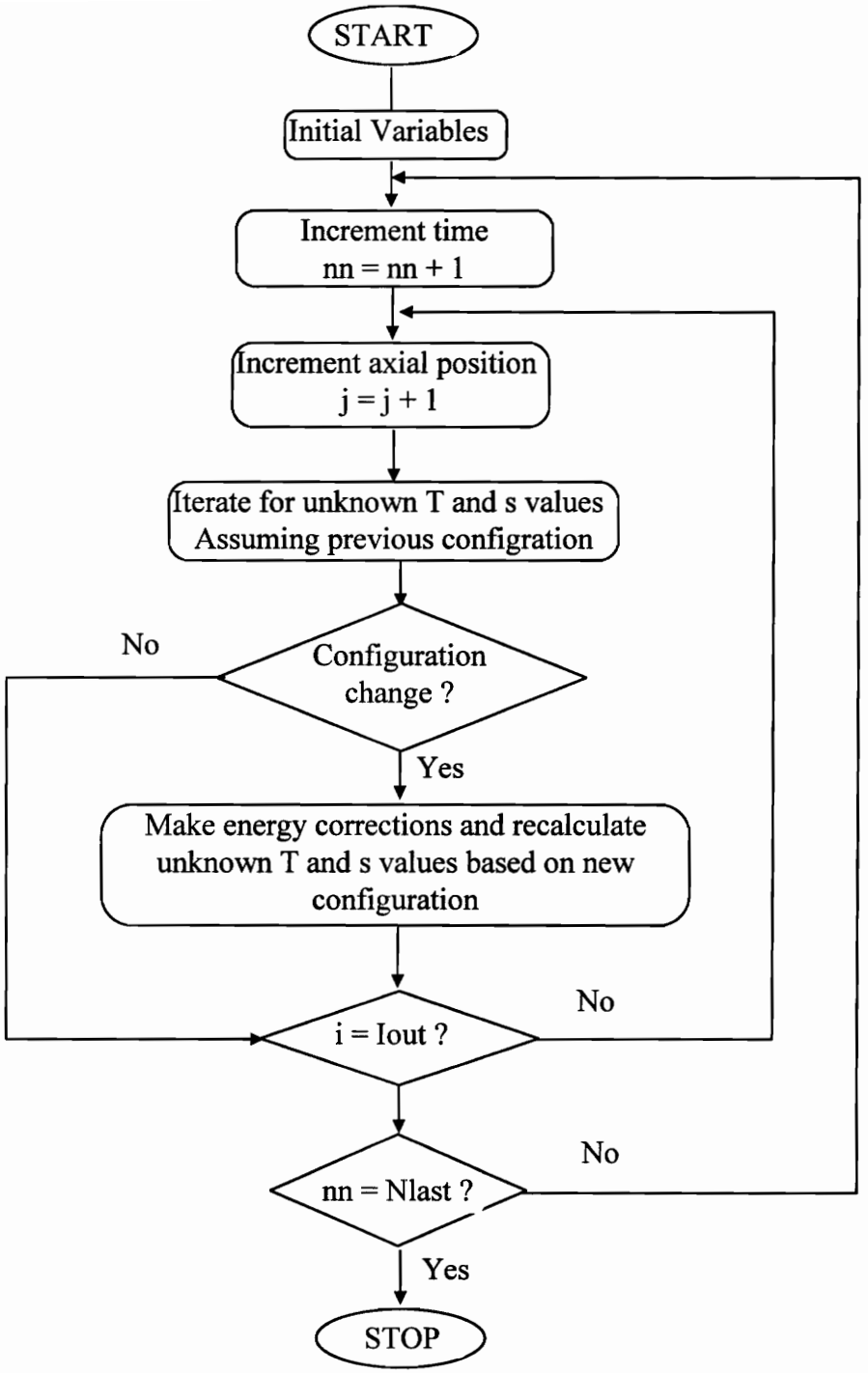

Fig. 4.5 Basic algorithm for the thermal storage component

of the phase fronts after 12 hours of discharge are pictured in Fig. 4.6a. The thermal storage component has only been partially discharged at this time as a sliver of ice still remains between the tubes. The phase fronts appear as stairsteps due to the numerical discretization process. Additional refinement could be obtained by using more axial segments and using a finer time step, however, numerical experiments show that additional numerical refinements do not improve the exit brine temperature of $T_{b,out}$ = 3.3°C = 38°F or the latent state of charge to two significant figures for this combination of parameters.

Following 12 hours of discharge, a changing cycle is initiated by supplying brine at an inlet temperature of -5°C (23°F). The phase fronts after 8 hours of charging are displayed in Fig. 4.6b. The system has been partially charged at this time as the sliver of ice remaining from the partial charge cycle is now surrounded by a layer of liquid and another ice layer adjacent to the tubes. The exit brine temperature at this instant of time is -1.3°C (30°F).

The results in Figures 4.6a and 4.6b display the multiple ice/water layer possibility, which make the ice-on-pipe brine thermal storage systems unique.

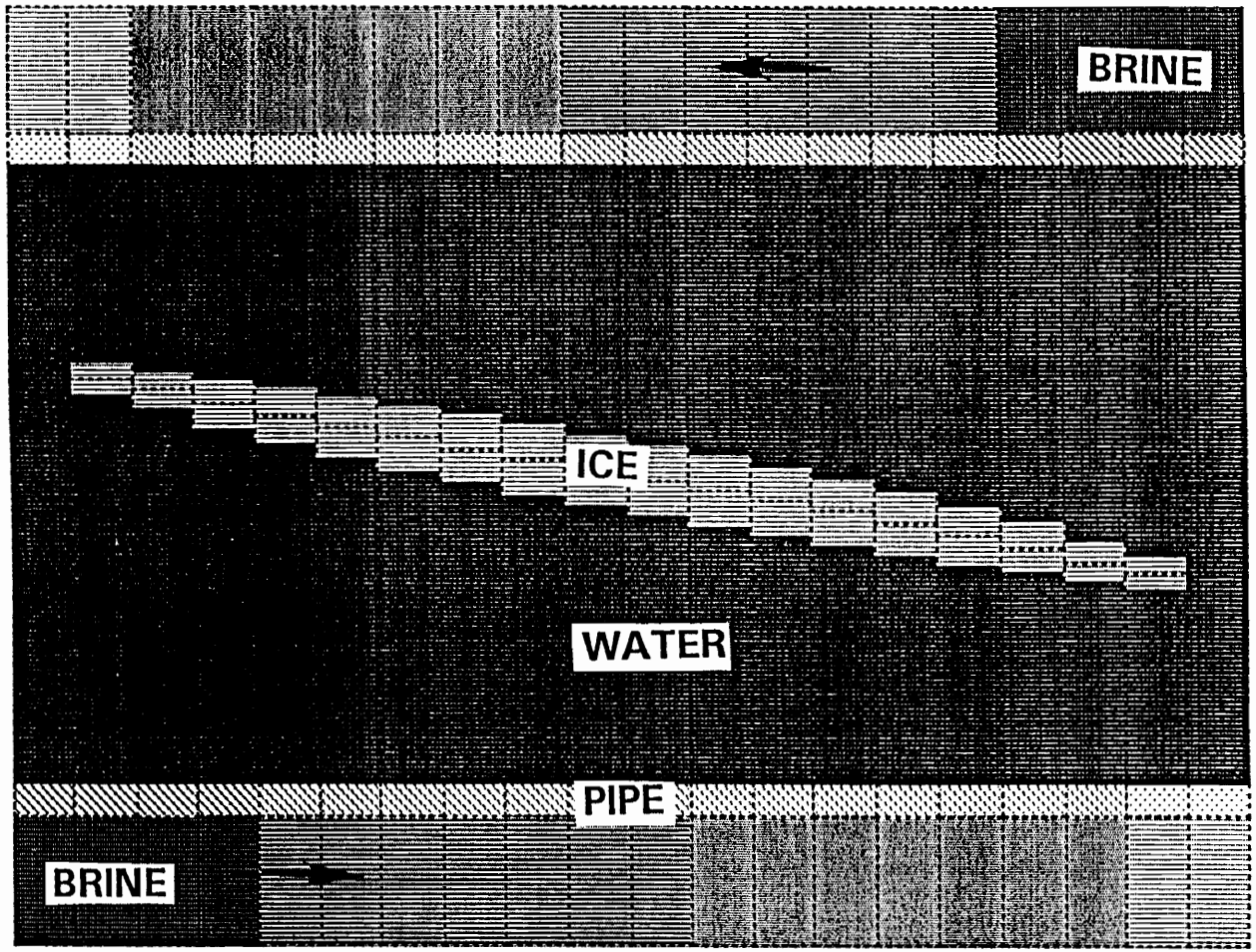

Fig. 4.6a: Phase fronts after 12 hours of discharge starting from fully charged ice at 0°C using brine at an inlet temperature of 7°C

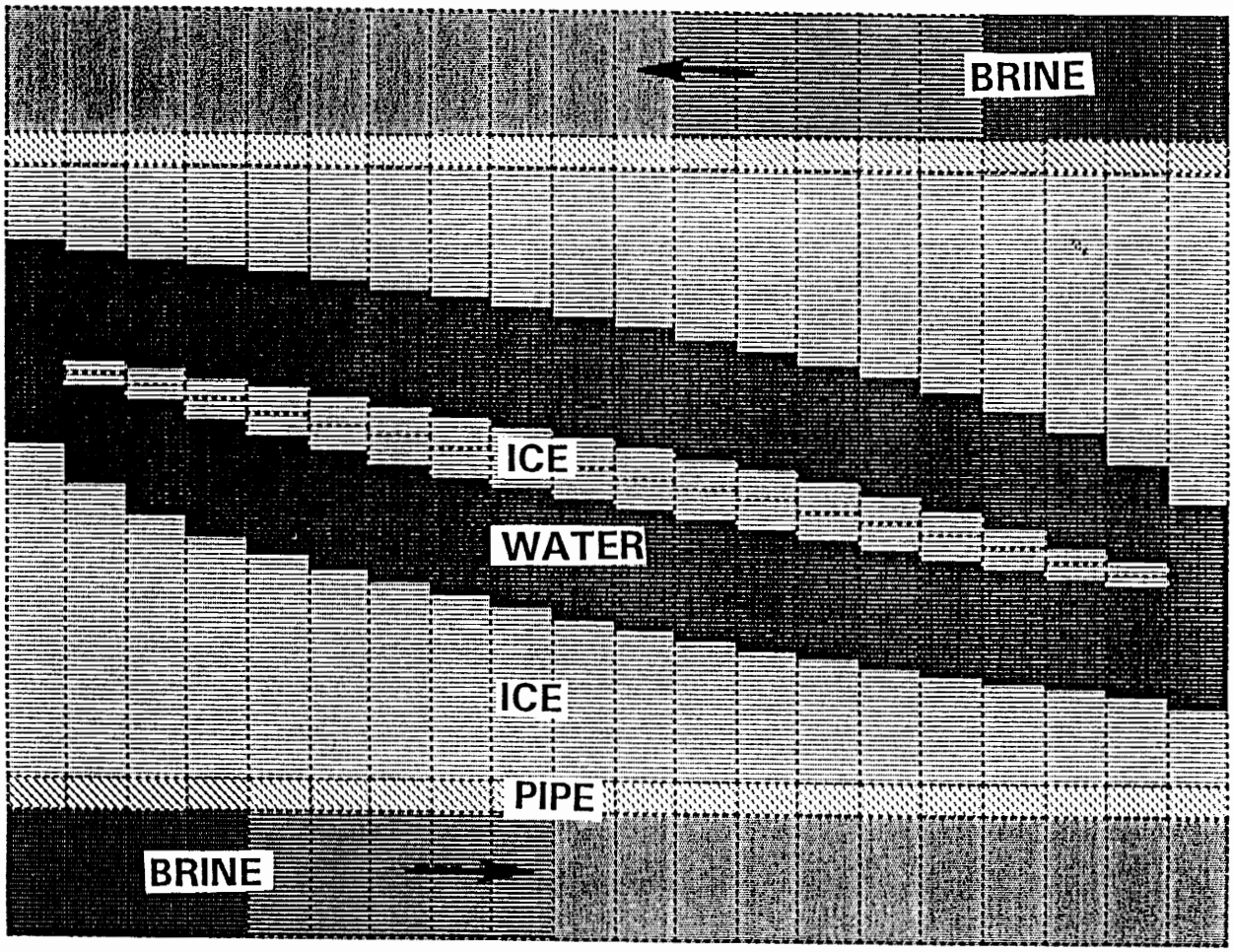

Fig. 4.6b: Phase fronts after 8 hours of charge using brine at an inlet temperature of -5°C following the 12 hour discharge cycle of Fig. 8a.

CHAPTER 5 VALIDATION OF THE ALGORITHMS

5.1 MODEL USED FOR THE IceTES COMPONENT

The computer program which predicts the transient performance of the ice-on-pipe brine system using the TNM is called IceTES (Ice Thermal Energy Storage). The theoretical model and solution method used to develop IceTES are described in detail in Chapter 4.

In the computer program IceTES, the mass flow rate of brine to each tube is obtained by dividing the total flow rate by the number of storage tanks in a system and by the number of tubes per storage tank. The amount of water surrounding each tube is similarly obtained by dividing the total mass of water in a tank by the number of tubes per tank. Calculations are then performed for a particular tube pair. The IceTES component requires the inlet brine temperature and mass flow rate at each time step and then calculates the dynamic response of the thermal storage component, including important quantities such as the exit brine temperature, charge or discharge rate, and state of charge of the system.

5.2 PARAMETRIC STUDIES

In order to examine qualitatively the dynamic behavior of the IceTES algorithm, a set of parameter studies for both charging and discharging cases were run. Figures 5.1, 5.2 and 5.3 show results for charge cycles and Figs. 5.4 and 5.5 display results for discharge

cycles. The particular parameters used in these figures correspond to the conditions for a Calmac model 1190, although the trends are typical of those found using any set of parameters.

Figure 5.1 shows outlet brine temperature, charging rate, and state of charge as a function of time for a fixed mass flow rate and various inlet brine temperatures. Lower inlet temperatures cause lower outlet temperatures and increase the temperature differences, thus producing greater charge rates. The relationship between temperature difference and charge rate can be seen from the following energy balance on the brine,

$$\dot{Q} = (\dot{m} C_p)_b \Delta T \qquad (5.1)$$

where

$\dot{Q}$ = charge or discharge rate

$\dot{m}$ = mass flow rate of brine

C_p = specific heat of brine

$$\Delta T = \begin{cases} T_{b,out} - T_{b,in} & , \text{ charge} \\ T_{b,in} - T_{b,out} & , \text{ discharge} \end{cases}$$

$T_{b,in}$ = inlet brine temperature

$T_{b,out}$ = outlet brine temperature

During most of the charge cycle, the exit temperature drops gradually, starting from values slightly below the freezing temperature of 32°F. However, as a state of full charge is approached, the exit temperature drops rapidly towards the inlet temperature since the entire mass of water becomes frozen and no more latent capacity is available to soak up heat. The

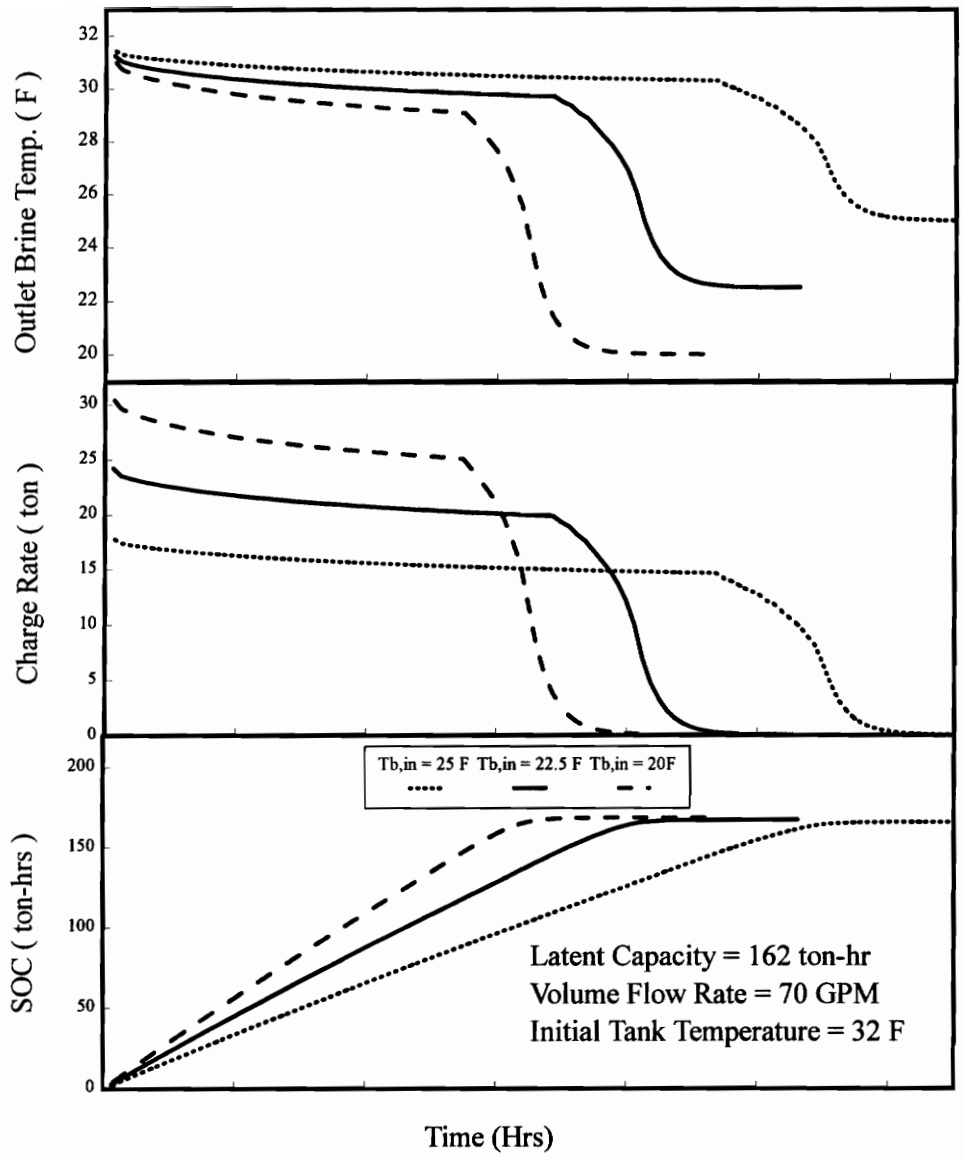

Fig. 5.1: Effects of brine inlet temperature on performance during a charge cycle.

charge rate behaves in a similar manner with relatively high values maintained until the latent capacity becomes saturated, causing the charge rate to drop rapidly to zero. Low inlet temperatures and high charge rates can significantly reduce the time required to charge the system. The state of charge shown in Fig. 5.1 is due to both latent and sensible energy in the ice tank. Although the latent capacity of the ice tank is 162 ton-hr, the total state of charge reaches somewhat greater values at full charge due to the sensible energy of subcooling the ice.

The brine outlet temperature and charge rate shown in Fig. 5.1 are replotted in Fig. 5.2 as a function of the fraction of latent capacity. The rapid drop in both outlet temperature and charge rate is seen to occur as the system becomes fully charged.

Figure 5.3 shows the effect of mass flow rate with a fixed inlet temperature on the charging performance. An increase in mass flow rate produce exit temperatures closer to the inlet temperature and an increase in charge rate. The drop in outlet temperature and charge rate is more gradual and begins with a higher fraction of latent capacity remaining as the flow rate is decreased.

The dynamic behavior during discharge is examined in Figs. 5.4 and 5.5. Figure 5.4 shows results for various inlet temperatures at a fixed mass flow rate. Increased inlet temperatures produce increased exit temperatures and also produces higher temperature differences, resulting in higher discharge rates as seen from eqn. (5.1). The outlet temperature rises gradually and the discharge rate drops gradually until almost all of the latent capacity is depleted, at which time the outlet temperature rises rapidly to the value of

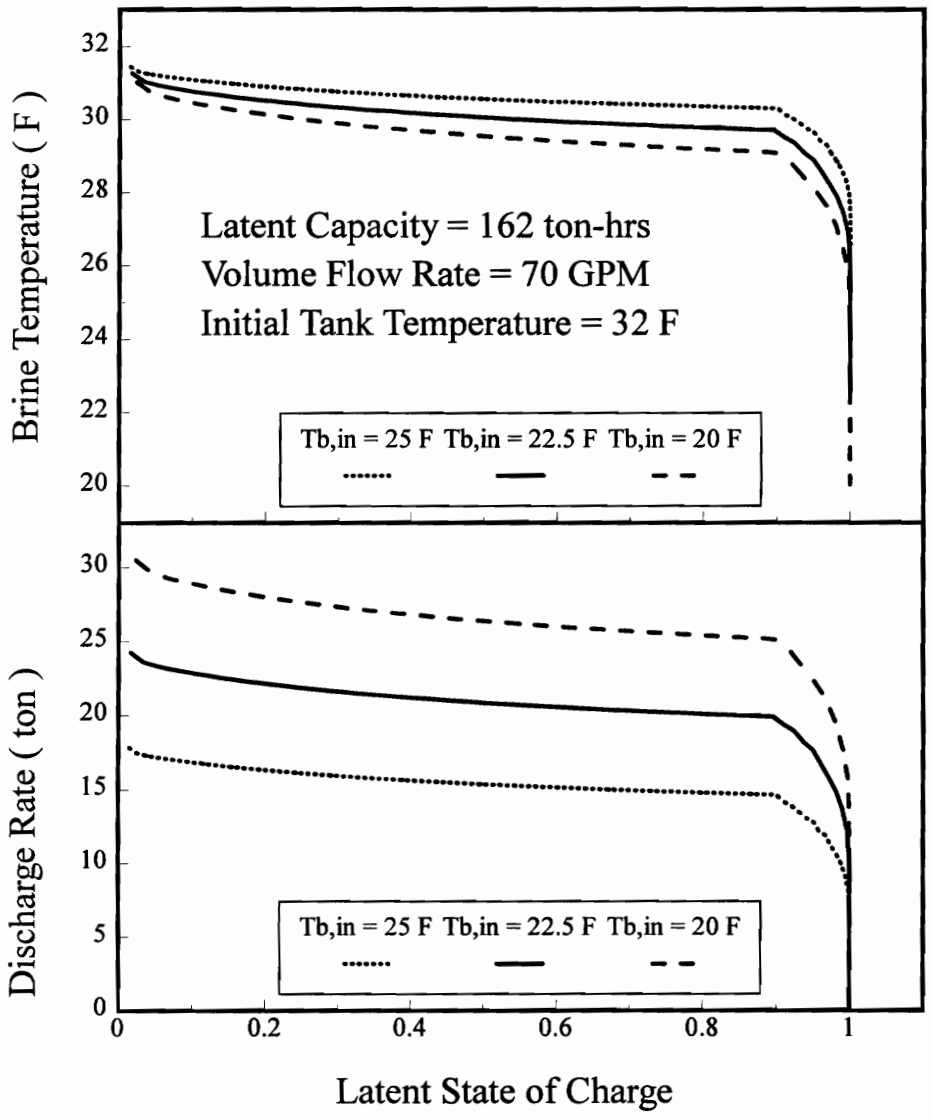

Fig. 5.2: Effects of brine inlet temperature during a charge cycle shown as a function of fraction of latent capacity.

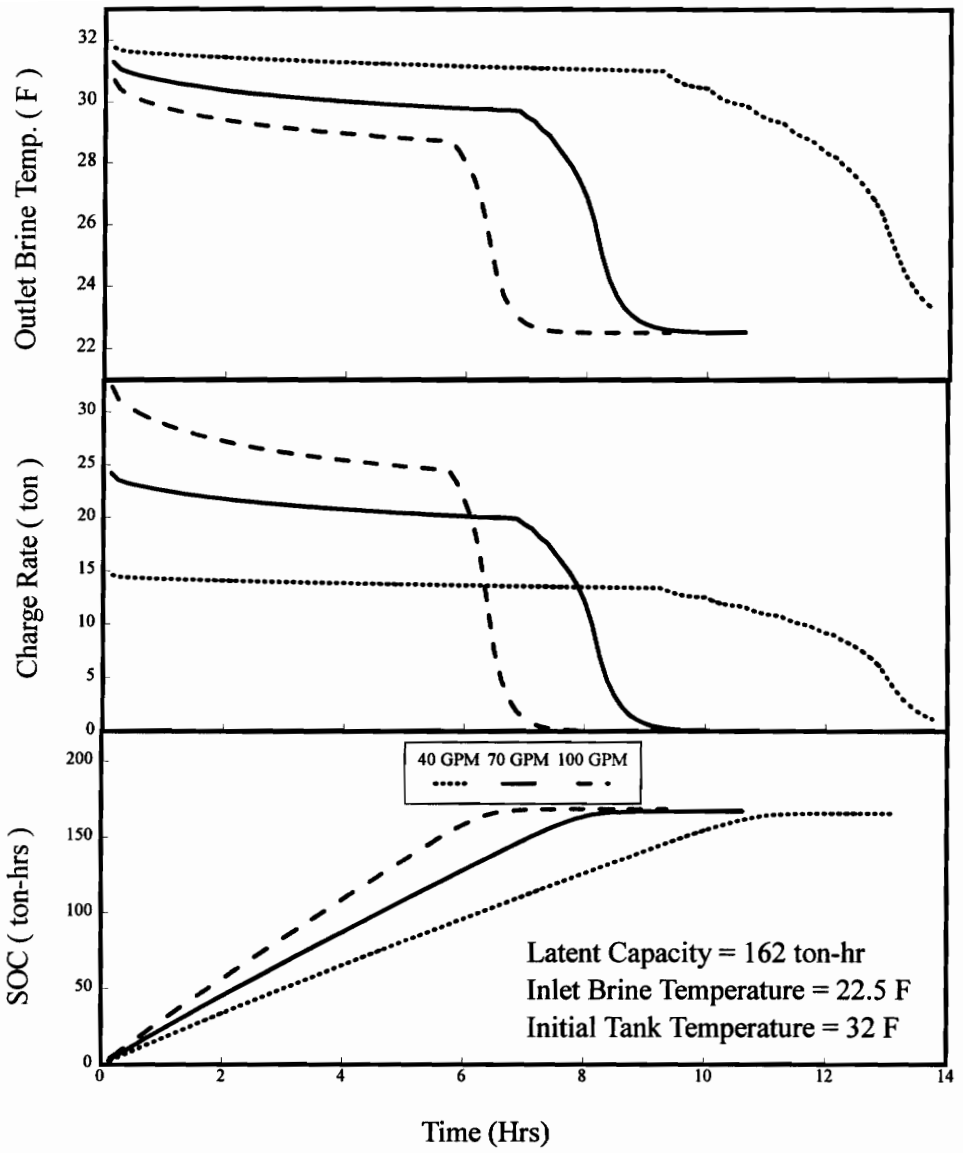

Fig. 5.3: Effects of mass flow rate on performance during a charge cycle.

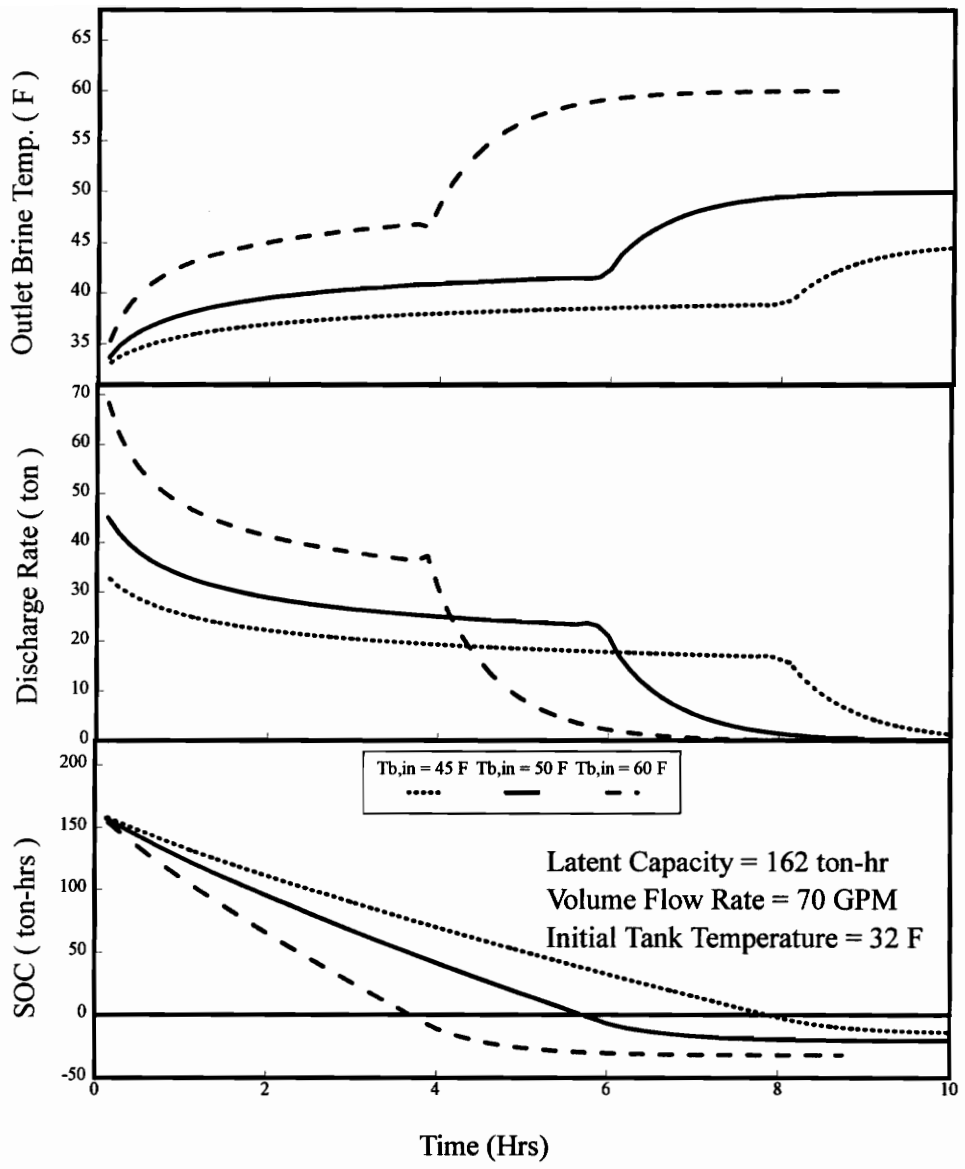

Fig. 5.4: Effects of brine inlet temperature on performance characteristics during a discharge cycle.

the inlet temperature and the discharge rate drops to zero. The state of charge drops below zero when the tank is totally discharged due to sensible heating of liquid up to the brine inlet temperature.

The effect of mass flow rate for a fixed inlet temperature is shown in Fig. 5.5. A larger mass flow rate produces outlet temperatures closer to the inlet temperatures and produces a larger discharge rate. The rapid rise in outlet temperature and drop in discharge rate occur with a greater fraction of latent capacity remaining as the mass flow rate is decreased.

In each of the Figures 5.1-5.5, the transition from latent energy mode to sensible energy mode (charging or discharging) is rather sharp. This behavior is related to two approximations in the model. When a layer collapses, the latent energy that it contains is deposited directly into (or out of) the brine. This approximation is made to ensure overall conservation of energy in the model so that long-term simulations are accurate--the net energy transfer from the brine agrees with the state of charge over many cycles. The other approximation is that the phase fronts remain axisymmetric. Thus near full charge or discharge the remaining mass for each tube is distributed in a thin ring which provides maximum surface area and minimum thermal resistance between the phase front and the tube. While this is a very good approximation for most of the charge or discharge cycle, many physical systems will exhibit some asymmetric phase fronts (such as "bridging" between tubes) near full charge that reduces the area and increases the thermal resistance. The thermal resistance and area can be corrected by incorporating a function of the state of

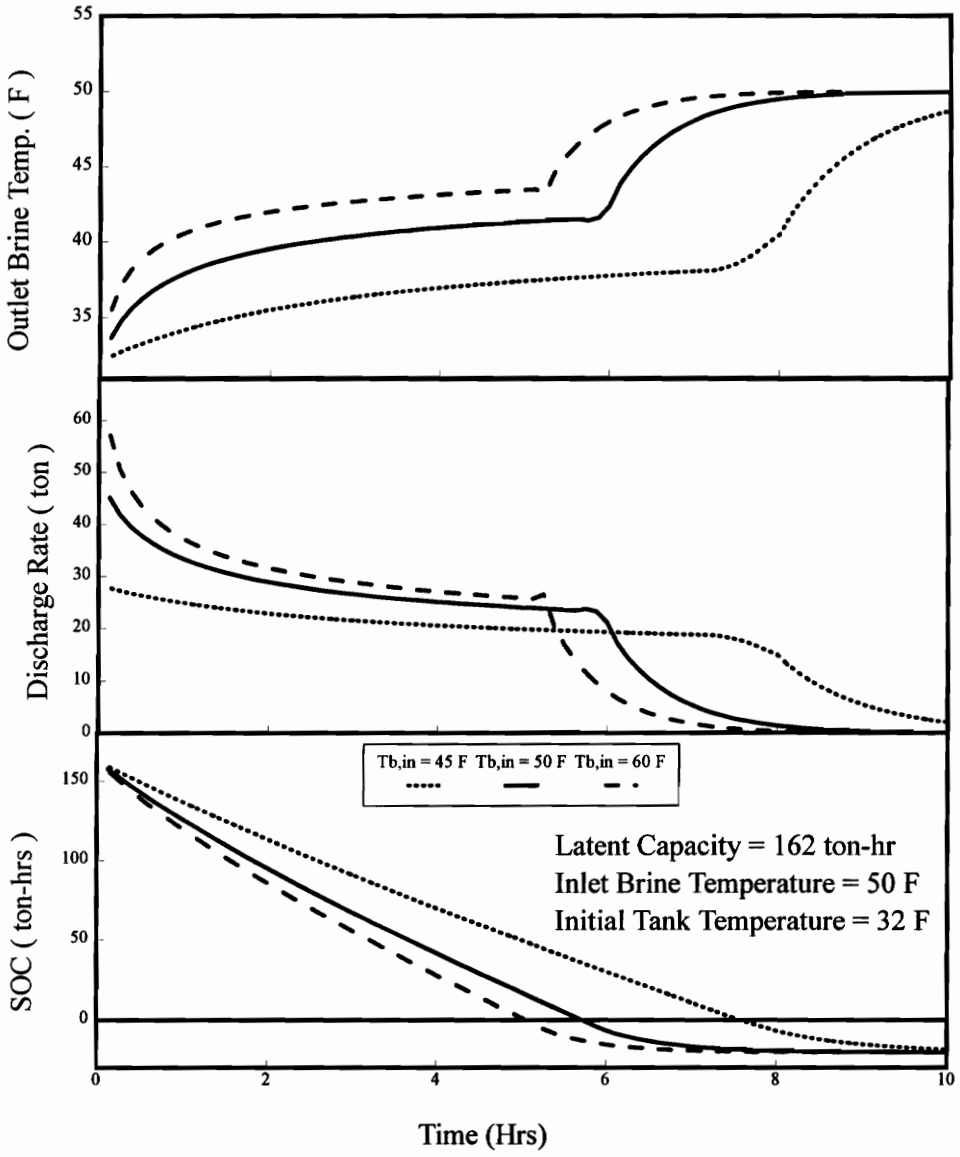

Fig. 5.5: Effects of mass flow rate on performance characteristics during a discharge cycle.

charge, as was done by Jekel (1991). This function must be specific to each possible set of tube geometries for different systems. The present axisymmetric approximation is independent of tube configuration and represents a fair approximation for all systems.

It should be noted that all the cases in the parameter studies shown in Figs. 5.1-5.5 use both constant inlet temperatures and flow rates. In practice, ice thermal storage systems rarely operate in this manner.

5.3 VALIDATION WITH CALMAC DATA FROM ORNL

In order to validate performance predictions, results generated from IceTES were compared with experimental data from an ORNL study of Calmac ice thermal storage tanks (Stovall, 1991a). The ORNL tests were performed on a Calmac model 1190, which has 162 ton-hrs of latent storage capacity. Figures 5.6 and 5.7 display comparisons for two different charging tests while Figs. 5.8, 5.9 and 5.10 compare results for three different discharge tests. All the experimental results shown in these figures were taken directly from the raw data supplied by ORNL.

The top portion of Fig. 5.6 shows the brine inlet and exit temperature data versus time for a case with a nominal charge rate of 8 tons and brine flow rate of 59 gal/min. The time history of the inlet temperature and mass flow rate recorded during the ORNL tests were input into the IceTES algorithm and the brine exit temperature was calculated and plotted in the top portion of Fig. 5.6. As shown in Fig. 5.6, the calculated and measured outlet temperatures are generally in excellent agreement. Differences occur just prior to the

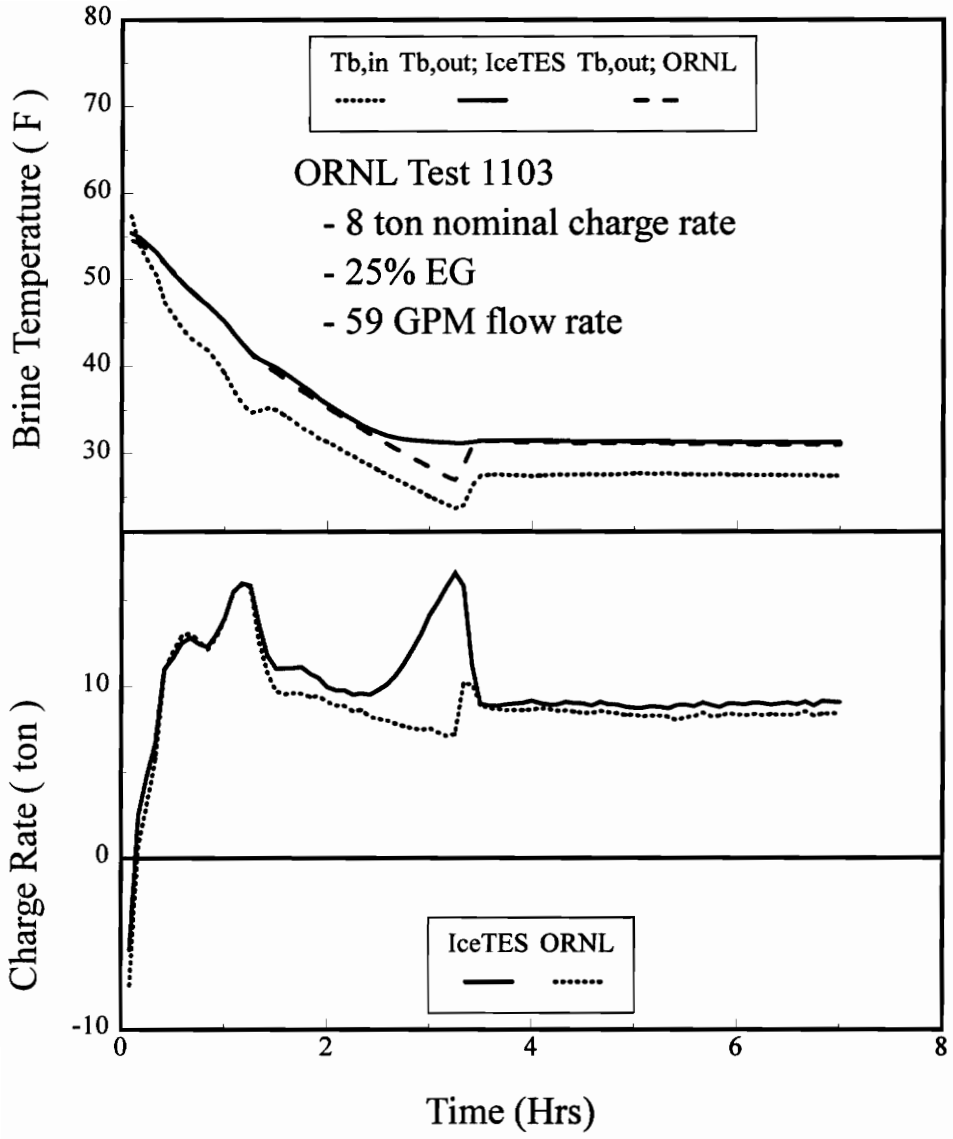

Fig. 5.6: Validation of IceTES predictions with ORNL charge data for a Calmac model 1190 with an 8 ton nominal charge rate.

Initiation of freezing, where subcooling of the liquid below 32°F was likely caused by a metastable equilibrium. This physical phenomenon is not built into the model used to create IceTES and thus cannot be predicted. The reported accuracy of the temperature data was ±0.5°F. The lower portion of Fig. 5.6 displays a comparison between the experimental and predicted charge rates. These values were calculated from eqn. (5.1) using the inlet brine temperature and mass flow rate measured during the ORNL tests together with the measured or predicted outlet brine temperatures shown in the top of the figure. Again there is excellent agreement between measured data and predictions from IceTES, except during the metastable state. Due to the low charge rate, this test did not approach full charge for the tank.

Figure 5.7 shows results from a case with a nominal charge rate of 30 tons and a flow rate of 60 gal/min. Again the experimental and predicted brine exit temperatures and charge rates are in fairly close agreement. At full charge approximately 9% of the liquid remains unfrozen in a layer at the top of the tank in the Calmac system while the IceTES algorithm distributes all the liquid evenly among the tubes. To account for this in the IceTES model, the computed results in Fig. 5.7 were obtained by using 91% of the actual mass of water in the tank. The slight up turn in charge rate before the drop off at the end of the charge cycle is caused by the model not reaching full charge at precisely the same time as the experimental system. The axisymmetric approximation discussed above also has some effect at this point. Note that in figures 5.1-5.3, the IceTES outlet brine temperature and charge rate do decrease as full charge is approached. Eight additional charge data sets

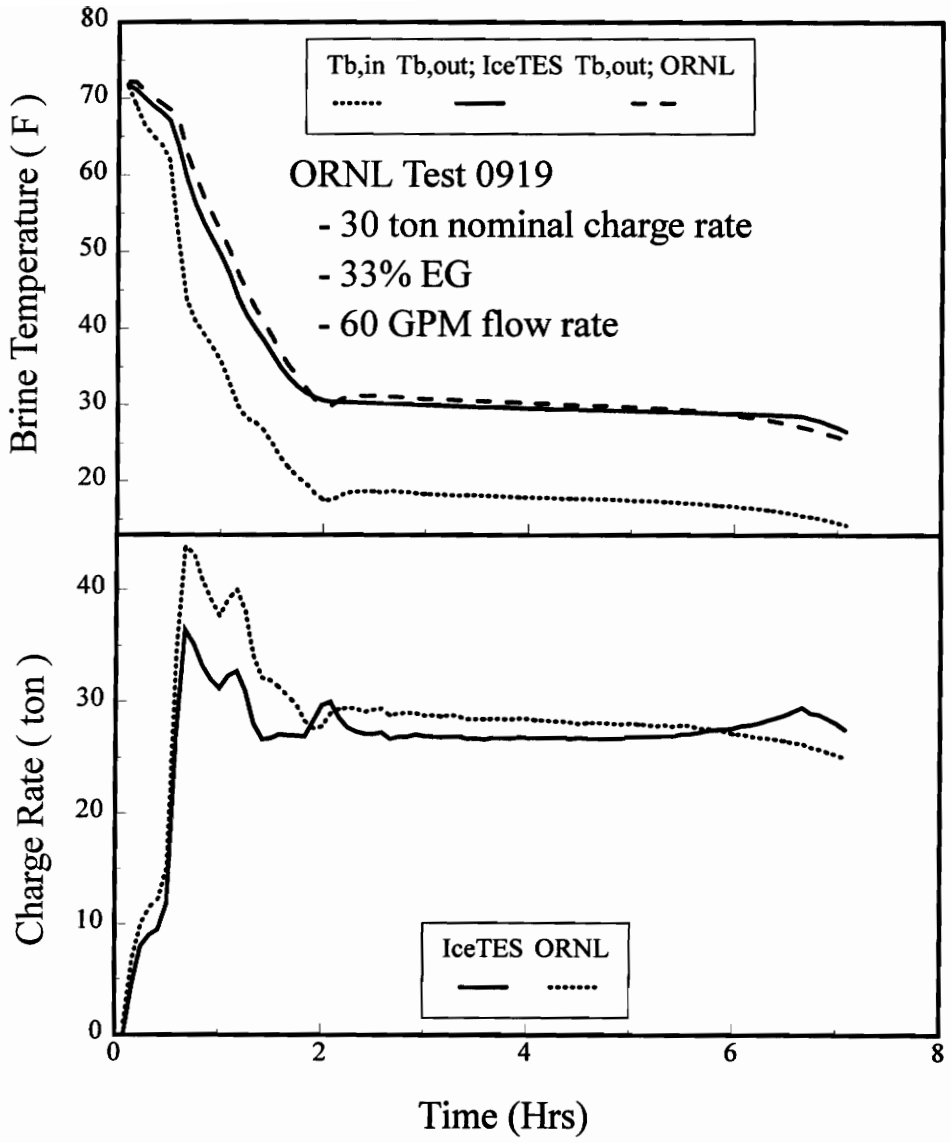

Fig. 5.7: Validation of IceTES predictions with ORNL charge data for a Calmac model 1190 with a 30 ton nominal charge rate using 91% of mass.

from ORNL were also run and compared to IceTES. These all gave as good or better agreement as Figures 5.6 and 5.7 but are not shown here.

Comparisons with discharging tests are shown in Figs. 5.8, 5.9 and 5.10. The agreement between experimentally measured and predicted brine exit temperatures and discharge rates is very good. The predicted values follow the measured data throughout the test, including the rapid rise in temperature at the end of some tests when the tanks become fully discharged and have no more ice to supply latent capacity. It is interesting to note that the discharge predictions using the IceTES algorithm are sensitive to the initial state of charge and distribution of ice in the tank, particularly near the end of discharge where small differences in the amount of remaining ice are important.

Four additional cases from the ORNL study were also validated and the agreement between the measured data and the predictions from IceTES in most cases was similar to the representative cases shown in Figs. 5.8-5.10.

5.4 VALIDATION WITH BAC DATA FROM ORNL

Performance predictions using IceTES were also compared to ORNL data for a BAC TSU275 (Stovall, 1991b), which is designed to freeze approximately 60% of the water producing 275 ton-h of stored latent energy. Calculations were made using a constant flow rate of 133 GPM and the inlet temperature profile read from the ORNL report by Stovall (1991b). The data was taken directly from the report because the raw data was not made available. As a result, the precise time history of the inlet temperature and mass flow

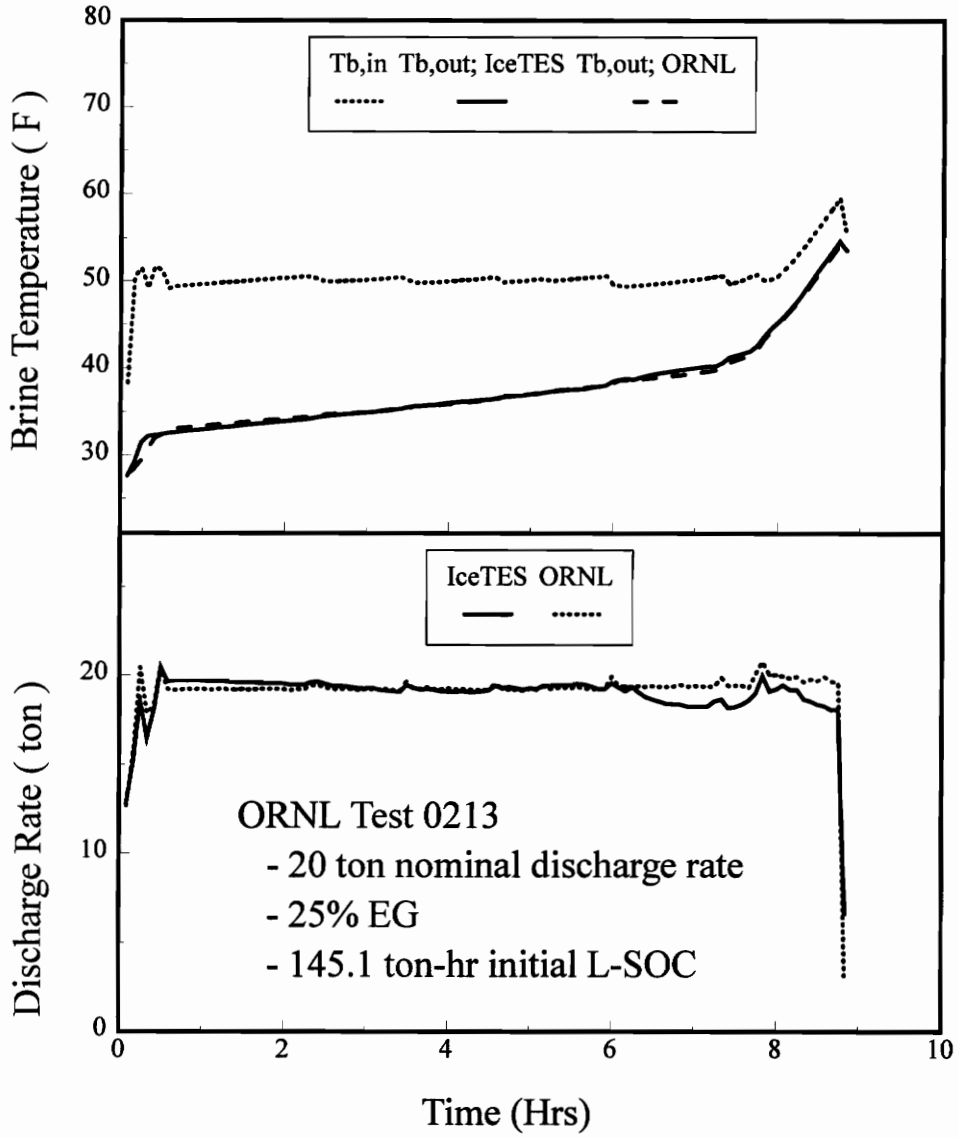

Fig. 5.8: Validation of IceTES predictions with ORNL discharge data for a Calmac 1190 with a 20 ton nominal discharge rate.

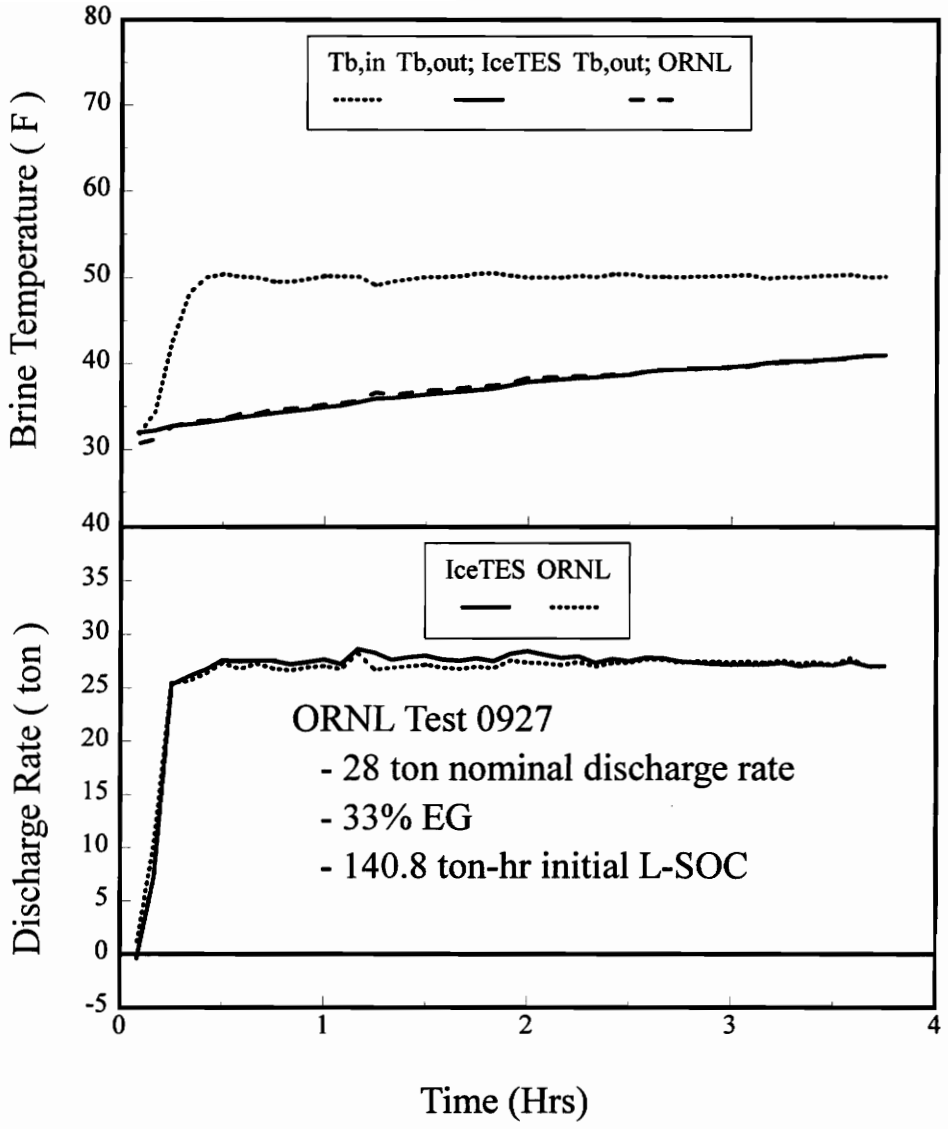

Fig. 5.9: Validation of IceTES predictions with ORNL discharge data for a Calmac 1190 with a 28 ton nominal discharge rate.

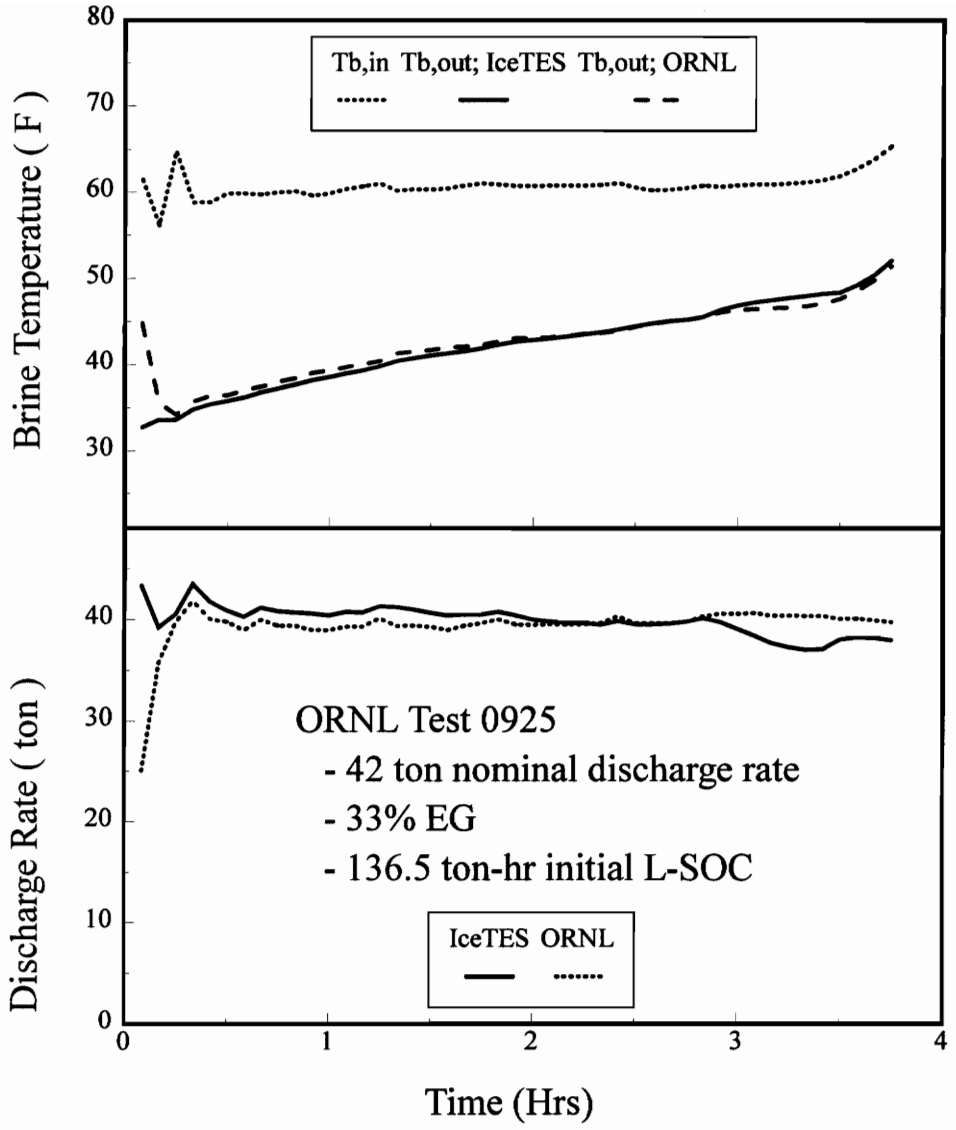

Fig. 5.10: Validation of IceTES predictions with ORNL discharge data for a Calmac 1190 with a 42 ton nominal discharge rate.

rate is approximate. In spite of this difficulty, the calculated and measured outlet brine temperatures were in very good agreement, as displayed in Fig. 5.11. The calculated brine exit temperatures are about 0.5°F lower than the measured values at the beginning of the charge cycle and gradually approach the measured values towards the end of the cycle.

No additional comparisons are reported due to the lack of the raw data. In addition, no comparisons are presented for a discharge case since the BAC units used in the ORNL tests were discharged from outside the pipes. The ice-on-pipe brine model is not valid for this situation.

5.5 SYSTEM SIMULATION

A driver program was created in order to dynamically couple the ice thermal storage component with a time varying load, chiller and control strategy. A schematic of the basic components are shown in Fig. 5.12. The driver program sets up the properties, parameters and time stepping and then calls the load, chiller and IceTES components. The chiller performance depends on the required load and the leaving brine temperature. A simple control logic is selected for this simulation for a series chiller/storage system with chiller priority (i.e. the chiller meets all the load it can with the remainder met from ice storage).

A typical design day discharge/charge cycle is used to illustrate the system simulation. The load profile was provided by the RP-699 project committee. The total load over 12 hours is 26.1 GJ (2061.5 ton-h). The peak load of 2.73 GJ/h (216 tons) occurs during the hour ending at 4 pm.

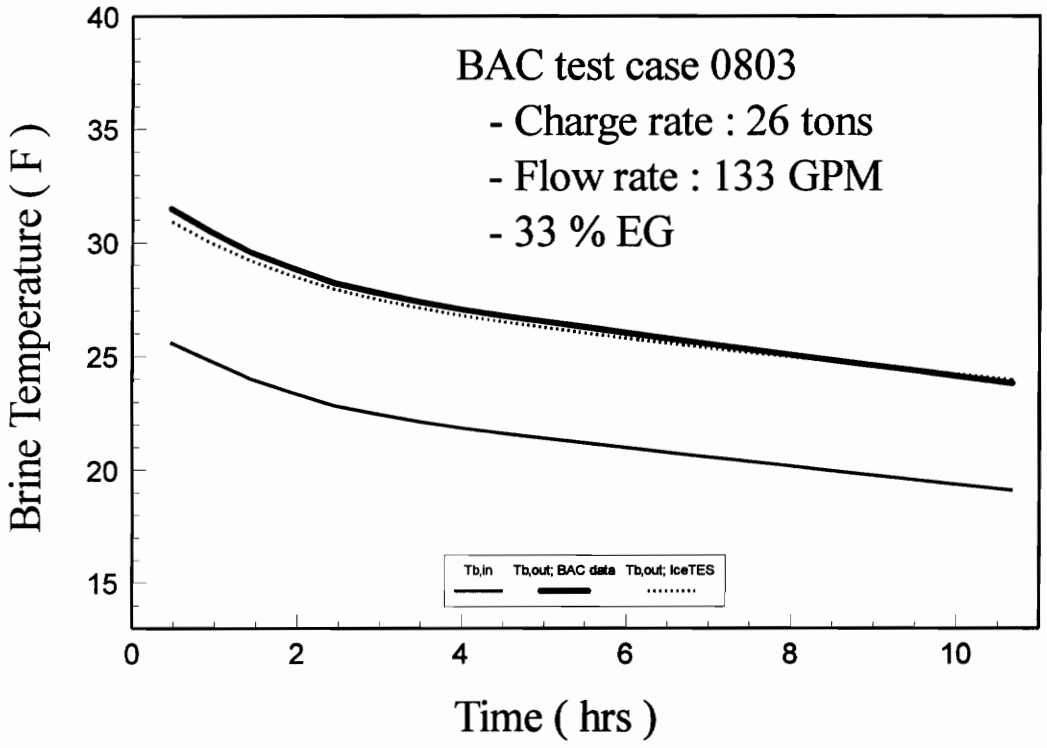

Fig. 5.11: Validation of IceTES predictions with ORNL charge data for a BAC TSU 275 with a 26 ton nominal charge rate.

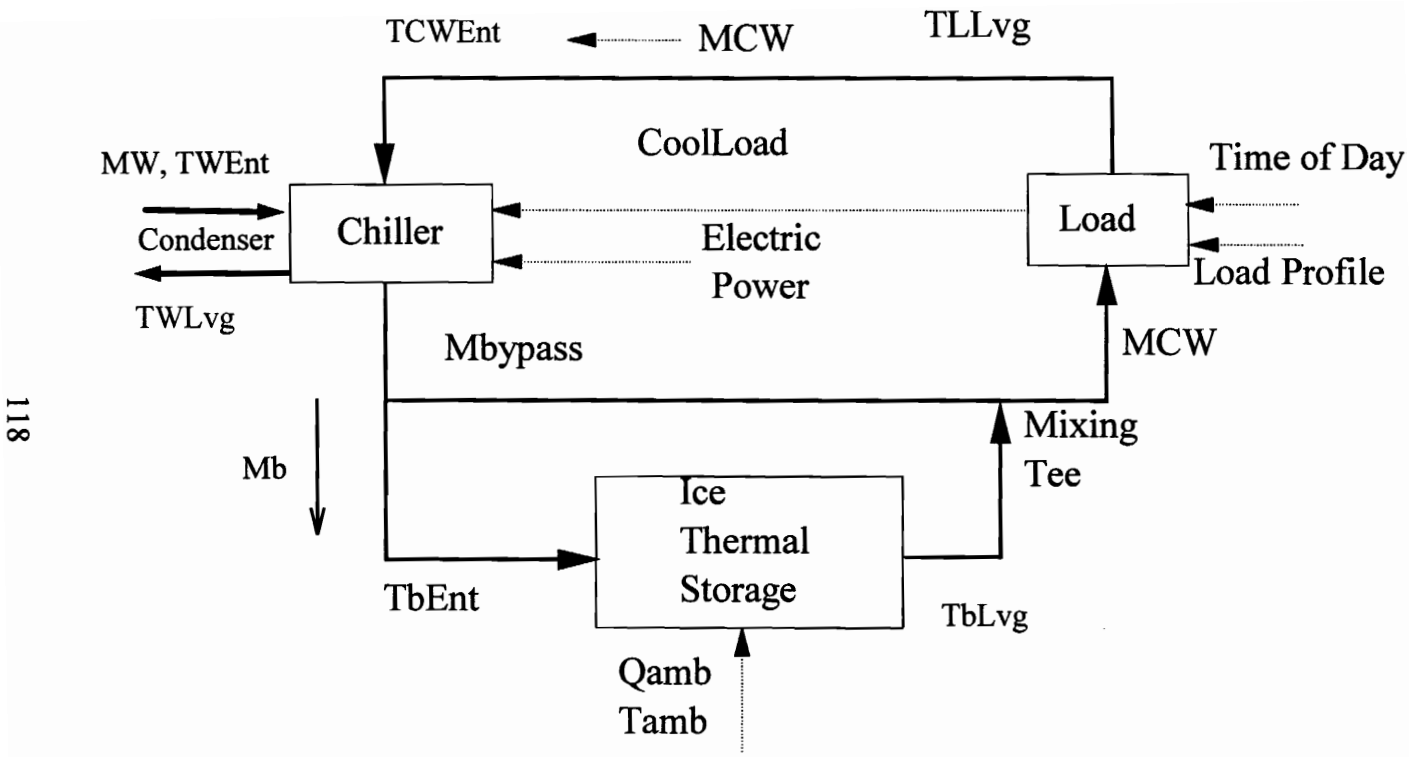

Fig. 5.12: System diagram

To meet this load profile using a partial storage design (to minimize chiller and storage size and cost), a nominal chiller size of 1.37 GJ/h (108 tons) is required. The chiller model used has approximately 60% of its nominal capacity under ice-making conditions. Of the total load over 12 hours 16.4 GJ (1296 ton-h) is provided by the chiller, leaving 9.7 GJ (765.5 ton-h) to be met from ice storage. The ice storage is recharged over the remaining 12 hours at an average rate of 0.81 GJ/h (63.8 tons), or 60% of the chiller nominal capacity.

To provide the required storage capacity, five Calmac model 1190 tanks are selected. Since each tank has 2.05 GJ (162 ton-h) of latent energy storage capacity, the tanks provide about a 5% capacity margin. The system mass flow rates are set to provide 6°C (10.8°F) temperature rise across the load heat exchanger at peak load, and 3°C (5.4°F) nominal temperature difference during charging.

The results of the system simulation for a charge/discharge cycle over a day are shown in Fig. 5.13. A one half hour time step is used. The system starts in a charge mode from an initially discharged state after the last load at 6:00pm. The IceTES brine outlet temperature gradually drops to -2°C (28.4°F) after 12 hours of charging.

During discharge mode, the brine mass flow rate through the IceTES component is iterated on at each time step until the mixing tee exit temperature is sufficient to meet the load. At the peak load, the IceTES exit temperature rises to 3.5°C (38.3°F). The present system simulation results demonstrate the application of the IceTES component model coupled to a dynamic load and chiller.

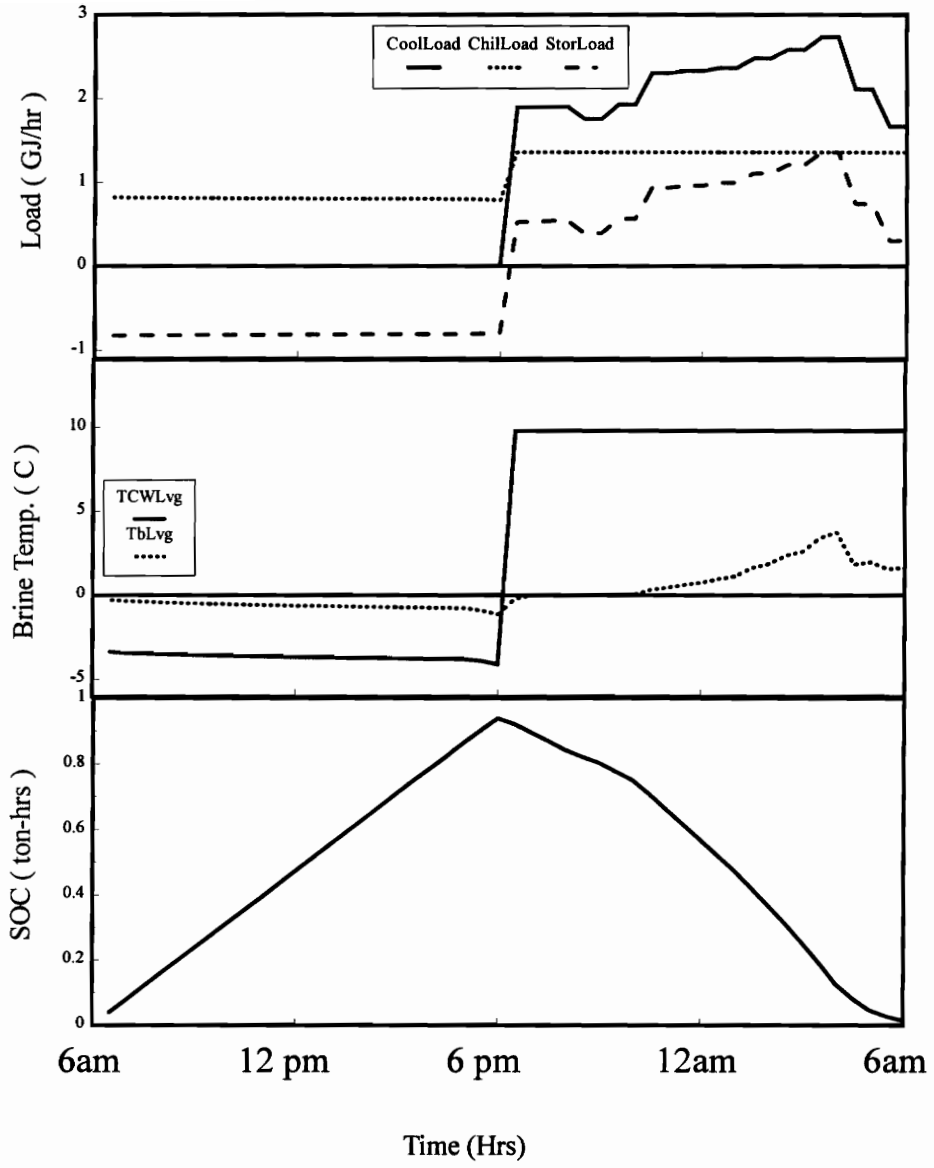

Fig. 5.13: a. Load profiles versus time of day.

b. Chiller and ice thermal storage brine exit temperatures versus time of day.

c. Latent state of charge versus time of day.

5.6 VALIDATION OF THE BEM AGAINST THE TNM AND THE NSH MODELS

To validate this algorithm, several cases with different Biot numbers, Stefan numbers, initial temperatures and Peclet numbers are tested against the thermal network method (TNM) and the negligible sensible heat (NSH) approximation method by comparing the exit temperature and the latent state of charge (mass percentage of ice). The results are shown in Fig. 5.14 to Fig. 5.18. The parameters and the property ratios are listed in Table 5.1. In these figures, the upper portion shows the latent state of charge (L-SOC) which represents the accumulated energy transferred while the lower portion of the figures shows the outlet temperature, $T_{b,out}$, which reflects the heat transfer rate at current time.

Figure 5.14 shows the results of case 1 where the nondimensional parameters are selected as, $Bi = 1$, $Ste = 1.0$, $Pe = 10^5$, $\theta_{init} = \theta_{fr} = 0.0+$. It shows that the results from the BEM and TNM have excellent agreements in both $T_{b,out}$ and L-SOC for this case. Since the system starts at liquid, $T_{init} = T_{fr}$, and the Biot number is not very high, the sensible energy does not play a very important role until the PCM at some or all of the axial segments gets fully charged or discharged. This is shown as the agreement of the NSH with the other two methods at the beginning for the L-SOC and the agreement of $T_{b,out}$ for most of the time in each freezing or melting period until the PCM around part or the whole tube becomes one single phase. Note that at each freezing period, there is a

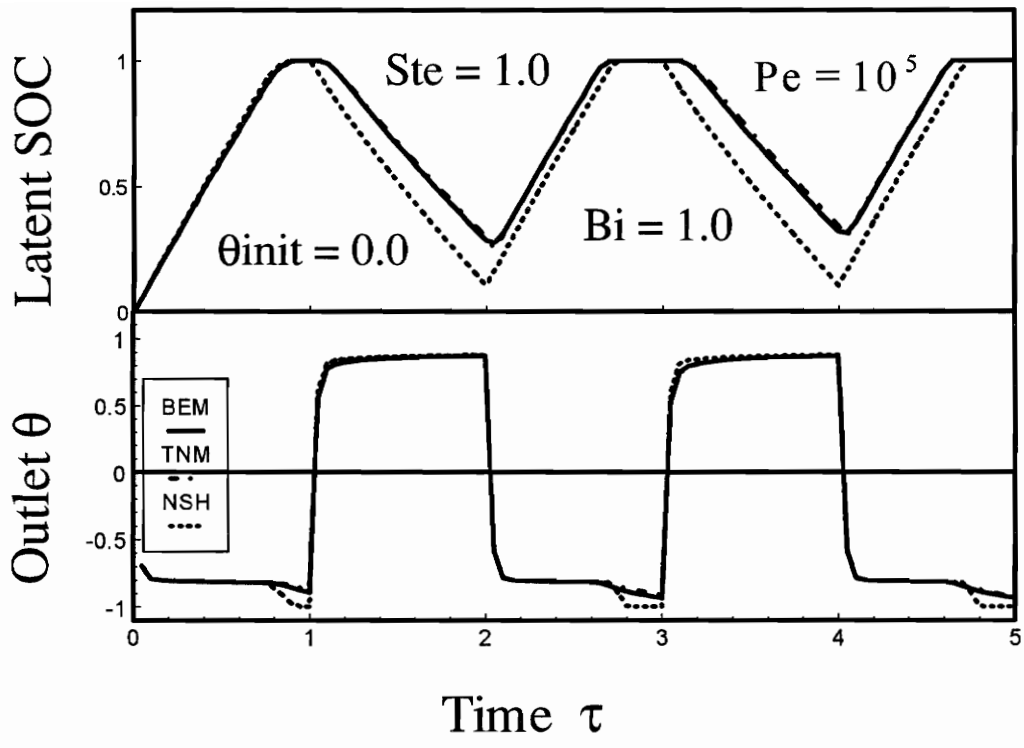

Fig. 5.14: Comparison of BEM with TNM and NSH, case 1. High Stefan number, initially saturated

sudden drop of the fluid outlet temperature in the NSH method. After the PCM around the tube becomes one single phase, the energy transferred into the PCM is stored as the sensible energy form. Thus, $T_{b,out}$ drops abruptly and the discrepancy shows up. In the melting period, due to the low conductivity in the liquid PCM, and thus less energy transferred, T_b is nearly uniform through out the tube. There is no sudden rise of $T_{b,out}$ when the PCM around part of the tube becomes a single phase liquid.

Figure 5.15 shows the results of case 2, where $Bi = 1$, $Ste = 1.0$, $Pe = 10^5$, $\theta_{init} = \theta_{fr} = 1.0$. Since the NSH does not consider the sensible heat at all, the L-SOC is far off from those of the BEM and TNM as expected for $Ste = 1.0$. The outlet temperature of fluid, $T_{b,out}$, is also off from those of the other two methods. The results from the BEM and the TNM still have very good agreement. Because the sensible energy is not considered in the NSH method, the PCM gets to a fully charged condition at each freezing period while those from the other methods do not. Similar to case 1, a sudden drop of $T_{b,out}$ still happens at the end of each freezing period. Note that there is no sudden rise in $T_{b,out}$ even after all the PCM becomes liquid because $T_{b,out}$ is always close to the upper limit $T_{b,in}$ in the melting period for these parameters. This is not true for small Peclet number cases which will be discussed later.

Figure 5.16 shows case 3 which is the same as case 2 in Fig. 5.15 except that the Stefan number is one tenth of that in case 2, $Ste = 0.1$, and the time for each period is increased by 10. The discrepancy of L-SOC and $T_{b,out}$ is much smaller comparing with

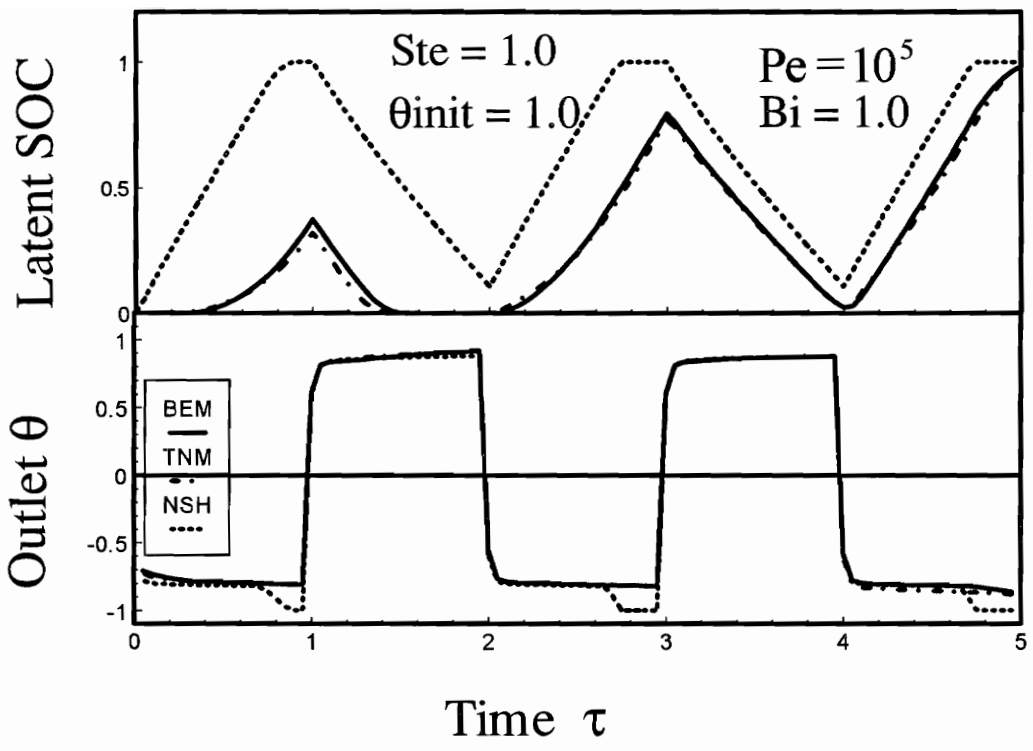

Fig. 5.15: Comparison of BEM with TNM and NSH, case 2. High Stefan number, high initially temperature

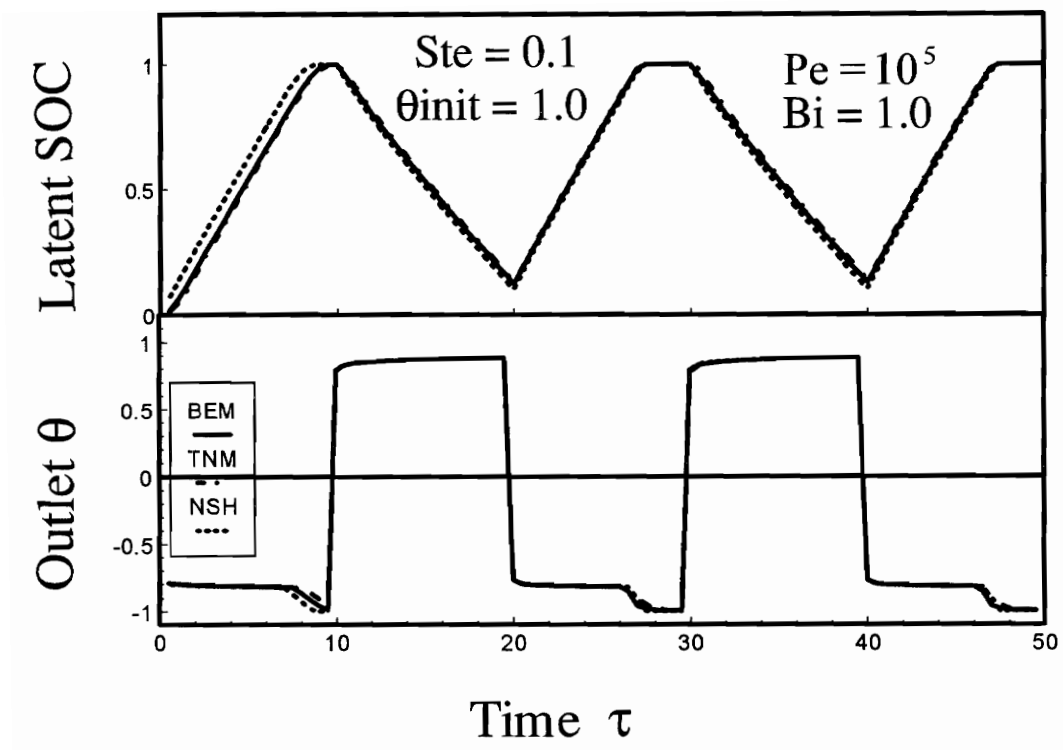

Fig. 5.16: Comparison of BEM with TNM and NSH, case 3, with low Stefan number, high initial temperature

case 2. All the other behaviors are similar to those in case 1 and case 2. Note that $T_{b,out}$ in all three methods has the dips in the freezing periods because of the small sensible energy. The offset of the L-SOC due to θ_{init} in the NSH method gets smaller after the first freezing period because less energy is stored, comparing with the initial condition.

Figure 5.17 shows the case 4 with a low Peclet number, $Pe = 10^4$, and the other parameters are $Bi = 1$, $Ste = 1.0$, $\theta_{init} = \theta_{fr} = 1.0$. Note that, the L-SOC and $T_{b,out}$ are all far off from the beginning for the NSH method. Because of the high Stefan number, high initial temperature and low Peclet number, the sensible energy plays a leading role in this case. With the same inlet temperature as the other cases, the system makes only a little ice in several segments at the entrance before the fluid is heated up above T_{fr}. The outlet temperature never gets below T_{fr} in the first freezing period. In the melting period, the PCM cools down the fluid and $T_{b,out}$ has no sudden rise in the BEM and the TNM even the PCM becomes all liquid. The sudden rise of $T_{b,out}$ occurs to the NSH method since the sensible energy is neglected. The results from the BEM and TNM still have very good agreement for all the freezing and melting periods. While this case is not representative of most ice thermal storage system operational conditions, it does illustrate conditions that may be encountered during transient operation (such as low flow rate).

Figure 5.18 shows the case 5 which has a low Biot number of $Bi = 0.1$. The other parameters are, $Ste = 1.0$, $Pe = 10^5$, $\theta_{init} = \theta_{fr} = 1.0$. The L-SOC has a similar performance to that in case 3 except that the discrepancy between the NSH method and

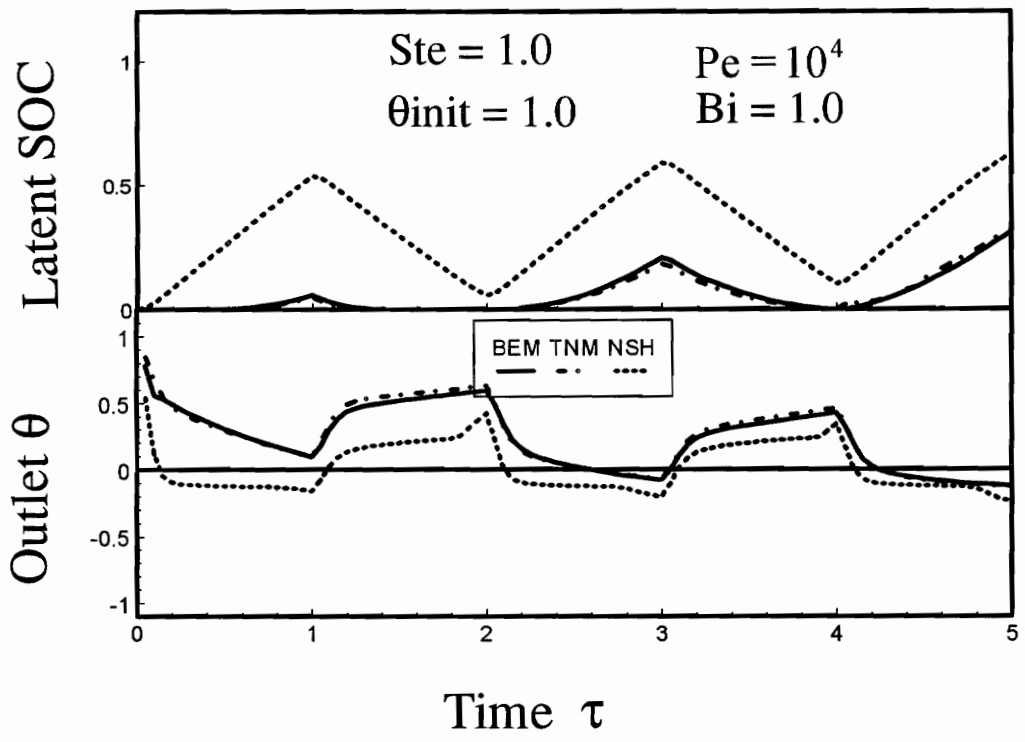

Fig. 5.17: Comparison of BEM with TNM and NSH, Case 4. High Stefan number, high initially temperature, low Peclet number

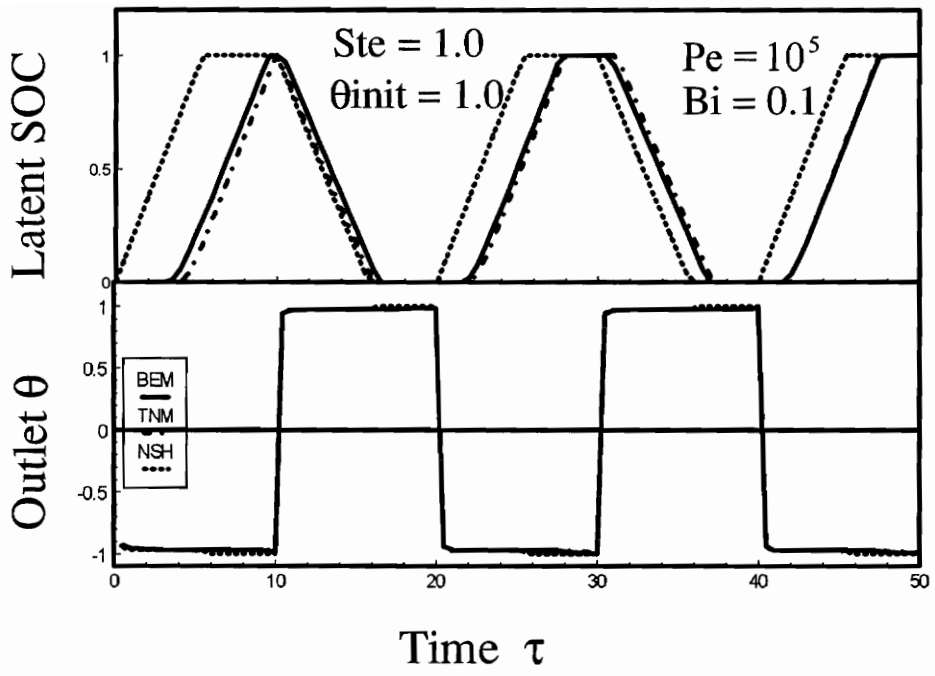

Fig. 5.18: Comparison of BEM with TNM and NSH, case 5. High Stefan number, high initially temperature, low Biot number

the other two methods is much larger. Because of the small Biot number, or less energy transferred to the PCM, the bulk temperature of fluid is almost uniform throughout the tube for this Peclet number.

CHAPTER 6 CONCLUSION

Based on the analytical results and the general trends observed, a multiple front problem arises when the system experiences partial charge and discharge while a fully charge/discharge system has at most one single moving front. If the heating and cooling periods are increased, a typical multiple front problem case could become a single front or fully charge/discharge problem. On the other hand, a fully charge/discharge system can become a partial charge/discharge system by reducing the length of the freezing and the melting periods.

By comparing the results from the TNM with experimental data and the results from the BEM with those of the TNM, we can see that both the TNM and BEM methods can track multiple layers of liquid/solid. The models can provide accurate time history of the outlet temperature and the state of charge for time varying input while and the BEM works for the parallel flow arrangements and the TNM for both the parallel and counter flow arrangements.

The boundary element method is well suited to multiple moving front problems since discretized information is only required on boundaries and phase fronts. No spatial discretization is required. The grid transformation method that works for a single moving front cannot be extended to independent multiple moving front problems. Stable and accurate results are generated using a fully implicit scheme in both the axial direction and in time.

In the thermal network method, although a number of simplifying assumptions were employed, care was taken to ensure that the solution conserved total latent and sensible energy in the system and that the important physical processes were taken into account. As a result, the results from the TNM agree with the BEM results for most of the practical cases because of the care taken to ensure that the solution conserved total latent and sensible energy in the system.

There is always a trade off between the computing time and the accuracy. For cases with very high Stefan numbers (>> 1), the BEM is suitable since the sensible energy is considered precisely. For cases with Stefan numbers in the ice thermal storage systems (< 1), TNM will be an accurate replacement of the BEM solution for different Peclet numbers, different initial temperatures and Biot numbers to save the computing time.

RECOMMENDATIONS

For future research, it would be useful to consider a two-dimensional thermal model in each axial section and thus model the effects of adjoining tubes in a more accurate manner. For cases with small Peclet number or short tubes, axial conduction effects need to be considered. In this case, two-dimensional axisymmetric with axial conduction instead of a one-dimensional radial model should be applied. For cases with neither axisymmetry nor strong convection, three-dimensional methods should be developed to accurately model the problems. In the BEM algorithm of this study, each layer is considered separately and the unknowns are solved through iteration. It would be helpful in the future study to develop an

algorithm which can track the total layer numbers and the history of each layer and put all the unknowns together in a matrix with a changing size. Thus, all the unknowns can be solved directly without iteration except the moving front positions and thus reduce the computing time.

REFERENCES

1. Abramowitz, M., and Stegun, I. A., 1972, "*Handbook of Mathmatical Functions*," Dover, New York.
2. Banerjee, P. K., and Shaw, R. P., 1982, "*Boundary Element Formulation for Melting and Solidification Problems*," in Developments in Boundary Element Methods-2, (Banerjee, Shaw, Eds.,) Applied Science Publishers, NJ.
3. Beck, J. V., and Cole, K. D., 1992, "*Heat Conduction Using Green's Functions*", Hemisphere Publishing Corporation, Bristol, Pennsylvania.
4. Choi, C. Y., and Hsieh, C. K., 1992, "*Solution of Stefan Problems Imposed with Cyclic Temperature and Flux Boundary Conditions*," International Journal of Heat Mass Transfer, Vol.35, No. 5, pp.1181-1195.
5. Jekel, T. 1991. Modeling of Ice-Storage Systems. Masters Thesis, University of Wisconsin-Madison.
6. Kim, C. J., and Kaviany, M., 1990, "*A Numerical Method for Phase-change Problems*," 1990, Int. J. of Heat Mass Transfer, Vol.33, No. 12, pp. 2721-2734.
7. Nelson, D.J., and Vick, B., 1994, "*Freezing and Melting with Multiple Phase Fronts Using the Boundary Element Method, Part I: Analysis*" Proceeding of the 10th International Heat Transfer Conference, Brighton, England, Aug. 14-18, 1994.
8. Nelson, D.J., and Vick, B., and Yu, X., 1994, "*Model of an Ice-on-Pipe Brine Thermal Storage Component*," submitted to ASHRAE transactions.

9. Nelson, D. J., Vick, B., and Yu, X. 1994b. *IceTES User's Guide*. to be published by ASHRAE.

10. O'Neill, K., 1983, "*Boundary Integral Equation Solutuin of Moving Boundary Phase Change Problems*," Int. J. for Numerical Methods in Eingineering, Vol.19, pp. 1825-1850.

11. Pasquetti, R., and Caruso, A., 1990, "*Boundary Element Approach for Transient and Nonlinear Thermal Diffusion*," Numerical Heat Transfer, part B, Vol.17, pp.83-99.

12. Patankar, S. V. 1980. *Numerical Heat Transfer and Fluid Flow*, Hemisphere Publishing Corporation.

13. Sadegh, A.M., Jiji, L. M., and Weinbaum, S., 1987, "*Boundary Integral Equation Technique with Application to Freezing Around a Buried Pipe*," Int. J. of Heat Transfer, Vol.30, No.2, pp.223-232.

14. Shah, R. K., and Joshi, S. D. 1987. Convective Heat Transfer in Curved Ducts, Chapter 5, and Flow Bends and Fittings, Chapter 10, in *Handbook of Single-Phase Convective Heat Transfer*. Kakac, Shah, and Aung, eds., John Wiley and Sons, New York.

15. Sieder, E. N., and Tate, C. E. 1936. Heat Transfer and Pressure Drop of Liquids in Tubes, *Ind. Eng. Chem.* 28: 1429-1439.

16. Silver, S. C., Jones, J. W., Peterson, J. L., and Hunn, B. D. 1989. CBS/ICE: A Computer Program for Simulation of Ice Storage Systems, *ASHRAE Transactions* 95(1): 1206-1213.

17. Silver, S. C., Milbitz, A., Jones, J. W., Peterson, J. L., and Hunn, B. D. 1989. Component Models for Computer Simulation of Ice Storage Systems, *ASHRAE Transactions* 95(1): 1214-1226.

18. Stovall, T. K. 1991a. *Calmac Ice Storage Test Report.* ORNL/TM-11582, Martin Marietta Energy Systems, Inc., Oak Ridge National Laboratory.

19. Stovall, T. K., 1991b. *Baltimore Aircoil Company (BAC) Ice Storage Test Report.* ORNL/TM-11342, Martin Marietta Energy Systems, Inc., Oak Ridge National Laboratory.

20. Vick, B., and Nelson, D.J., 1993, "*The Boundary Element Method Applied to Freezing and Melting Problems*," Numerical Heat Transfer, Part B: Fundamentals, Vol. 24, pp263-277.

21. Vick, B., and Nelson, D.J., 1994, "*Freezing and Melting with Multiple Phase Fronts Using the Boundary Element Method, Part II: Results*" Proceeding of the 10th International Heat Transfer Conference, Brighton, England, Aug. 14-18, 1994.

22. Vick, B., Nelson, D. J., and Yu, X., 1994, " *Validation of the Algorithm for Ice-on-Pipe Brine Thermal Storage Systems*," submitted to ASHRAE Transactions.

23. Wrobel, L. C., and Brebbia, C. A., 1981, "*Boundary Elements in Thermal Problems*," in Numerical Methods in Heat Transfer, John Wiley, New York, NY, pp.91-113.

24. Wrobel, L. C., and Brebbia, C. A., 1981, "*A Formulation of the Boundary Element Method for Axisymmetric Transient Heat Conduction*," Int. J. of Heat Mass Transfer, Vol.24, No. 5, pp. 843-850.

25. X. Yu, D. J. Nelson and B. Vick, 1994, *Phase Change With Multiple Fronts In Cylindrical Systems Using the Boundary Element Method,* accepted by Journal of Boundary Element Method in Heat Transfer Problems.

APPENDIX A: SENSIBLE ENERGY

Consider a circular annulus of length Δx, inside radius r_i, outside radius r_o, and temperatures T_i and T_o on the inside and outside radius, respectively. If steady-state conditions exist, the temperature distribution is,

$$T(r) = T_o + (T_i - T_o) \frac{\ell n(r / r_o)}{\ell n(r_i / r_o)} \qquad \text{(A. 1)}$$

The sensible energy content is,

$$E_{sen} = \rho C_p \Delta x \int_{r_i}^{r_o} T(r) 2\pi r dr \qquad \text{(A. 2)}$$

If a quasi-steady state assumption is used in which time changes are slow, then the temperature profile can be approximated by eqn. (A.1) at any instant of time and the sensible energy content becomes,

$$E_{sen} = C_o T_o + C_i T_i \qquad \text{(A. 3)}$$

where

$$C_o = \rho C_p \pi \Delta x \left[r_o^2 - (r_o^2 - r_i^2) / 2 / \ell n(r_o / r_i) \right] \qquad \text{(A. 4)}$$

$$C_i = \rho C_p \pi \Delta x \left[-r_i^2 + (r_o^2 - r_i^2) / 2 / \ell n(r_o / r_i) \right] \qquad \text{(A. 5)}$$

The coefficients C_o and C_i represent thermal capacity associated with T_o and T_i, respectively. Note that if $T_o = T_i = T$, then the sensible energy given by eqn. (A.3) reduces to

$$E_{sen} = \rho C_p \pi \Delta x (r_o^2 - r_i^2) T \qquad \text{(A.6)}$$

APPENDIX B: HEAT TRANSFER COEFFICIENT

The forced convention heat transfer coefficient is calculated using fully developed flow correlations for laminar and turbulent flow in a spiral tube. The following correlations are suggested Shah and Joshi (1987, Ch. 5) to calculate the Nusselt number in terms of the dimensionless parameters,

$$Re_D = \frac{4\dot{m}}{\pi D\mu} = \text{Reynolds number} \qquad \text{(A. 7)}$$

$$De = \mathrm{Re}_D\left(\frac{r_{pi}}{r_{ave}}\right)^{0.5} = \text{Dean number} \qquad \text{(A. 8)}$$

$$Pr = \frac{\nu}{\alpha} = \frac{\mu c_p}{k} = \textit{Prandtl number} \qquad \text{(A. 9)}$$

where r_{ave} is the mean radius of curvature for a spiral.

Laminar Flow: $Re_D \leq 1500$

$$Nu_D = \frac{\bar{h}D}{k} = 4.36\left[1 + 0.0276\ De^{0.75}\mathrm{Pr}^{0.197}\left(\frac{\mu}{\mu_w}\right)^{0.14}\right] \qquad \text{(A. 10)}$$

where μ is the viscosity evaluated at the mean brine temperature and μ_w is evaluated at the wall temperature. This fully developed correlation is used since secondary flow makes development lengths short.

Turbulent Flow: $Re_D \geq 4000$

$$Nu_D = 1.04\left[0.027\ \mathrm{Re}_D^{0.8}\ \mathrm{Pr}^{1/3}\left(\frac{\mu}{\mu_w}\right)^{0.14}\right] \qquad \text{(A. 11)}$$

This correlation is the Sieder and Tate (1936) equation for turbulent flow with a 4 percent enhancement due to the spiral tubes.

Transition Regime: $1500 < Re_D < 4000$

In the transition Reynolds number regime, a linear interpolation between the laminar and turbulent correlations is used.

The previous correlations were developed for spiral tubes appropriate for the geometry in Calmac systems. However, these same correlations were also recommended by Shah and Joshi (1987, Ch. 10) for tubes with 90 and 180 degree bends appropriate for the geometry in BAC ice tanks.

APPENDIX C: NUMERICAL TIME INTEGRATION OF THE GREEN'S FUNCTION AND ITS GRADIENT

For one-dimensional radial problems, the Green's function and its gradient are given by expression eqn. (2.16) and eqn. (2.17). There are no general analytical expressions for the time integrals GI and HI of $G(r,t|r_0,t_0)$ and $\partial G / \partial r_0$ defined by eqn. (2.26). For the cases with $rr_0 = 0$, GI and HI can be calculated analytically. For $rr_0 \neq 0$, polynomial approximations with sufficient accuracy have been applied for computational purposes. To apply the approximations, the following variable changes are used,

$$Z = \frac{rr_0}{2\alpha(t - t_0)}, \qquad Z^n = \frac{rr_0}{2\alpha(t - t^n)} \tag{A. 12}$$

$$p = \frac{r^2 + r_0^2}{2rr_0} \tag{A. 13}$$

$$x = \frac{r^2 + r_0^2}{4\alpha(t - t_0)} = pZ, \quad x^n = \frac{r^2 + r_0^2}{4\alpha(t - t^n)} = pZ^n \tag{A. 14}$$

then, for $rr_0 \neq 0$, the expression (2.26) becomes,

$$\begin{aligned} (GI)^n &= \int_{t^{n-1}}^{t^n} G(r,t|r_0,t_0)dt_0 = \int_{Z^{n-1}}^{Z^n} \frac{1}{4\pi Z} e^{-pZ} I_0(Z)dZ \\ (HI)^n &= \int_{t^{n-1}}^{t^n} \frac{\partial G(r,t|r_0,t_0)}{\partial r_0} dt_0 = \int_{Z^{n-1}}^{Z^n} \frac{e^{-pZ}}{4\pi\alpha r r_0} \left[rI_1(Z) - r_0 I_0(Z)\right] dZ \end{aligned} \tag{A. 15}$$

Let $y = x / 3.75$, the polynimial approximations of the Bessel functions $I_0(x)$ and $I_1(x)$ are as follows [1],

$$\begin{aligned} I_0(x) &= \sum_{l=0}^{6} a_l y^{2l} + \varepsilon \\ &= 1 + 3.5156229y^2 + 3.0899424y^4 + 1.2067492y^6 \\ &\quad + .2659732y^8 + .0360768y^{10} + .0045813y^{12} + \varepsilon \end{aligned} \tag{A. 16}$$

$$|\varepsilon| \leq 1.6 \times 10^{-7}, \text{ for } -3.75 \leq x \leq 3.75$$

$$\begin{aligned} x^{\frac{1}{2}} e^{-x} I_0(x) &= \sum_{l=0}^{8} b_l y^{-l} + \varepsilon \\ &= .39894228 + .01328592y^{-1} + .00225319y^{-2} - .00157565y^{-3} \\ &\quad + .00916281y^{-4} - .02057706y^{-5} + .02635537y^{-6} - .01647633y^{-7} \\ &\quad + .00392377y^{-8} + \varepsilon \end{aligned} \tag{A. 17}$$

$$|\varepsilon| \leq 1.9 \times 10^{-7}, \text{ for } 3.75 \leq x \leq \infty$$

$$x^{-1}I_1(x)=\sum_{l=0}^{6}c_l y^{2l}$$

$$=\frac{1}{2}+.87890594y^2+.51498869y^4+.15084934y^6+.02658733y^8 \qquad \text{(A. 18)}$$
$$+.00301532y^{10}+.00032411y^{12}+\varepsilon$$

$$|\varepsilon|\le 8\times 10^{-9},\quad \text{for } -3.75\le x\le 3.75$$

$$x^{\frac{1}{2}}e^{-x}I_1(x)=\sum_{l=0}^{8}d_l y^{-l}$$

$$=.39894228-.03988024y^{-1}-.00362018y^{-2}+.00163801y^{-3} \qquad \text{(A. 19)}$$
$$-.01031555y^{-4}+.02282967y^{-5}-.02895312y^{-6}+.01787654y^{-7}$$
$$-.00420059y^{-8}+\varepsilon$$

$$|\varepsilon|\le 2.2\times 10^{-7},\ \text{for } 3.75\le x\le\infty$$

With these approximations, the integrations can be performed analytically for the cases of $rr_0\neq 0$.

Integrals of Green's Function: $(GI)^n$

- **Case 1:** $r=r_0=0$,

$$G(r,t|r_0,t_0)=\frac{1}{4\pi\alpha(t-t_0)} \qquad \text{(A. 20)}$$

$$(GI)^n=\frac{1}{4\alpha\pi}\ln\frac{(t-t^{n-1})}{(t-t^n)} \qquad \text{(A. 21)}$$

- **Case 2:** $r=0$ or $r_0=0$,

$$G(r,t|r_0,t_0)=\frac{xe^{-x}}{\pi(r^2+r_0^2)} \qquad \text{(A. 22)}$$

where x is defined by eqn (A. 14), $(GI)^n$ can be calculated analytically in the form,

$$(GI)^n = \frac{1}{4\alpha\pi}[\Gamma(0,x^{n-1}) - \Gamma(0,x^n)] \qquad \text{(A. 23)}$$

- **Case 3:** $r = r_0 \neq 0$,

After using Bessel function approximations (A. 16) and (A. 17), the Green's function integrals can be evaluated as,

$$(GI)^n = \begin{cases} \dfrac{1}{4\alpha\pi}\displaystyle\sum_{l=0}^{6}\frac{a_l}{3.75^{2l}}[\Gamma(2l,x^{n-1}) - \Gamma(2l,x^n)], & |x| < 3.75 \\ \dfrac{1}{2\alpha\pi}\displaystyle\sum_{l=0}^{8} 3.75^l b_l \frac{(x^{n-1})^{-(n+\frac{1}{2})} - (x^n)^{-(n+\frac{1}{2})}}{2n+1}, & x \geq 3.75 \end{cases} \qquad \text{(A. 24)}$$

- **Case4:** $r \neq r_0$, $rr_0 \neq 0$,

Approximation (A. 16) and (A. 17) are used again to produce,

$$(GI)^n = \begin{cases} \dfrac{1}{4\alpha\pi}\displaystyle\sum_{l=0}^{6}\frac{c_l}{3.75^{2l}p^{2l}}[\Gamma(2l,pZ^{n-1}) - \Gamma(2l,pZ^n)], & |Z| < 3.75 \\ \dfrac{1}{4\alpha\pi}\displaystyle\sum_{l=0}^{8} 3.75^l d_l (p-1)^{l+\frac{1}{2}}\left[\Gamma\left(-l-\frac{1}{2},(p-1)Z^{n-1}\right) - \Gamma\left((-l-\frac{1}{2},(p-1)Z^n\right)\right], \\ \qquad\qquad Z \geq 3.75 \end{cases}$$

(A. 25)

Integrals of Green's Function Gradient: $(HI)^n$

- **Case1:** $r_0 = 0$,

$$\frac{\partial G}{\partial r_0} = 0 \qquad \text{(A. 26)}$$

and,

$$(HI)^n = 0 \tag{A. 27}$$

- **Case2 :** $r = 0,\ r_0 \neq 0$,

$$\frac{\partial G}{\partial r_0} = -\frac{2x^2}{\pi r_0} e^{-x} \tag{A. 28}$$

$$(HI)^n = -\frac{e^{-x^n} - e^{-x^{n-1}}}{2\alpha\pi r_0} \tag{A. 29}$$

- **Case3:** $r = r_0 \neq 0$,

$$\frac{\partial G}{\partial r_0} = \frac{x^2}{2\pi r_0^3} e^{-x}[I_1(x) - I_0(x)] \tag{A. 30}$$

$$(HI)^n = \begin{cases} \dfrac{1}{4\alpha\pi r} \displaystyle\sum_{l=0}^{6} 3.75^{-2l} \{c_l[\Gamma(2l+2, x^{n-1}) - \Gamma(2l+2, x^n)] \\ \qquad\qquad - a_l[\Gamma(2l+1, x^{n-1}) - \Gamma(2l+1, x^n)]\}, \quad |x| < 3.75 \\ \dfrac{1}{2\alpha\pi r} \displaystyle\sum_{l=0}^{8} 3.75^l (d_l - b_l) \frac{(x^{n-1})^{-i+\frac{1}{2}} - (x^n)^{-i+\frac{1}{2}}}{2l-1}, \quad x \geq 3.75 \end{cases} \tag{A. 31}$$

- **Case4:** $r \neq r_0$ and $rr_0 \neq 0$,

$$\frac{\partial G}{\partial r_0} = \frac{Z^2}{2\pi r_0^2 r^2} e^{-pz}[rI_1(x) - r_0 I_0(x)] \tag{A. 32}$$

$$(HI)^n = \begin{cases} \dfrac{1}{4\alpha\pi r}\displaystyle\sum_{l=0}^{6} 3.75^{-2l} p^{-(2l+2)} \{c_l r[\Gamma(2l+2, pZ^{n-1}) - \Gamma(2l+2, pZ^n)] \\ \qquad - a_l r_0 p[\Gamma(2l+1, pZ^{n-1}) - \Gamma(2l+1, pZ^n)]\}\,, & |x| < 3.75 \\ \dfrac{1}{4\alpha\pi r}\displaystyle\sum_{l=0}^{8} 3.75^l (d_l r - b_l r_0)(p-1)^{l-\frac{1}{2}} \left\{\Gamma\left[(-l+\frac{1}{2}), (p-1)Z^{n-1}\right]\right. \\ \qquad \left. - \Gamma\left[(-l+\frac{1}{2}), (p-1)Z^{n}\right]\right\}\,, & x \geq 3.75 \end{cases}$$

(A. 33)

APPENDIX D: NEGLIGIBLE SENSIBLE HEAT MODEL

---- Solidification of a Cylinder From Inside

Figure A-1 shows the problem considered. The phase change mateial is contained in two concentric thin walls and is insulated at the outside surface. The conditions are,

- The PCM starts as all liquid initially at the melt temperature $T_{init} = T_{fr}$
- Inside surface exposed to convection with h_b, T_b
- Negligible heat capacity in the solid layer

The energy balance at the phase front, $r = s(t)$, gives,

$$q_s' = \frac{T_{fr} - T_b}{R_{conv} + R_{cond}} = \frac{T_{fr} - T_b}{\dfrac{\ln\left(\dfrac{s}{r_{in}}\right)}{2\pi k_s} + \dfrac{1}{2\pi h_b r_{in}}} = 2\pi s \rho h_{if} \frac{ds}{dt} \qquad \text{(A. 34)}$$

where R_{conv} and R_{cond} are convective and conductive resistences.

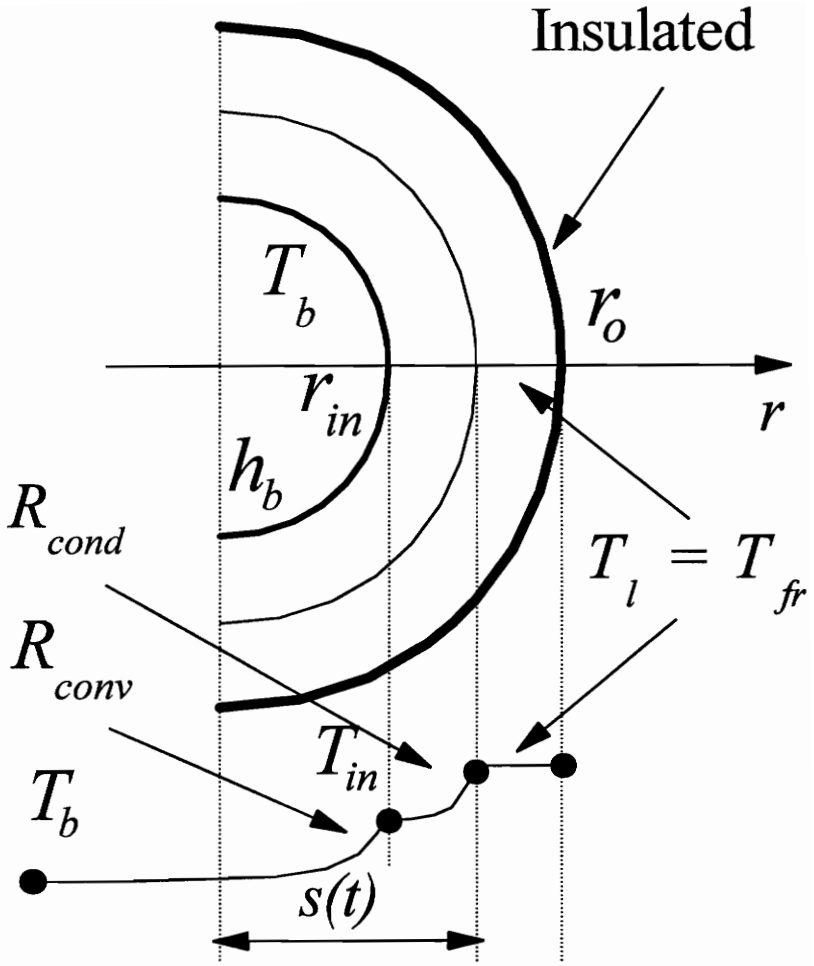

Fig. A.1: No sensible heat model

Multiplyeqn.(A.34) by $\frac{c_p}{h_{if} k_s}$ gives,

$$Ste \times \alpha dt = \left[\ln\left(\frac{s}{r_{in}}\right) + \frac{k_s}{h_b r_{in}} \right] s ds \qquad \text{(A. 35)}$$

where,

$$Ste = \frac{Cp_s (T_{fr} - T_b)}{h_{if}} \qquad \text{(A. 36)}$$

Integrate the equation at 0 to t and r_{in} to $s(t)$,

$$Ste \times \alpha t = \frac{(s^2 - r_{in}^2)}{2}\left(\frac{k_s}{h_b r_{in}} - \frac{1}{2}\right) + \frac{s^2}{2}\ln\left(\frac{s}{r_{in}}\right) \qquad \text{(A. 37)}$$

We can similarily get the expression of solifidation from outside as,

$$t^+ = \frac{r_0^{+2}}{4}\left\{\left(1 - \frac{s^+}{r_0^+}\right)^2\left[2\ln\left(1 - \frac{s^+}{r_0^+}\right) - 1\right] + 1\right\} - \frac{r_0^+}{2}\left[\left(1 - \frac{s^+}{r_0^+}\right)^2 - 1\right] \qquad \text{(A. 38)}$$

where r_0 is the outside position, t^+, r_0^+, r^+ and s^+ are defined as,

$$\begin{aligned} s^+ &= s\frac{h_b}{k_s} \\ r^+ &= r\frac{h_b}{k_s} \\ r_0^+ &= r_0\frac{h_b}{k_s} \\ t^+ &= t \times Ste \times \alpha_s\left(\frac{h_b}{k_s}\right)^2 \end{aligned} \qquad \text{(A. 39)}$$

By changing the properties of solid to liquid we can easily get the expression of ablation from both inside and outside.

Vita

Born on March 22, 1964 in Mudanjiang, Heilongjiang Province of China, the author received his primary and secondary education in nearby Ningan, Heilongjiang. He graduated from the No.2 High School of Baotou, Innermongolia of China in July 1980 and enrolled in Beijing University of Aeronautics and Astronautics (BUAA) the following September. Upon graduating with a B.S. in the Department of Aircraft Design and Applied Mechanics in July 1984, he immediately transferred to the Department of Power in BUAA as a Master's student in September. After receiving his M.S. in December 1986, he entered in a Ph.D. program in March 1987. In August 1991, he entered the Ph.D. program in Mechanical Engineering Department at VPI&SU as a research assistant. Four years later, he received his Ph.D. in Mechanical Engineering in May 1995.